UNIVERSIDADE TECNOLÓGICA FEDERAL DO PARANÁ

JOEL ROBERT KARP

THE DYNAMICS OF COMPOUND DROPS RISING IN A QUIESCENT VISCOUS FLUID

CURITIBA

2021

JOEL ROBERT KARP

THE DYNAMICS OF COMPOUND DROPS RISING IN A QUIESCENT VISCOUS FLUID

Dinâmica de gotas compostas escoando em um fluido viscoso estagnado

Tese apresentada como requisito para obtenção do título de Doutor em Engenharia Mecânica – Área de Concentração: Engenharia Térmica, do Programa de Pós-Graduação em Engenharia Mecânica e de Materiais da Universidade Tecnológica Federal do Paraná.

Orientador: Prof. Dr. Rigoberto Eleazar Melgarejo Morales.

CURITIBA

2021

Ministério da Educação
Universidade Tecnológica Federal do Paraná
Campus Curitiba

JOEL ROBERT KARP

THE DYNAMICS OF COMPOUND DROPS RISING IN A QUIESCENT VISCOUS FLUID

Trabalho de pesquisa de doutorado apresentado como requisito para obtenção do título de Doutor Em Engenharia da Universidade Tecnológica Federal do Paraná (UTFPR). Área de concentração: Engenharia Térmica.

Data de aprovação: 15 de Dezembro de 2021

Prof Rigoberto Eleazar Melgarejo Morales, Doutorado - Universidade Tecnológica Federal do Paraná

Prof Amadeu Kun Wan Sum, Doutorado - Colorado School Of Mines

Prof Fabricio Soares Da Silva, Doutorado - Petróleo Brasileiro - Petrobras

Prof Marcio Da Silveira Carvalho, Doutorado - Pontifícia Universidade Católica do Rio de Janeiro (Puc-Rio)

Prof Moises Alves Marcelino Neto, Doutorado - Universidade Tecnológica Federal do Paraná

Documento gerado pelo Sistema Acadêmico da UTFPR a partir dos dados da Ata de Defesa em 07/02/2022.

ACKNOWLEDGEMENTS

This thesis was elaborated and conducted in the Multiphase Flow Research Center (NUEM) at the Federal University of Technology of Paraná (UTFPR). May I extend my sincerest gratitude to everyone in this group. A special and very fond "*thank you*" goes to Rigoberto E. M. Morales, who introduced me to the domain of *fluid mechanics* and mentored me through this challenge. For my part, it is and has always been a privilege working with you.

This work was conducted in a close collaboration with Ernesto Mancilla, researcher at NUEM, Dominique Legendre, professor at the *Institut de Mécanique des Fluides de Toulouse*, Yunxing Su, postdoctoral associate at Brown University, and Roberto Zenit, professor at Brown University. At the conception of this work, I could never have hoped to learn from so many talented people. I am deeply grateful for this opportunity.

The valor of a scholarly work cannot be separated from the competence of the people judging it. Thus, I would like to express my gratitude to the members of the examination board for their support in the evaluation of this work. Special thanks to Rigoberto E. M. Morales for presiding the board. Moisés A. M. Neto, professor at NUEM, Márcio Carvalho, professor at PUC-RIO, Fabrício Soares, research associate at PETROBRAS – CENPES/PDIDP/ESUP/TPMF, and Amadeu Sum, professor at Colorado School of Mines, please accept my gratitude.

The true education starts at home. In that spirit, special thanks to my family for educating me and shaping my character. To my wife, Tatiane, the assurance that our family will always be my most cherished treasure in this world. Thanks for your love, encouragement, and so many other things that I don't deserve. Thank you, Ronald and Solange, my parents and first *mentors*, for preparing me to life and all its nuances. Also, Susan and Tiago, Jonathan and Camile, and Jessé and Ana, brothers and sisters, thank you. Through all of you, I experience the endless love of God. Through my work, I stand amazed at the complexity of God's creation; it took me no less than four years to get only a sketchy glimpse of the fluid mechanics of a tiny compound drop…

The scientific endeavor henceforth presented was made possible through the financial contribution bestowed by CENPES/PETROBRAS, TC. 5850.0106833.18.9. I acknowledge the funding from this company.

"…with humility comes wisdom."
(Proverbs 11:2)

RESUMO

KARP, Joel Robert. **Dinâmica de Gotas Compostas Escoando em um Fluido Viscoso Estagnado**. Tese - Programa de Pós-Graduação em Engenharia Mecânica e de Materiais, Universidade Tecnológica Federal do Paraná. Curitiba, 120 p., 2021.

Gotas compostas são partículas fluidas compostas por mais de um fluido. Sua estrutura complexa rege seu comportamento, cujo conhecimento é de importância em vários cenários envolvendo escoamento multifásico. O presente trabalho é dedicado à análise do movimento gravitacional de gotas compostas gás-líquido de tamanho na ordem de milímetros com alto número de Reynolds, aproximadamente de 70 a 700, em um fluido viscoso quiescente por meio de técnicas de visualização de escoamento. Para tanto, experimentos em ambiente isotérmico utilizando as técnicas de aquisição de imagens em alta velocidade e velocimetria de imagem de partículas (PIV) foram conduzidos no Laboratório de Visualização de Escoamentos nas dependências do Núcleo de Escoamento Multifásico (NUEM - UTFPR). A influência das propriedades dos fluidos e da geometria da gota composta foi investigada empregando diferentes fluidos (óleos de silicone, milho, e mineral) e alterando o tamanho da bolha interna. Dois regimes ascendentes foram identificados com base em uma faixa crítica de razão de diâmetro, a saber, os regimes retilíneo e oscilatório. Os efeitos governantes em cada regime de movimento foram discutidos. As gotas compostas preservaram sua forma esférica em todas as medições, sugerindo que o escoamento interno pode desempenhar um papel essencial na transição do movimento. O comportamento oscilatório é descrito pelos ângulos de orientação das fases da gota composta que seguem um movimento pendular. A bolha interna reduz a dissipação viscosa e o coeficiente de arrasto apresentou valores intermediários em relação às gotas e bolhas monofluido. A instabilidade da esteira é sugerida como a origem física das instabilidades na trajetória. Quando o tamanho da bolha excede um valor crítico, a simetria da esteira é perdida devido ao aumento da vorticidade. O número de Strouhal apresentou uma evolução diferente em comparação com bolhas, gotas e esferas, revelando diferentes mecanismos de oscilação. Essas observações são corroboradas por modelagem mecanicista e suportadas por dados experimentais.

Palavras-chave: Instabilidade da trajetória, coeficiente de arraste, gota composta, esteira, modelagem

ABSTRACT

KARP, Joel Robert. **The Dynamics of Compound Drops Rising in a Quiescent Viscous Fluid**. Thesis - Postgraduate Program in Mechanical and Materials Engineering, Federal University of Technology - Parana. Curitiba, 120 pages, 2021.

Compound drops are fluid particles composed by more than one fluid phase. Their complex structure governs their dynamic behavior, whose knowledge is of the utmost importance in several multiphase flow applications. The present work is devoted to the analysis of the gravitational motion of millimeter-sized gas-liquid compound drops in a quiescent viscous fluid at high Reynolds numbers, from 70 to 700 roughly, by means of flow visualization techniques. With this aim, experiments in an isothermal environment employing the high-speed shadowgraph and particle image velocimetry (PIV) techniques were conducted in the Flow Visualization Laboratory within the premises of the Multiphase Flow Research Center (NUEM – UTFPR). The influence of the properties of the fluids and the geometry of the compound drop was investigated by employing different fluids (silicone, corn, and mineral oils) and altering the size of the internal bubble. Two rising regimes were identified based on a critical range of diameter ratios, namely the rectilinear and the oscillatory motions. The governing effects of each motion regime were discussed. The compound drops preserved their spherical shape through all the measurements, suggesting that the internal fluid movement might play an essential role in the motion transition. The oscillatory behavior is described by the orientation angles of the phases of the compound drop that follow a pendular-like motion. The internal bubble reduces the viscous dissipation and the drag coefficient presented intermediate values compared to single-fluid drops and bubbles. The unsteadiness of the wake is at the onset of path instabilities. When the size of the bubble exceeds a critical value, the symmetry of the wake is lost due to the increased vorticity. The Strouhal number showed a different evolution compared to bubbles, drops, and spheres, revealing different mechanisms of oscillations. These observations are corroborated by mechanistic modeling and supported by the experimental data.

Keywords: Path instability, drag coefficient, compound drop, wake, modeling

NOMENCLATURE

Roman letters:

a	Geometrical parameter of the compound drop
b	Geometrical parameter of the compound drop
C_d	Drag coefficient of the compound drop
C_d^d	Drag coefficient of a single-fluid drop
C_d^s	Drag coefficient of a rigid sphere
C_d^b	Drag coefficient of a single-fluid bubble
C_{cd}^*	Normalized drag coefficient of the compound drop
d_b	Equivalent diameter of the internal phase of the compound drop
d_{cd}	Equivalent diameter of the compound drop
$\boldsymbol{F_g}$	Archimedes force
$\boldsymbol{F_d}$	Drag force
$\boldsymbol{F_i}$	Inertial force
$\boldsymbol{F_v}$	Viscous dissipation force
Fr	Froude number
Fr^*	Modified Froude number
$\boldsymbol{F_L}$	Lift force
$\bar{F}_L$	Time-averaged lift force
f_p	Pendular oscillation frequency
f	Frequency of velocity fluctuations
f_0	Surface oscillation of a drop in inviscid flow
f_s	Frequency of vortex shedding
$\boldsymbol{g}$	Acceleration of gravity
H	Width of the external fluid at the bottom segment of the compound drop
h	Width of the external fluid at the top segment of the compound drop
I	Turbulence intensity
k	Prefactor employed in the modeling of the drag coefficient of compound drops in oscillatory motion
l	Distance between the external centroid and the top of the compound drop
l_c	Distance between the vortex centers in the wake of a compound drop
l_w	Characteristic dimension of the interrogation window used in the PIV measurements
M_{cd}	Major axis of the compound drop
m_{cd}	Minor axis of the compound drop
M_b	Major axis of the internal phase of the compound drop
m_b	Minor axis of the internal phase of the compound drop
n	Exponent employed in the modeling of the drag coefficient of compound drops in oscillatory motion
P	Power-law coefficient employed in the modeling of the drag coefficient in rectilinear motion
r_b	Equivalent radius of the internal phase of the compound drop
St	Strouhal number
St_p	Strouhal number of the pendular oscillation
St_s	Strouhal number based on vortex shedding frequency

S_0	Spreading coefficient
t	Time
t_θ	Time threshold for linear behavior of the orientation angle of the external phase of the compound drop
t_ω	Time threshold for linear behavior of the orientation angle of the internal phase of the compound drop
$\boldsymbol{V_{cd}}$	Rising velocity of the compound drop
V_z	Vertical component of the rising velocity of the compound drop
V_x	Horizontal component of the rising velocity of the compound drop
v_z	Velocity component of the continuous liquid in the z direction
v_y	Velocity component of the continuous liquid in the y direction
v_x	Velocity component of the continuous liquid in the x direction
v_x'	Temporal fluctuations of the velocity component of the continuous liquid in the x direction
v_y'	Temporal fluctuations of the velocity component of the continuous liquid in the y direction
$\bar{v}_x$	Time-averaged velocity component of the continuous liquid in the x direction
$\bar{v}_y$	Time-averaged velocity component of the continuous liquid in the y direction

Dimensionless numbers:

Re	Reynolds number
Bo	Bond number
We	Weber number
Mo	Morton number
$We_{o/g}$	Internal Weber number
$Bo_{o/g}$	Internal Bond number

Greek letters:

α	Constant used in the modeling of the aspect ratio of the internal fluid
γ	Constant used in the modeling of the aspect ratio of the internal fluid
Γ	Interfacial tension
δ	Distance travelled by the external centroid of the compound drop
ϵ	Eccentricity of the compound drop
θ	Orientation angle of the external phase of the compound drop
θ_{max}	Orientation angle of the external phase of the compound drop at the inflexion point
θ^*	Normalized orientation angle of the external phase of the compound drop
ϑ_{cd}	Volume of the compound drop
ϑ_b	Volume of the internal phase of the compound drop
λ	Wavelength of the pendular oscillation
Λ_θ	Amplitude of the orientation angle of the external phase of the compound drop
Λ_ω	Amplitude of the orientation angle of the internal phase of the compound drop
Λ_{V_x}	Amplitude of fluctuations of the horizontal component of the rising velocity of the compound drop
Λ^*	Normalized amplitude of the orientation angles of the compound drop
μ	Dynamic viscosity of the continuous fluid
μ_b	Dynamic viscosity of the internal phase of the compound drop

μ_o	Dynamic viscosity of the external phase of the compound drop
μ_{cd}	Effective dynamic viscosity of the compound drop
ρ	Density of the continuous fluid
ρ_b	Density of the internal phase of the compound drop
ρ_o	Density of the external phase of the compound drop
ρ_{cd}	Effective density of the compound drop
σ	Interfacial tension coefficient at the gas-water interface
$\sigma_{g/o}$	Interfacial tension coefficient at the oil-gas interface
$\sigma_{o/w}$	Interfacial tension coefficient at the oil-water interface
τ	Fluid circulation
φ	Viscosity ratio
φ'	Effective viscosity ratio
φ_ω	Time lag of the external phase of the compound drop
χ_{cd}	Aspect ratio of the compound drop
χ_b	Aspect ratio of the internal phase of the compound drop
ω	Orientation angle of the internal phase of the compound drop
ω_y	Normal vorticity ($x-z$ plane)
ω_z	Streamwise vorticity ($x-y$ plane)
ω^*	Normalized orientation angle of the internal phase of the compound drop

LIST OF FIGURES

LIST OF TABLES

TABLE OF CONTENTS

1 INTRODUCTION

Compound drops appear in several multiphase flows in which the dispersed phase contains more than one fluid (Neeson et al., 2012; Mandal et al., 2016). Such objects consist of a liquid drop, immersed in an immiscible fluid, that contains a gas bubble or another immiscible liquid drop within it. Their study has received attention over the years because of their prevalence in industry and medical applications.

In pharmaceutics, compound drops enable the synthesis of structured colloids, increasing the stability of the formed emulsions as well as the shelf life of the product (Abate & Weitz, 2009). In some medical procedures, compound drops can be intravenously administered into the blood stream to enhance ultrasound scattering, as illustrated in Figure 1-1. This procedure increases the diagnosis potential of tumor micro metastases, for example (Lindner, 2004; Sijl et al., 2010).

Figure 1-1. Application of compound drops in medical procedures.

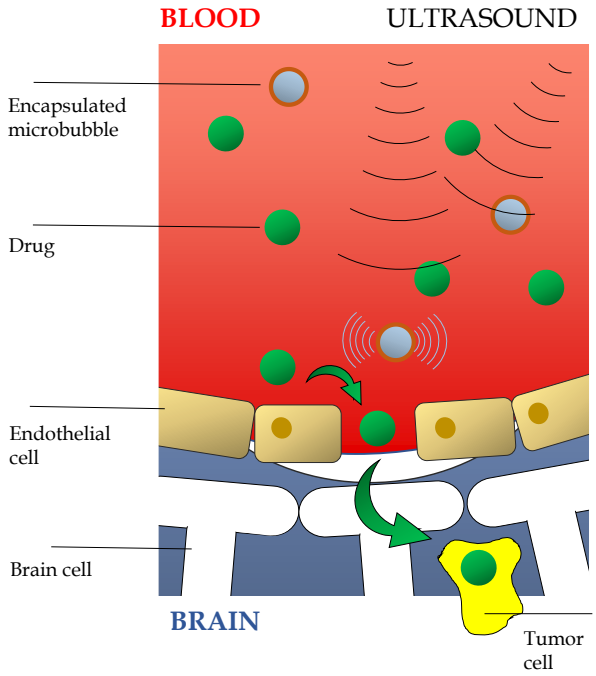

Source: own authorship.

Compound drops are also encountered in magmatic eruptions (Mungal et al., 2015). The multiphase flow inside a volcano is composed primarily by hot magma with

water vapor bubbles and drops of undissolved sulphide, whose interaction may form gas-liquid compound drops. They float to the eruption site carrying sulfurous gases, whose emission is of environmental concern.

The effectiveness of primary oil separation also relies on the formation of compound drops. In a flotation unit, oil drops are removed from the produced water by inserting gas bubbles into the stream (Saththasivam et al., 2016). Those bubbles attach themselves to the drops and increase their terminal velocity. The treated water is then safely disposed into the environment, in accordance with the increasingly rigorous environmental legislation.

Figure 1-2. Scheme of compound drop formation within a gas flotation cell in oil recovery systems.

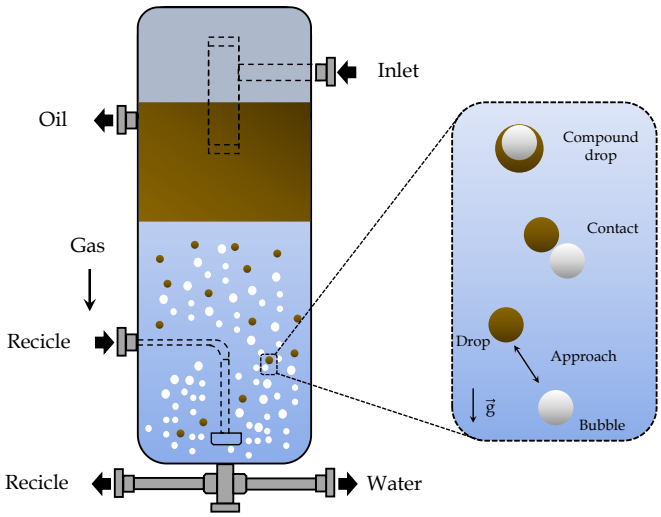

Source: own authorship.

The successful application of the aforementioned processes relies on the knowledge of the dynamic behavior of the compound drops under gravitational motion in a viscous fluid. Up to the present date, the design and operation of such separation vessels on offshore oil platforms are based on daily observations by operating personnel, whereas details regarding the formation of the compound drops and the influence of the internal bubble on the separation efficiency – to name just a few – have yet to be accounted for.

1.1 Objectives

The main objective of this work is to experimentally investigate the dynamic behavior of gas-liquid compound drops rising in a viscous fluid for a wide range of Reynolds numbers. To achieve this, different geometrical parameters and combinations of fluids will be tested.

The following specific objectives were also outlined:

1) Investigate the configuration and shape of the compound drops;
2) Analize the path and rising velocity and propose a transition criterion for path instabilities;
3) Model the drag coefficient of the compound drops and compare with typical single-fluid particles;
4) Investigate the effect of the compound structure in the dynamics of the oscillatory motion;
5) Investigate the structure of the wake behind a compound drop and propose an underlying physical mechanism for the occurance of path instabilities.

1.2 Contribution of the present work

In the context of the aforementioned objectives, the general contribution of this work is to provide a detailed analysis of the dynamics of the compound drop for more realistic scenarios based on experiments and modeling that aim to fill the existing gap in literature. Other specific contributions can also be outlines:

1) The effect of inertia on the dynamics of the compound drops is investigated over a wide range of Reynolds numbers;
2) An intermediate behavior was observed for the terminal velocity of the compound drop, when compared to single-fluid particles;
3) Similarly, the drag coefficient lies within the lower and upper limits of a single-fluid bubble and a rigid sphere, respectively, as corroborated by the modeling herein proposed;
4) The wake instability is at the onset of path oscillations that consist of a pendular oscillation;
5) A different dynamics is observed for the wake behind an oscillating compound drop; a direct consequence of their compound nature.

1.3 General presentation

Chapter 2 reviews the existing literature on the motion of compound drops, after which the contribution of the present research is discussed. The experimental methodology is described in detail in chapter 3. The design of the apparatus as well as the image processing algorithm are described.

The mechanistic modeling of the drag coefficient of the compound drops is presented in chapter 4 along with a description of the temporal parameters of the oscillatory motion. Chapter 5 is devoted to the general dynamics of the compound drops rising in a viscous fluid. With this aim, measurements of the rising path, terminal velocity, shape, and drag coefficient are presented. The analysis of the structure of the wake behind the compound drop is developed in chapter 6 where a physical mechanism for the origin of the oscillations is presented.

Finally, the main conclusions drawn from the analysis of the results are discussed in chapter 7. Moreover, some insights towards the future prospects of the research in compound drop dynamics are sketched.

2 LITERATURE REVIEW

This chapter provides a theoretical background regarding the dynamics of compound drops and a review of the specific literature. The contribution of the present research is depicted by describing the peculiarities of each study, focusing on the assumptions considered and the phenomena analyzed by the researchers. Firstly, the main aspects of the hydrodynamics of the motion of compound drops are presented in section 2.1. Focus is given to the configurations adopted by the compound drops, the forces acting on them, and the relevant dimensionless numbers. Then, a review of the specific literature is given at section 2.2.

2.1 Hydrodynamic aspects

The multiphase nature of the compound drops herein evaluated offers an increased structural complexity that makes the investigation of their dynamics far from trivial. This section provides an essential introduction to the main aspects of their dynamic behavior. Firstly, the possible configurations adopted by the fluids composing the compound drops are described based on the interfacial properties. Then, the compound nature of the drop is taken into account to describe the main hydrodynamic forces acting on it. Finally, the effect of these forces is evaluated in terms of the relevant dimensionless numbers.

2.1.1 Equilibrium configurations

According to Torza & Mason (1970), when two immiscible fluids - henceforth designated as Fluid 1 and Fluid 2 - interact when suspended in a third continuous fluid (Fluid 3), the equilibrium configuration is classified in terms of the resultant interfaces, as shown in Figure 2-1. The interfacial tension coefficients – designated here as σ – and the radii r are also shown for each configuration. The interfacial tension coefficient seems a suitable parameter for the estimation of the equilibrium configuration since it arises from the cohesion at the fluid interface and is, therefore, related to its interfacial

energy. Thus, a higher interfacial tension coefficient implies in the minimization of the interfacial area. It can be seen from Figure 2-1 that depending on the combination of the interfacial tension coefficients, specific equilibrium configurations can be adopted as a consequence of the spreading of the fluids. Note that in this example the terminology *surface tension* is avoided, given that no restrictions were applied to the composition of the fluids, i.e., they can be either a gas or a liquid.

In this example, the fluid with greater interfacial tension coefficient is designated as Fluid 1 ($\sigma_{1/3} > \sigma_{2/3}$). In the case of a neutrally buoyant compound drop, the final equilibrium state is determined by a balance between the interfacial tensions of the fluids and is classified as:

- *Non-engulfed*

This configuration (Figure 2-1a) is characterized by the non-engulfment of the fluids. It occurs when Fluid 1 and Fluid 2 are in contact but without fluid spreading. The non-engulfed configuration corresponds to a condition where the spreading of Fluid 2 over Fluid 1 is not thermodynamically favorable, i.e., $\sigma_{1/2} > \sigma_{1/3} + \sigma_{2/3}$. In that case, the resultant interface between Fluid 1 and Fluid 2 (with $\sigma_{1/2}$) would increase the overall interfacial energy of the system;

- *Completely engulfed*

Figure 2-1b shows that a complete engulfment occurs when Fluid 2 completely spreads over Fluid 1. It opposes to the non-engulfed configuration since the contact between Fluid 1 and Fluid 2 yields the formation of a single multiphase compound. This equilibrium configuration is encountered when $\sigma_{1/3} > \sigma_{1/2} + \sigma_{2/3}$, for which the interfacial energy of the compound drop is reduced when the interface between Fluid 1 and Fluid 3 disappears completely;

- *Partially engulfed*

Figure 2-1c shows the intermediate equilibrium configuration, where the spreading of Fluid 2 over Fluid 1 occurs partially. Thus, an additional interface

between Fluid 1 and Fluid 2 is formed, but both fluids still keep their interface with Fluid 3. As one might expect, this final state is achieved when none of the aforementioned conditions is fully met, i.e., $\sigma_{1/2} < \sigma_{1/3} + \sigma_{2/3}$ and $\sigma_{1/3} < \sigma_{1/2} + \sigma_{2/3}$.

Figure 2-1. Equilibrium configurations of a compound drop. (a) Non-engulfed, (b) completely engulfed, and (c) partially engulfed. The interfacial tensions and equivalent ratios are displayed for each fluid phase. The dash-dotted line represents the axis of symmetry.

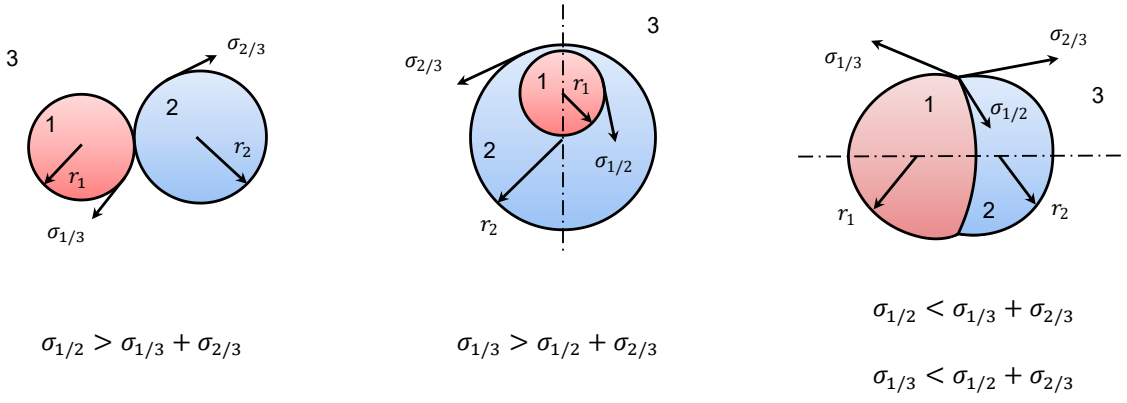

$\sigma_{1/2} > \sigma_{1/3} + \sigma_{2/3}$

$\sigma_{1/3} > \sigma_{1/2} + \sigma_{2/3}$

$\sigma_{1/2} < \sigma_{1/3} + \sigma_{2/3}$

$\sigma_{1/3} < \sigma_{1/2} + \sigma_{2/3}$

a) b) c)

Source: adapted from Torza & Mason (1970).

Note that the estimation of the equilibrium configurations shown in Figure 2-1 do not take gravitational effects into account. Thus, for a rising compound drop where buoyant effects are relevant – the case of the compound drops studied here –, some deviations from the equilibrium configurations shown in Figure 2-1 may be observed depending on the motion parameters.

2.1.2 *Forces acting on a compound drop*

Let us consider a single compound drop with clean interfaces rising at terminal conditions in a quiescent and viscous fluid. The completely engulfed configuration (Figure 2-1b) is considered for the compound drop. As will be later corroborated by the experiments, this condition agrees well with the system of fluids herein investigated. For this configuration, Fluid 1 and Fluid 2 are typically denoted as the internal and external fluids, respectively, as schematically shown in Figure 2-2.

Water was chosen as the continuous fluid, whereas air and oil correspond to the internal and external fluids, respectively. The density and dynamic viscosity of each fluid are designated as ρ and μ, respectively. The subscripts b and o refer to the internal and external fluids, respectively. The interfacial tension coefficient is represented as σ, with the subscripts g/o and o/w referring to the internal and external interfaces, respectively. The equivalent diameter of the internal fluid and the compound drop are designated respectively by d_b and d_{cd}.

The main forces acting on a compound drop rising under gravitational motion in a uniform flow are shown in Figure 2-2. Insomuch as the compound drop is submitted to a gravitational field, $\boldsymbol{g}$, it experiences a force that arises from the density difference in respect to the continuous fluid. This is known as the Archimedes force, $\boldsymbol{F_g}$, the resultant between the buoyancy and weight forces; $\boldsymbol{F_g}$ is the driving force of buoyancy-driven flows and is calculated according to Legendre (1996):

$$\boldsymbol{F_g} = (\rho - \rho_{cd})\vartheta_{cd}\boldsymbol{g} \qquad 2\text{-}1$$

where ρ_{cd} is the effective density of the compound drop that will be defined later (Eq. 3-4). The volume of a spherical compound drop, ϑ_{cd}, is:

$$\vartheta_{cd} = \frac{1}{6}\pi d_{cd}^3 \qquad 2\text{-}2$$

In the case of a stationary, quiescent, and uniform flow, the only supplementary force that acts on the compound drop is the viscous drag, $\boldsymbol{F_d}$. For a spherical compound drop, the viscous drag is expressed by:

$$\boldsymbol{F_d} = \frac{1}{8}\pi\rho C_d d_{cd}^2 \boldsymbol{V_{cd}^2} \qquad 2\text{-}3$$

where C_d and $\boldsymbol{V_{cd}}$ are the drag coefficient and terminal velocity of the compound drop, respectively. C_d is a dimensionless parameter to quantify the drag force and numerous models to predict this parameter are found in literature (Magnaudet, 1997).

Figure 2-2. Scheme of the Archimedes and drag forces acting on a rising compound drop. The equivalent diameters and fluid properties of each phase are also shown.

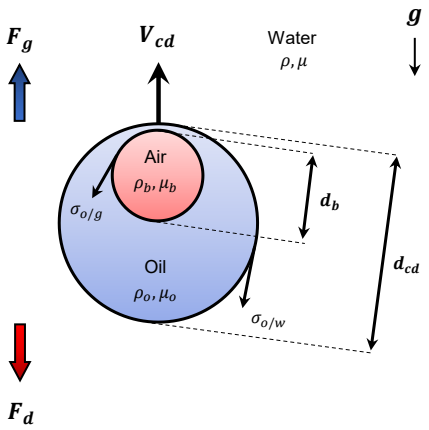

Source: own authorship.

The gravitational motion of the compound drop is then determined by the aforementioned forces. Note that the force balance represented by Eq. 2-1 and Eq. 2-3 is simplified, insomuch as the instabilities that arise from the non-uniformities of the flow are not considered. As will be evidenced by the experiments, other forces may be taken into account depending on the rising regime of the compound drop. This subject will be addressed later in this text. For now, this simplified approach is sufficient to derive the governing dimensionless numbers of the motion.

During its rise, the compound drop experiences the effect of inertia as a consequence of the relative momentum of the flow. This effect is measured by the inertial force, $\boldsymbol{F_i}$, calculated as proposed by Zhou et al. (2020):

$$\boldsymbol{F_i} = \rho \boldsymbol{V_{cd}^2} d_{cd}^2 \qquad 2\text{-}4$$

Similarly, some amount of work has to be done to deform the continuous fluid as the compound drop flows through it. This is a direct consequence of the viscosity of the fluid and is measured by the viscous force, $\boldsymbol{F_v}$, calculated as:

$$\boldsymbol{F_v} = \mu \boldsymbol{V_{cd}} d_{cd} \quad \text{2-5}$$

Because of inertia, the shape of the compound drop may no longer be spherical. This deformation occurs when the magnitude of $\boldsymbol{F_i}$ is sufficiently large to overcome the work necessary to deform the interface of the compound drop, Γ, calculated as:

$$\Gamma = \sigma_{o/w} d_{cd} \quad \text{2-6}$$

2.1.3 Dimensionless numbers

The gravitational motion of the compound drop is characterized by the relative magnitude of the effects of inertia (Eq. 2-4), viscosity (Eq. 2-5), and interfacial tension (Eq. 2-6). They are represented by dimensionless groups that govern the motion. The Reynolds number, Re, is defined as the ratio between the inertial effects and the viscous dissipation:

$$Re = \frac{\rho V_{cd} d_{cd}}{\mu} \quad \text{2-7}$$

Thus, the effect of inertia is negligible at low Reynolds numbers ($Re < 1$), for which the terminologies *creeping flow* or *Stokes flow* are frequently used. The present study, however, focuses on the flow of compound drops at high Reynolds numbers, i.e., when inertial effects are dominant. The buoyancy-driven motion of millimeter-sized particles usually fall into that category.

Under those circumstances, the fluid particle might be deformed. Thus, the characterization of their shape requires the evaluation of the effect of interfacial tension over inertia or gravity. The Bond and Weber numbers, denoted here as Bo and We, respectively, are frequently used with this aim. Many correlations provide the shape distortion as a function of these two parameters. They are defined as:

$$Bo = \frac{(\rho - \rho_{cd}) g d_{cd}^2}{\sigma_{o/w}} \quad 2\text{-}8$$

$$We = \frac{\rho V_{cd}^2 d_{cd}}{\sigma_{o/w}} \quad 2\text{-}9$$

The Morton number, Mo, is also used in conjunction with the aforementioned dimensionless parameters to consider the properties of the fluids. For the compound drops herein evaluated, Mo is defined as:

$$Mo = \frac{g\mu^4(\rho - \rho_{cd})}{\rho^2 \sigma_{o/w}^3} \quad 2\text{-}10$$

Note that since the compound drop has two interfaces, the definitions of Bo, We, and Mo are not straightforward. For now, only the external interface is considered and $\sigma_{o/w}$ is taken as the relevant interfacial tension coefficient.

2.2 Literature review

This section describes the state-of-the-art of the literature regarding the dynamics of compound drops in different flow conditions. Focus is given on the description of the main motion parameters for which the present work provides specific contribution. This work focuses on the case of completely engulfed compound drops (Figure 2-1b). For this configuration, the compound drops may assume a nearly spherical shape and a symmetry axis along the line connecting the two centroids (dash-dotted line in Figure 2-1b). Note that the position of the internal and external centroids may or may not coincide, for which the compound drop is classified as concentric or eccentric, respectively. The details regarding the structure of the compound drop depend on several parameters, as will be outlined in this section. The shape of a compound drop is firstly considered. A review of the models of the drag coefficient and the behavior of the velocity is also provided. Then, their interfacial stability is

briefly addressed. Finally, the concepts related to the structure of the wake behind a compound drop and the onset of path instabilities are introduced.

2.2.1 Shape and velocity

As opposed to regular drops and bubbles, the fluid inclusion increases the structural complexity of the compound drops (see Figure 2-1b). Naturally, the configuration of the compound drop affects the flow parameters, e.g., rising path, terminal velocity, and shape deformation (Torza & Mason, 1970). To understand the motion of compound drops is therefore a challenging task, despite the efforts done by several researchers to comprehend their dynamic behavior.

Torza & Mason (1970) were among the first to experimentally investigate the three-phase interactions covering a vast range of the configurations of the compound drops. The engulfment process of a liquid-liquid compound drop is shown in Figure 2-3. The water drop (left) is completely engulfed by the polyglycol drop (right). Furthermore, a theoretical analysis of the configuration of static compound drops was included, albeit restricted to flows with the absence of gravitational effects.

Figure 2-3. Steps in the engulfing process of a water drop (left) and a polyglycol drop (right) in silicone oil brought together in a combined shear and electrical field.

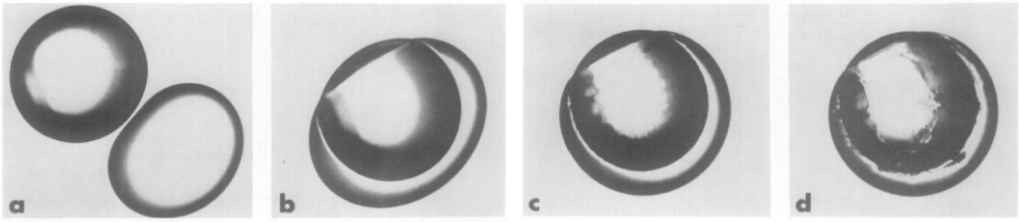

Source: Torza & Mason, 1970.

Further researchers investigated the case of a gas-liquid compound drop, e.g., when a gas bubble is engulfed by a liquid drop. Focus was given on the dynamics of the gravitational motion of these particles, also designated as coated or encapsulated bubbles. Hayakawa & Shigeta (1974) reported that their terminal velocity and drag coefficient are mainly governed by the volume ratio, that is, the relative volume of the

bubble with respect to the external liquid. However, the authors reprieved a detailed fluid mechanical analysis of the motion.

Mori and collaborators (1977) studied the influence of the properties of the fluids in the terminal velocity. The relative size of the bubble in comparison to the drop seemed to govern the motion; interestingly, the properties of the continuous fluid had a minor effect in the terminal velocity. They compared the motion of their compound drops with theoretical predictions that do not consider the effect of inertia. Similar conclusions were drawn by Mercier et al. (1974) for the case of evaporating drops and condensing bubbles, where the compound drop is composed by one fluid only.

Figure 2-4. (a) Silicone oil coated bubble rising in deionized water; and (b) shape of an uncoated (bottom) and silicone oil coated (top) bubbles in water.

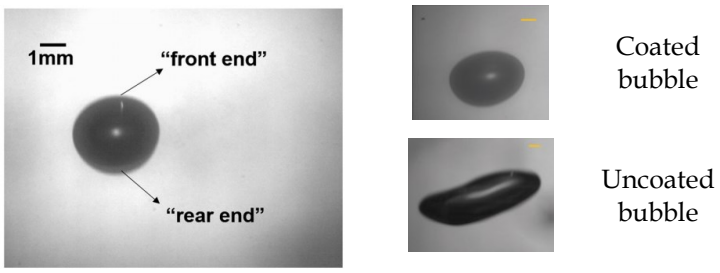

Source: Wang et al., 2018.

Recently, it was observed that when oil coats a rising bubble it significantly affects its shape and terminal velocity (Wang et al., 2018). Most of the motion parameters showed an intermediate behavior in comparison to single-fluid bubbles and drops of correspondent magnitude; thus, the relative size of the compound drop may be a useful parameter to characterize the motion of the particles, based on their multiphase nature. Figure 2-4 illustrates how the compound structure of the drop affects its shape. The compound drops adopted an eccentric configuration (Figure 2-4a), where the oil is placed essentially at the "rear end" of the compound drop due to the density difference. This equilibrium configuration led to a compound drop with nearly spherical shape, opposed to a typical bubble of comparable size (Figure 2-4b).

An analytical expression of the terminal velocity of compound drops was firstly presented, presumably independently, by Johnson & Sadhal and Rushton & Davies in

1983. Their models of the drag force consider the diameter and viscosity ratios of the compound drop. Rushton & Davies (1983) considered the internal phase as a rigid sphere, whereas Johnson & Sadhal (1983) used the lubrication theory to address the flow by considering the external liquid as a thin film. Both studies presented similar results with the compound drop having intermediate behavior between the Stokes and Hadamard & Rybczynscki solutions (Clift et al., 1978). However, the effect of shape deformation was not evaluated, given that the models are restricted to creeping flows.

Brunn & Roden (1985) also proposed a model for the drag of concentric compound drops in creeping flow. To enable an analytical solution, interfacial deformation was neglected by considering high values of interfacial tension. The compound drops behaved similarly to a rigid sphere when the external fluid was reduced to a thin film, suppressing the internal circulation. Thus, the compound drop is virtually a stationary fluid engulfed by an immobile shell. Furthermore, Brunn & Roden (1985) analyzed the conditions where mild inertial forces are added to the system, after which the compound nature of the drop appears to govern the motion and a concentric configuration is prevented.

Over the past few decades, advances in computational methods have permitted the study of compound drops in more detail and for a wider range of parameters. Kawano & Hashimoto (1997) numerically studied the steady viscous flow past a sphere coated with a thin liquid film. Their simulations covered a Reynolds number up to 200 and analyzed the influence of physical properties of the fluid, as well as diameter and volume ratios. The authors extended the theory of Rushton & Davies (1983) and obtained an empirical model for the drag coefficient of compound drops at moderate Reynolds numbers. They found out that the drag of a compound drop behaves similarly as a rigid sphere, a probable consequence of the imposed considerations, mainly the absence of a disjoining pressure.

Other recent numerical endeavors focused on specific applications of compound drops such as interactions in an ultrasound field (Liu et al., 2018), effect of surface contamination (Mandal et al., 2016) and microfluidics (Vu et al., 2019).

2.2.2 *Compound drop stability*

The conditions of breakup of a spherical compound drop in Stokes flow was analyzed by Patzer & Homsy (1975) by means of a hydrodynamic stability theory. A stable concentric configuration was reported, with a critical film thickness of approximately 9000 Å for which the breakup occurs. However, the analysis was simplified by neglecting inertia and the density difference between the fluids. Landman (1985) investigated the shape oscillations of compound drops in potential flow. They addressed the stability of a concentric compound drop composed by Newtonian fluids. The compound drops are disturbed from their motionless spherical shape, followed by a damping phenomenon and out-of-phase displacements of the compound drop interfaces, according to the scheme shown in Figure 2-5.

Figure 2-5. Configurations of the compound drop: (a) out-of-phase oscillations; and (b) in-phase oscillations.

a) b)

Source: Landman, 1985.

Bazhlekov and collaborators (1995) extended this analysis to compound drops with eccentric configuration. They used a finite-element numerical simulation at moderate Reynolds number to address the shape evolutions and reported the formation of a thin film at the front end of the compound drop that experiences a swift draining process that leads to the breakup of the compound drop.

Numerical studies also suggested that the presence of a fluid inclusion may increase the stability of compound drops in Stokes flow (Stone & Leal, 1990). Two modes of breakup were reported based on the distortion of the compound drop. The first mode refers to conditions of continuous extension; the second mode is caused by interfacial incompatibility for less distorted systems. In both scenarios, the presence of

the internal phase favors the destabilization of the compound drop in comparison to correspondent single-phase drops because of the formation of a thin film between the interfaces, as illustrated in Figure 2-6.

Figure 2-6. Complete numerical simulation of deformation of compound drops in a uniaxial extensional flow.

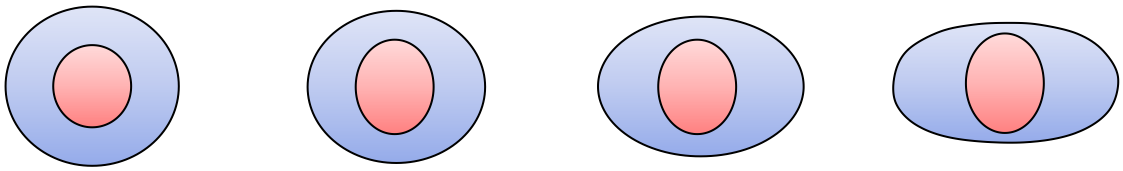

a) b) c) d)

Source: Stone & Leal, 1990.

Hua et al. (2014) studied the non-breakup behavior of the compound drop employing the immersed boundary method. They found the diameter ratio to be the major influential parameter in the three-dimensional shape deformation. The effect of the capillary number and the initial location of the inner drop were also evaluated. By employing similar numerical methods, it was also observed that the relative size influences the stability of compound drops (Hua et al., 2014; Chen et al., 2015).

Recent endeavors focused on the stability of compound drops in more specific flow situations. Chaithanya & Thampi (2019) further addressed the stability of rotating concentric compound drops. The authors reported values of the force required to stabilize the compound drops in imposed flows in an inertia-less limit, and proposed a pulsatile flow of the continuous phase as the proper transport mechanism in order to prevent rupture. Deka et al. (2019) suggested that the coalescence dynamics of compound drops is similar to typical drops, as long as the fluid inclusion is small. However, the compound structure of the drop seemed to affect its impact onto a liquid pool, as investigated by Zhu et al. (2020). The authors also suggested that the compound drops may not be stable under certain impact conditions. A review of the underlying mechanisms governing the impact of compound drops in liquid and rigid surfaces may be found elsewhere (Blanken et al., 2021).

2.2.3 *Path instabilities and wake structure*

It is well known that fluid particles may experience path oscillations induced by the inertia of the flow (Ern et al., 2012). Although this phenomenon is now nearly completely understood for air bubbles (Zenit & Magnaudet, 2009) and liquid drops (Albert et al., 2015), it remains unanswered for rising compound drops. For instance, millimeter-sized bubbles rising in water present either a zigzagging or spiraling path, opposed to smaller bubbles that rise in a straight line (Wu & Gharib, 2002). In the past few decades, many researchers have converged to a common conclusion to explain this behavior: the oscillations arise when the wake behind the particle becomes unstable due to subsequent symmetry breakdowns when a critical value of vorticity is reached (Magnaudet & Mougin, 2007; Zenit & Magnaudet, 2009).

However, for the case of compound drops, an underlying mechanism for path instability to occur has yet to be reported. To the best of the current knowledge, the only study regarding the structure of the wake behind a compound drop had been conducted by Bazhlekov and collaborators (1995). The inertia of the flow led to a compound drop with a deformed shape with minor flow circulation behind it, as shown in Figure 2-7. However, no further information is available regarding the stability of this wake structure nor its connection to the onset of path instabilities.

Figure 2-7. Streamlines around a deformed and eccentric gas-liquid compound drop.

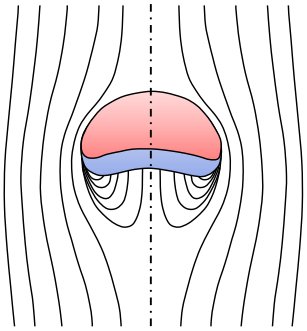

Source: Bazhlekov et al., 1995.

The structure of the wake of a compound drop remains mostly unexplored to date. Thus, it is convenient to outline the major characteristics of the wake dynamics

of typical particles, e.g., gas bubbles, liquid drops, and rigid spheres, to check whether or not the compound drops will show a similar structure.

Figure 2-8. Isosurfaces of streamwise vorticity isovorticity surfaces in the wake of an oscillating bubble.

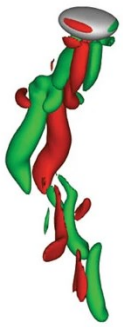

Source: Tripathi et al., 2015.

The wake behind a rising bubble has been experimentally documented for the first time by Lunde & Perkins (1998) and Brücker (1999) using flow visualization techniques. In summary, the wake structure resembled the one of a rigid sphere with the presence of two counter-rotating trailing vortices at the bottom segment of the bubble. Furthermore, the periodic shedding of vortices led to specific three-dimensional structures denoted as *hairpin vortices*, as shown in Figure 2-8.

The instability of the wake emerged as a likely phenomenon to characterize the appearance of path instabilities. Direct numerical simulations by Mougin & Magnaudet (2001) and Magnaudet & Mougin (2007) for stress-free ellipsoidal bubbles corroborated this hypothesis. They showed that the unsteadiness of the wake is unambiguously the onset of path oscillations. The wake behind a bubble is stable and axisymmetric with the instabilities arising due to sequential symmetry breakdowns. Yang & Prosperetti (2007) reached a similar conclusion using a linear stability theory.

Further experiments conducted by Zenit & Magnaudet (2009) for a clean bubble corroborated these observations. When the aspect ratio of the bubble exceeds a critical value, the generated vorticity behind the bubble creates two vorticity tubes that induce a horizontal force on the bubble. Thus, the sideways motion is triggered, characterizing the path instabilities. Moreover, the authors proposed the streamwise vorticity as the

key parameter for the path instabilities to appear when the bubble is rising in a low viscosity fluid. It should be noted that Zenit & Magnaudet (2009) were pioneers in the experimental characterization of the three-dimensional structure of the wake behind a rising bubble. As shown in Figure 2-9, the wake of a bubble in zigzagging motion consists of two vortex tubes that decrease with the distance from the bubble, in excellent agreement with previous numerical simulations.

Figure 2-9. Isovorticity surfaces in the wake of an oscillating bubble (black line). Images (left and right) show different views of the same flow.

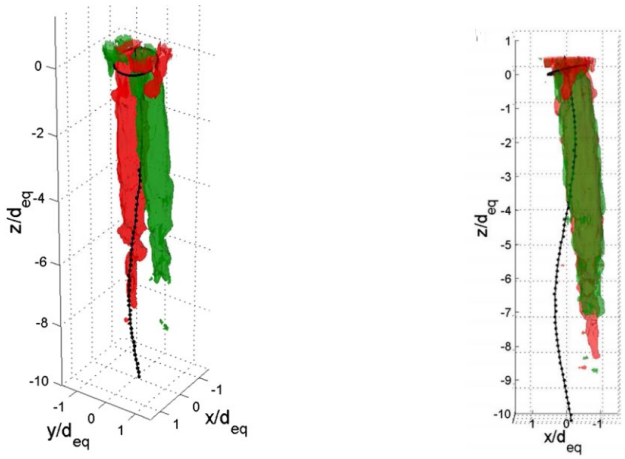

Source: Zenit & Magnaudet, 2009.

2.3 Final remarks

The literature review presented in this chapter is summarized in Table 2-1. For each topic discussed earlier, the main references are presented for bubbles, drops, rigid spheres, and compound drops. The goal is to identify the gaps in the existing literature and provide a suitable background for the analysis presented in this study.

As Table 2-1 indicates, the understanding of the motion parameters that were outlined is consolidated only for the typical particles, for which a wider range of parameters were evaluated and validated experimentally. As for the compound drops, most studies are restricted to creeping flow among other simplifications. Apparently, few studies offered some experimental validation for their claims. Thus, experiments involving compound drops are still valuable. This work aims to investigate some of these topics by using the experimental methodology presented in chapter 3.

Table 2-1. Review on the literature of bubbles, drops, rigid spheres, and compound drops. The status of each motion parameter is classified as "well documented" (blue marker) or "incomplete" (yellow marker) based on the range of conditions evaluated.

	Bubbles		Drops		Spheres		Compound drop	
	Status	References	Status	References	Status	References	Status	References
Trajectory	✓	[2, 7, 12, 16, 18, 19, 27, 31, 40, 44, 70, 71, 72, 73, 76]	✓	[1, 9, 10, 12, 17, 19, 27, 69]	✓	[12, 19, 53]	✓	[23, 38, 67]
Shape	✓	[2, 7, 12, 16, 18, 19, 27, 29, 34, 35, 39, 40, 70, 71, 72, 73, 76]	✓	[1, 4, 9, 10, 12, 17, 19, 27, 46, 68, 69]	n/a	-	✓	[3, 6, 8, 11, 13, 15, 22, 23, 25, 28, 33, 36, 38, 41, 42, 45, 56, 61, 67]
Velocity	✓	[2, 12, 16, 18, 19, 27, 29, 30, 31, 35, 40, 70, 71, 72, 76]	✓	[1, 9, 12, 17, 19, 27, 69]	✓	[12, 19, 35, 51]	✓	[21, 23, 24, 26, 38, 49, 67]
Drag	✓	[12, 18, 19, 30, 31, 35, 37, 46, 59, 71, 76]	✓	[1, 9, 12, 19, 52, 69]	✓	[12, 19, 35, 46, 50, 51, 53]	✓	[6, 23, 24, 26, 49]
Stability	✓	[5, 12, 16, 27, 34, 71]	✓	[10, 12, 17, 27]	n/a	-	✓	[3, 8, 11, 13, 14, 22, 23, 28, 32, 33, 43, 45, 55, 56, 57, 63, 74]
Wake	✓	[7, 12, 18, 19, 30, 35, 40, 47, 48, 62, 71, 73]	✓	[1, 9, 12, 19, 46, 69]	✓	[12, 19, 20, 35, 50, 58]	✓	[3]

Source: [1] Albert et al. (2015); [2] Aoyama et al. (2016); [3] Bazhlekov et al. (1995); [4] Becker et al. (1991); [5] Biesheuvel & Winjgaarden (1984); [6] Brunn & Roden (1985); [7] Brücker (1999); [8] Chaithanya & Thampi (2019); [9] Charin et al. (2019); [10] Chebel et al. (2012); [11] Chen et al. (2015); [12] Clfit et al. (1978); [13] Das et al. (2020); [14] Deka et al. (2019); [15] Dudek & Oye (2018); [16] Duineveld (1995); [17] Edge & Grant (1971); [18] Ellingsen & Risso (2001); [19] Ern et al. (2012); [20] Ghidersa & Dusek (2000); [21] Hayakawa & Shigeta (1974); [22] Hua et al. (2014); [23] Johnson & Sadhal (1985); [24] Johnson & Sadhal (1983); [25] Kan et al. (1998); [26] Kawano & Hashimoto (1997); [27] Lalanne et al. (2015); [28] Landman (1985); [29] Legendre et al. (2012); [30] Legendre (1996); [31] Lindt & de Groot (1974); [32] Liu et al. (2016); [33] Kiu et al. (2021); [34] Lunde & Perkins (1997); [35] Magnaudet & Mougin (2007); [36] Mandal et al. (2016); [37] Mei et al. (1994); [38] Mercier et al. (1974); [39] Moore (1965); [40] Mougin & Magnaudet (2001); [41] Mori (1978); [42] Mori et al. (1977); [43] Patzer & Homsy (1975); [44] Prosperetti et al. (2003); [45] Qu & Wang (2012); [46] Rachih et al. (2020); [47] Riboux et al. (2013); [48] Roig et al. (2012); [49] Rushton & Davies (1983); [50] Sakamoto & Haniu (1990); [51] Schiller & Naumann (1933); [52] Selecki & Gradon (1976); [53] Segré & Silberbeg (1962); [54] Shankar & Subramanian (1983); [55] Song et al. (2010); [56] Stone & Leal (1990); [57] Stroeve & Varanasi (1984); [58] Tamboulides & Orszag (2000); [59] Tomiyama et al. (1998); [60] Torza et al. (1972); [61] Torza & Mason (1970); [62] Tripathi et al. (2015); [63] Tsamopoulos & Brown (1987); [64] Ulbrecht et al. (1972); [65] De Vries et al. (2002); [66] Vu et al. (2019); [67] Wang et al. (2018); [68] Wellek et al. (1966); [69] Winnikov & Chao (1966); [70] Wu & Gharib (2002); [71] Yang & Prosperetti (2007); [72] Zenit & Magnaudet (2008); [73] Zenit & Magnaudet (2009); [74] Zhang et al. (2016); [75] Zhou et al. (2006); [76] Zhou et al. (2020); [77] Zhu et al. (2020).

3 EXPERIMENTAL METHODOLOGY

This chapter describes the experimental techniques used to investigate the dynamics of compound drops. Section 3.1 describes the experimental setup for the high-speed shadowgraph visualization. The behavior of the continuous phase is analyzed using the particle image velocimetry (PIV) technique shown in section 3.2.

3.1 High-speed shadowgraph

The experiments were conducted in a 700 – mm high glass tank with a 150 – mm wide rectangular cross-section filled with tap water, as shown schematically in Figure 3-1. The liquid was at room temperature (kept at 20 ºC using an air conditioning system) and atmospheric pressure. An acrylic dish (thickness of 10 mm) made the base of the tank where two capillary tubes were placed to generate the bubbles and drops.

Figure 3-1. Sketch of the experimental apparatus used for the visualization of the motion of compound drops.

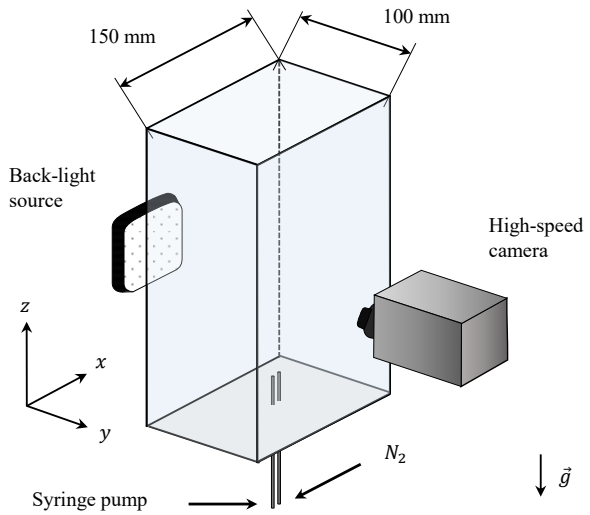

Source: own authorship.

Different systems of capillaries with several internal diameters were used with this aim. While the size of the oil drop was kept nominally constant by using one capillary size, the size of the air bubbles was varied by using capillaries of different

internal diameters. In this way, the diameter ratio of the gas bubble and oil droplet was varied. Both the gas bubbles and oil drops were produced by means of the pinch-off method. The oil was injected by means of a pump and flowed through a capillary; the oil injection stopped once the droplet was formed. The droplet diameter was approximately 2.5 mm for all tests. The gas was injected through the second capillary tube, generating bubbles with an equivalent diameter ranging from 0.3 to 3.0 mm. Then, the bubble-drop compound was formed by manually manipulating the distance between the capillaries, moving the bubble slowly towards the drop.

As shown in Figure 3-2, the gas bubble is completely engulfed by the drop, with the oil surrounding the bubble. For the range of parameters tested here, the compound drop is eccentric; hence, the bubble is not surrounded by a uniform distribution of oil, as shown in Figure 3-2, and in agreement with Wang et al. (2018). The distribution of the oil shell depends on the volume of the internal bubble, since the droplet volume is kept fixed. The compound droplets formed by this method were stable and slightly deformed with an axisymmetric shape. The composition of the compound drops was quantified by considering the size ratio d_b/d_{cd}, where d_b and d_{cd} are the equivalent diameters of the internal bubble and the compound drop, respectively.

3.1.1 Measurements and image processing

Two different sets of measurements to characterize the dynamic behavior of the compound drops were designed, where both transient and stationary motions were captured. Firstly, the three-dimensional rise of the compound drops was obtained with a single high-speed camera (Photon SA4, Nikkon 60 mm). The camera was located in front of the cell to capture the $x-z$ movement. To obtain the entire particle trajectory a mirror was placed at 45º with respect to the lateral wall, so that the $y-z$ view could be recorded simultaneously. Additionally, an illumination system consisting of a LED lamp located in a backlight configuration was set to capture the contour of the drops. The mirror was also used to reflect light for the side view. From these measurements, the three-dimensional paths were reconstructed for each compound drop. This methodology was also used to carry out the transient motion experiments.

Figure 3-2. The compound drop formation process: the series of images show the bubble-drop attachment process, considering air and Oil 1 (see Table 3-1). The bubble and drop (on the left and right of image (a), respectively) diameters before attachment were 3.1 and 2.5 mm, respectively. Images (a) shows the initial contact between the phases; (b - e) the engulfment process of the oil over the surface of the bubble; (f - i) the detachment of the compound drop from the capillary and the initial stage of gravitational motion.

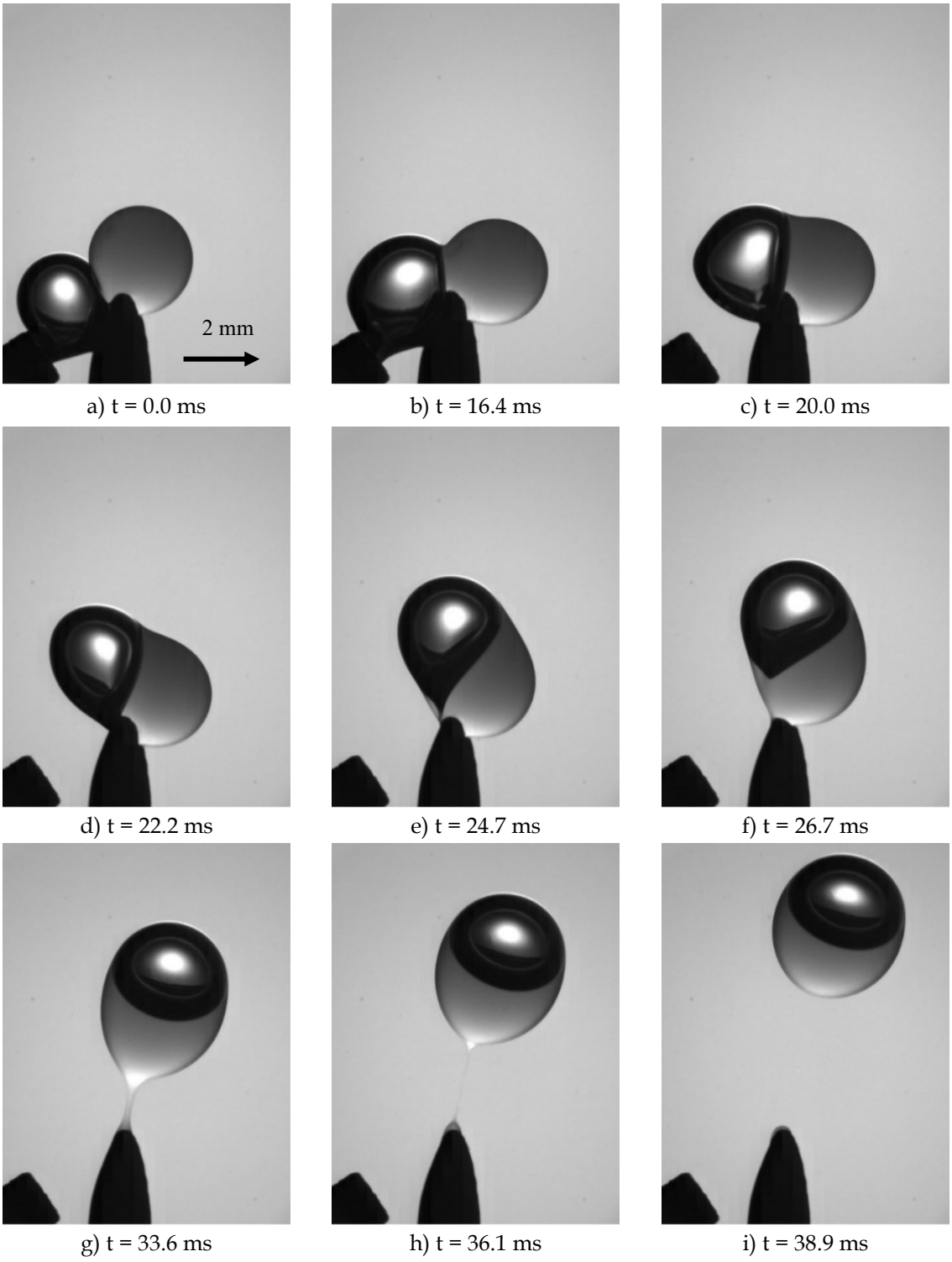

a) t = 0.0 ms b) t = 16.4 ms c) t = 20.0 ms

d) t = 22.2 ms e) t = 24.7 ms f) t = 26.7 ms

g) t = 33.6 ms h) t = 36.1 ms i) t = 38.9 ms

Source: own authorship.

A second set of images was also obtained to provide a more detailed visualization of the two different phases within the compound drop. The camera was placed higher (roughly 200 mm above the capillary bank) to ensure that the motion of the compound drop has achieved its terminal state. A high-magnification lens system (12X, LaVision) was used for capturing the stationary frontal-view of the rising compound drops. This methodology enabled the phase segmentation of the compound drop where both the internal and external fluids were analyzed separately.

The images were processed using MATLAB®. Light non-uniformity and edge noise were reduced by standard image processing techniques. The images were then binarized. For the first set of measurements, aimed at determining the compound droplet trajectory, the image processing and binarization parameters were chosen to detect the external interface only.

The second set of measurements of the image processing enabled the detection of both interfaces of the compound drop. This procedure is illustrated in Figure 3-3. From the raw image (Figure 3-3a), the external interface was characterized by simply detecting the contour of the compound drop (Figure 3-3b). As for the detection of the internal interface, two different conditions were recognized from the measurements of the compound drop formation. The first one referred to small internal bubbles that kept their nearly spherical shape even after the engulfment process, whereas the second condition involved larger internal bubbles that assumed an ellipsoidal shape.

Figure 3-3. Image processing procedure of a compound drop.

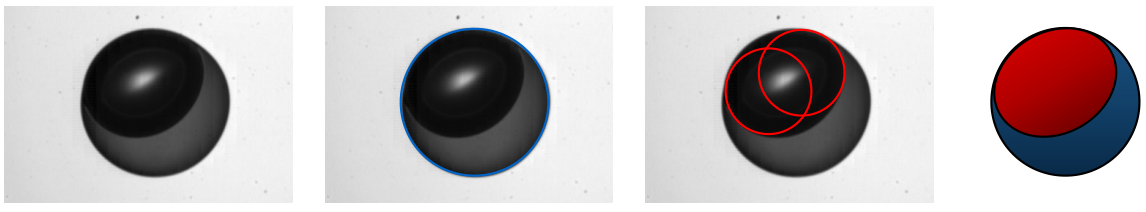

(a) Raw image (b) External interface (c) Internal interface (c) Phase segmentation

Source: own authorship.

When the bubble is not distorted, the detection of the boundary was conducted by detecting spherical objects in the image. On the other hand, when the bubble is

deformed, a shape recognition methodology was developed for the characterization of the ellipsoidal contour from the identification of two spherical circles (Figure 3-3c). Finally, Figure 3-3d presents the processed compound drops with phase segmentation, which was composed by the junction of the previously detected interfaces. This allowed each phase of the compound drop to be analyzed separately.

The volume of the compound droplet was obtained from the image processing, considering the 2D projection and the second theorem of Pappus, which states that the volume of a solid of revolution generated by the displacement of a lamina over an external axis is equal to the product of the area of such lamina by the distance travelled by its centroid. In the present case, the lamina to be rotated was a representative circle of the internal bubble, obtained by averaging the parameters of the two individual circles identified in the detection methodology. This averaged circle was rotated around the axis of symmetry of the object. The distance travelled by the lamina was calculated as the perimeter of the ellipsis formed as the centroid of the representative circle rotated around the axis. This ellipsis is described by the parameters a and b which are, respectively, related to the major and minor axis of the internal bubble, as illustrated in Figure 3-4b. The calculation of the internal bubble volume followed this procedure according to:

$$\vartheta_b = 2\pi \sqrt{\frac{a^2 + \left(\frac{ba}{a + r_b}\right)^2}{2}} \pi r_b^2 \qquad 3\text{-}1$$

The shape of both fluid phases can be obtained thanks to the phase segmentation algorithm described above. The aspect ratio of the compound drop, χ_{cd}, and the internal bubble, χ_b, were calculated as:

$$\chi_{cd} = \frac{M_{cd}}{m_{cd}} \quad , \qquad \chi_b = \frac{M_b}{m_b} \qquad 3\text{-}2$$

where M_i and m_i are the long and short axes, respectively. The suffix i can either be cd for the compound drop or b for the bubble, as depicted in Figure 3-4. The equivalent diameter of the compound drop, d_{cd}, was calculated as:

$$d_{cd} = (M_{cd}^2 \cdot m_{cd})^{\frac{1}{3}} \qquad 3\text{-}3$$

assuming that the shape was close to that of an ellipsoid; d_b was obtained directly from the volume of the internal bubble (Eq. 3-1). Note that these calculations were based on a 2D projection of the compound drops.

Figure 3-4. Scheme of the long and short axes for: a) compound drop; and b) internal bubble. The yellow, green and blue dots indicate the center of mass of the compound drop, internal bubble and external fluid, respectively. Geometric parameters are also shown.

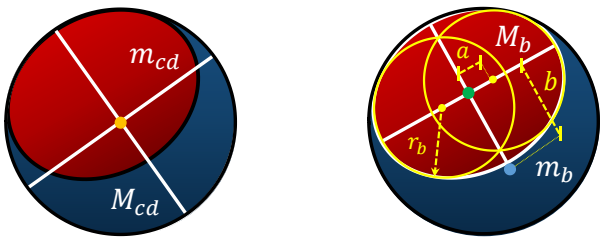

Source: own authorship.

The shape recognition methodology described earlier provided measurements of the geometrical parameters of the compound drop with adequate accuracy. However, some uncertainties are intrinsic to the Hough transform routine that was applied to the images for contour detection; since a certain quantity of pixels around the interfaces fell in a range of grayscale tones, the threshold applied to the algorithm provides fluctuating contours for the compound drop. Based on the standard deviation of the measurements, the uncertainties can be estimated as less than 2 %. Note that this is a rough estimation, since it depends on the quality of each frame.

The cross-section of the compound drop was analyzed by measuring the width of the external phase at the bottom (H) and top (h) segments of the compound drop along the axis of symmetry (black line shown in Figure 3-5). The widths were

measured by attributing a specific value for each fluid phase - 1 and 0 for the pixels detected in the oil and bubble segments, respectively - and evaluating the value to each pixel along the axis of symmetry. Therefore, H and h were calculated as the distance for which every pixel equaled the unity. The distance between the external and internal centroids of the compound drop (blue and red dots in Figure 3-5, respectively) was defined as the eccentricity ϵ of the compound drop.

Figure 3-5. Representative scheme of the geometrical parameters of an oscillating compound drop.

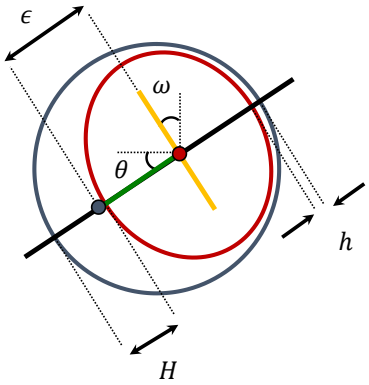

Source: own authorship.

Figure 3-5 also shows that the axes of the compound drop are not aligned with the vertical direction, i.e., the compound drop is inclined with regard to the Cartesian system shown in Figure 3-1. The orientation of the inner bubble was defined as the acute angle ω formed by the major axis (yellow line) with the vertical axis. Similarly, the orientation of the external phase θ was the acute angle formed by the green line with the horizontal axis. Accordingly, a maximum inclination was observed for $\theta \to 0$ and $\omega \to 0$, when the compound drop was perpendicular to the vertical axis; on the other hand, a straight alignment was observed for $\theta, \omega \to 90°$.

3.1.2 Test fluids and operating conditions

Three different oils were used to test the effect of the drop viscosity, density and interfacial tension. The properties of these fluids are shown in Table 3-1. Nitrogen (99.98% purity) was used as the gas, and tap water was used as the continuous fluid. Note that the condition of complete engulfment (see Figure 2-1b) is met for all fluids.

Table 3-1. Physical properties of the working fluids used for the experimental measurements.

Fluid	Density $[kg/m^3]$	Viscosity $[Pa.s]$ x 10^{-3}	Interfacial tension $[mN/m]$		
	ρ	μ	σ	$\sigma_{o/w}$	$\sigma_{o/g}$
Tap water	998	1.002	73.5	-	-
Oil 1 (silicone oil, 47V350, Rhodorsil)	970	350	-	41.1	21.1
Oil 2 (commercial corn oil)	915	59	-	26.0	31.6
Oil 3 (mineral oil, 330779, Sigma-Aldrich)	838	13	-	18.0	28.6

Source : Gaonkar, 1989; Huang et al., 1997; Bashir et al., 2014.

It is necessary to define an effective density of the compound drop, i.e., the density of the individual fluids averaged by their relative size. For that purpose, an evaluation of the influence of the bubble size has to be considered to obtain a working density and to observe the influence of this parameter on the dynamics of the compound drops. Accordingly, since density is defined as the mass of a fluid contained in a certain volume, the final size of the compound drop was taken into account to quantify the effective density of the compound drop, expressed in the dimensionless form:

$$\rho_{cd}/\rho_o = 1 - \left(\frac{d_b}{d_{cd}}\right)^3 \qquad 3\text{-}4$$

where the subscript o refers to the oil phase. Accordingly, ρ_{cd}/ρ_o represents the effective density of the compound drop with regard to the density of the external fluid. Essentially, it accounts for the reduction in density promoted by the engulfment process. Note that this parameter is used in the definition of the dimensionless numbers defined earlier.

Table 3-2 presents the operating range of the dimensionless numbers that govern the motion of the compound drops, previously defined in chapter 2. The data are shown for all the experimental measurements conducted in the present work, enabling a comparison with the existing literature. The magnitude of the Reynolds (Eq. 2-7), Bond (Eq. 2-8), Weber (Eq. 2-9), and Morton (Eq. 2-10) numbers illustrates the

relevance of hydrodynamic effects acting on the compound drop as a function of the physical properties of the working fluids and the geometry of the compound drops.

Table 3-2. Range of evaluated dimensionless numbers for the produced compound drops for all measurements.

	Oil 1	Oil 2	Oil 3
d_b/d_{cd}	0.14 – 0.94	0.14 – 0.86	0.15 – 0.83
Reynolds	62 - 732	197 - 616	201 – 706
Bond	0.040 – 2.00	0.20 – 1.90	0.35 – 2.50
Weber	0.045 – 3.45	0.55 – 4.40	0.95 – 7.60
Morton	4.4×10^{-12} - 1.2×10^{-10}	2.8×10^{-10} - 9.5×10^{-10}	4.8×10^{-11} - 3.1×10^{-10}

Source: own authorship.

3.2 Particle image velocimetry (PIV)

To analyze the structure of the wake of a rising compound drop, a particle image velocimetry (PIV) system was implemented, as shown in Figure 3-6. The chamber was the same as previously shown in Figure 3-1. The laser sheet can be aligned vertically or horizontally in respect to the height the chamber to measure the velocity perturbation in the $x - z$ and $x - y$ planes, respectively. The flow was seeded with neutrally buoyant B-Rhodamine particles that acted as fluorescent tracers to reduce the reflections at the interfaces of the compound drop. A high-speed camera - same system used in the shadow measurements - was used to capture the motion of the tracers together with a continuous laser used to illuminate the PIV measurement region.

The software FlowMaster (LaVision, Germany) was used to process the typical PIV images. The algorithm is based on an interactive multi-pass routine. Interrogation windows with final size of 32 x 32 pixels with an overlap of 50 % in both directions were used. The characteristic dimension of the interrogation area l_w was approximately 1 mm for all the measurements, ensuring a minimum of 15 tracer particles per window. Near the external contour of the compound drop, measurements

closer than l_w presented significant noise caused by reflection. Moreover, in this region the displacement of the particles between sequential frames was frequently greater than one quarter of the interrogation window. Thus, the velocity field was not calculated in this region and a geometric mask was added to the image as a pre-processing stage.

Figure 3-6. Experimental arrangement for the PIV measurements. Flow field detection in the $x-z$ (a) and $x-y$ (b) planes. The visualization chamber is the same from in Figure 3-1.

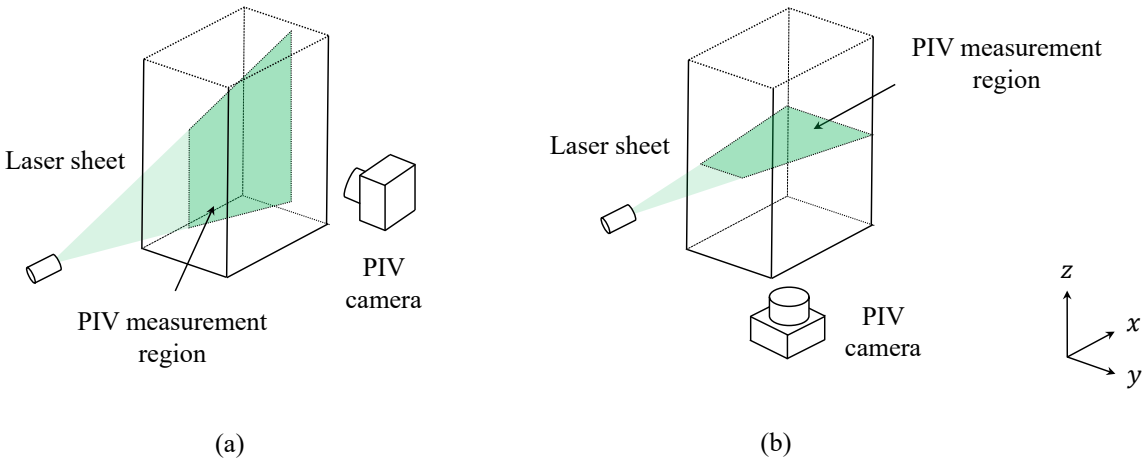

Source: own authorship.

Subsequently, a validation of the correlation value was carried out, together with the application of special filter routines. The vorticity normal to the flow, ω_y, and the streamwise vorticity, ω_z, were calculated, respectively, as the curl of the velocity field in the $x-z$ and $x-y$ planes:

$$\omega_y = \frac{\partial v_z}{\partial x} - \frac{\partial v_x}{\partial z}, \qquad \omega_z = \frac{\partial v_y}{\partial x} - \frac{\partial v_x}{\partial y} \tag{3-5}$$

3.2.1 Operating conditions

Three representative cases were chosen to be investigated with the PIV methodology, as listed in Table 3-3. As will be discussed later, those cases had specific values of diameter ratio d_b/d_{cd} that corresponded to a rectilinear motion, transitory flow, and fully developed oscillating motion. In all cases, Oil 1 was chosen as the

external fluid. Preliminary tests indicated that these three conditions represented well the motion of the compound drops in different regimes.

Table 3-3. Conditions analyzed with the PIV methodology. The external fluid is Oil 1.

Case	Motion	d_{cd} (mm)	d_b/d_{cd}	Re
1	Straight	2.52	0.28	59
2	Transition	2.72	0.61	319
3	Oscillating	3.06	0.77	412

Source: own authorship.

Figure 3-7. 2D trajectories of compound drops at terminal conditions. The cases are the same from Table 3-3. Solid and dotted lines represent the position of the external and internal centroids in the $x-z$ plane, respectively.

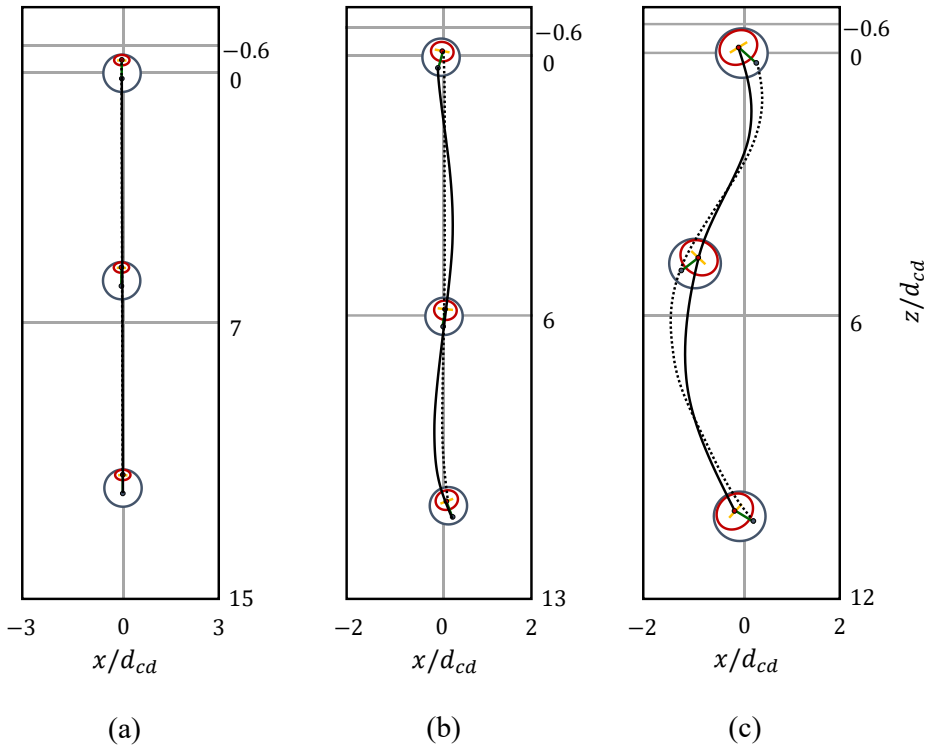

Source: own authorship.

To illustrate the conditions analyzed in the PIV experiments, the rising path of the compound drops is briefly presented in Figure 3-7 for each case listed in Table 3-3. Note that the position of the compound drop in the $x-z$ plane was made dimensionless by d_{cd}. Also, the vertical position was set to zero at the final position of the compound drop (the position is approximated by neglecting the internal fluid).

Above the compound drop, z/d_{cd} is negative, whereas positive values are found behind the compound drop. Note that, a prior, the trajectory of the compound drops appears to fluctuate in the $x-z$ plane only. Details regarding the evolution of the rising regime with d_b/d_{cd} will be presented in chapter 5.

Figure 3-8 shows sample images obtained with the PIV methodology for the cases listed in Table 3-3. The superposition of the images enabled the qualitative visualization of the velocity field in the $x-z$ and $x-y$ planes (top and bottom rows, respectively). The contours of the compound drop are also shown for the sake of clarity. A direct comparison with Figure 3-7 suggests that the regions with swirling fluid are connected to the path of the compound drop, as will be discussed in detail in chapter 6.

Figure 3-8. Fluid motion for compound drop for the cases listed in Table 3-3. Top row shows frontal images of cases 1 (a), 2 (b), and 3 (c), respectively. Accordingly, bottom row shows the streamwise measurements.

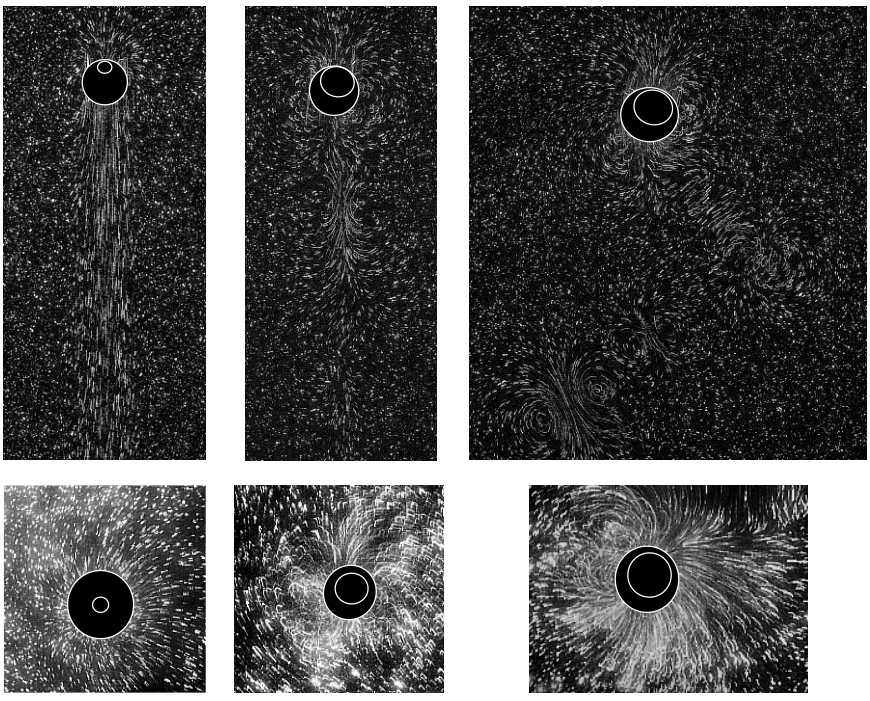

(a) (b) (c)

Source: own authorship.

4 MECHANISTIC MODELING

This chapter presents the mechanistic modeling of some of the relevant parameters of the motion of the compound drops. Section 4.1 proposes a modeling of the drag coefficient of compound drops in rectilinear motion. The transient behavior of the orientation of the compound drop is described in section 4.2 as a function of the geometry of the compound drop.

4.1 Drag coefficient of a spherical compound drop

This section aims to describe the drag coefficient of a single compound drop rising in quiescent water in rectilinear motion. The estimation of the drag coefficient, C_d, is crucial in buoyant flows where the drag determines the magnitude of the terminal velocity. So far, the models that have been proposed for the determination of the C_d of compound drops rely on the absence of inertial forces.

The drag coefficient can be experimentally calculated according to the force balance schematically shown in Figure 2-2. The balance between the Archimedes (Eq. 2-1) and drag (Eq. 2-3) results in the following expression:

$$C_d = \frac{4gd_{cd}(\rho - \rho_{cd})}{3\rho V_{cd}^2} \qquad 4\text{-}1$$

Note that the estimation of the drag coefficient by Eq. 4-1 is a simplified approach since the following assumptions were herein considered:

1) The shape of the compound drop is spherical;
2) The hydrodynamic effects that arise from the non-uniformities of the flow, in particular the lift force, are absent.

These assumptions may or may not be adequate depending on the motion. For instance, for an ellipsoidal bubble, Eq. 4-1 is inaccurate and a different estimation for the C_d is required (Ellingsen & Risso, 2001). However, according to Figure 3-2, the

compound drops studied here seem to be virtually spherical at terminal conditions. Further details regarding the shape of the compound drops will be presented later. Moreover, it is a common practice in gravitational flows to only consider forces that have a vertical component to calculate the C_d. Thus, as chapter 6 will show, even though a significant horizontal component of the lift force may be identified for oscillating compound drops, the estimation by Eq. 4-1 is fair (Sanada et al., 2008). Nonetheless, there are several flow situations where other forces should be considered, e.g., bubble motion in a cross-flow, hydrofoils, to name just a few.

The first step towards the modeling of C_d is to describe the dynamic behavior of a spherical compound drop in rectilinear motion, as schematically shown in Figure 4-1. Note that the compound drop shown below is analogous to the force balance scheme depicted in Figure 2-2 where the Archimedes and drag forces are outlined. Additional attention is now given to the flow inside the fluids comprising the compound drop, insomuch as the drag of a fluid particle is greatly affected by its inner circulation (Clift et al., 1978).

Firstly, the pressure component of the drag is disregarded by neglecting the presence of a wake; however, inner circulation and distribution of pressure should be influenced by the presence of a fluid inclusion. Ideas to describe the drag coefficient of a compound drop based on that assumption are now presented.

Figure 4-1. Flow pattern of a single compound drop rising in straight motion at terminal conditions.

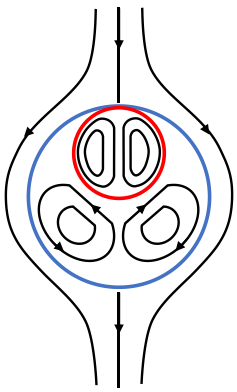

Source: own authorship.

4.1.1 Proposal 1

The first approach is based on the assumption of Hadamard & Rybczynski that states that the drag coefficient of a drop, C_d^d, with viscosity μ_o in creeping flow is described by a modified Stokes solution:

$$C_d^d = \frac{24}{Re}\left(\frac{2 + 3\varphi}{3 + 3\varphi}\right) \qquad 4\text{-}2$$

where $24/Re$ is the classical solution for the drag coefficient of a sphere in the Stokes regime and φ is the viscosity ratio of the drop:

$$\varphi = \frac{\mu_o}{\mu} \qquad 4\text{-}3$$

that evaluates the internal shear and pressure distribution in terms of the relative viscosity of the fluid particle (Clift et al., 1978). Thus, as it can be seen from Eq. 4-2, the internal flows of a fluid particle act towards the reduction of its drag coefficient in comparison to a rigid sphere. Additionally, the viscosity of the fluid particle governs this behavior; the reduction in the drag coefficient is inversely proportional to φ.

However, Eq. 4-2 is valid for Stokes flow ($Re < 1$) only, which is not the case of the compound drops herein considered (see Table 3-2). If the assumption of Hadamard & Rybczynski is extended to a fluid sphere at high Reynolds number, Eq. 4-2 becomes:

$$C_d^d = C_d^s\left(\frac{2 + 3\varphi}{3 + 3\varphi}\right) \qquad 4\text{-}4$$

where C_d^s can be calculated from the classical Schiller & Naumann (1933) correlation for a rigid sphere with $Re < 1000$. This correlation has been extensively used in the past decades to account for the effect of inertia on the drag coefficient. The correlation is given by:

$$C_d^s = \frac{24}{Re}(1 + 0.15Re^{0.687}) \quad 4\text{-}5$$

Moreover, the calculation of φ is not straightforward for the compound drop because of the internal bubble. However, an expression for the effective viscosity of the compound drop, μ_{cd}, can be derived analogously to its effective density defined by Eq. 3-4. If the reduction in the drag coefficient is more pronounced for a less viscous fluid particle as a consequence of the pressure distribution, it could be expected that the internal bubble is responsible for an additional reduction in the C_d of a compound drop. Therefore, $\mu_{cd} < \mu_o$ and Eq. 4-4 can be written as a function of an effective viscosity ratio, that accounts for the presence of the internal bubble:

$$\varphi' = \frac{\mu_{cd}}{\mu} \quad 4\text{-}6$$

where μ_{cd} is obtained by averaging the viscosity of each fluid phase in terms of the volume ratio:

$$\mu_{cd} = \mu_b\left(\frac{d_b}{d_{cd}}\right)^3 + \mu_o\left[1 - \left(\frac{d_b}{d_{cd}}\right)^3\right] \quad 4\text{-}7$$

For the compound drops studied here, $\mu_b \ll \mu_o$; thus, the effective viscosity becomes:

$$\mu_{cd} = \mu_o\left[1 - \left(\frac{d_b}{d_{cd}}\right)^3\right] \quad 4\text{-}8$$

and an expression for the drag coefficient of a compound drop is given:

$$C_d = C_d^s \left(\frac{2 + 3\varphi'}{3 + 3\varphi'} \right) \quad 4\text{-}9$$

The effective viscosity ratio of the compound drop is obtained by dividing Eq. 4-8 by μ. Thus, the effect of the internal circulation on the drag coefficient of the compound drop is considered by the following term:

$$\varphi' = \varphi \left[1 - \left(\frac{d_b}{d_{cd}} \right)^3 \right] \quad 4\text{-}10$$

The use of Eq. 4-9 and Eq. 4-10 provides the C_d of a compound drop, based on the drag coefficient of a rigid sphere with the same Reynolds, for which extensive modeling can be found in literature. The compound nature of the drop promotes a reduction in its drag coefficient that depends on the viscosity of the internal and external fluids, as well as the diameter ratio. However, the estimation of the effective viscosity μ_{cd} is based on an averaging of the viscosities of the individual fluids, which is clearly an approximation insomuch as the compound drop keeps its multiphase structure, i.e., the fluids are immiscible. Thus, the set of correlations grouped in Eq. 4-9 and Eq. 4-10 provides no further physical insight, but it can be a useful tool to estimate the drag coefficient of a compound drop at high Reynolds numbers.

4.1.2 Proposal 2

Recently, Rachih et al. (2020) suggested that the drag coefficient of a drop, C_d^d, spans between the limits of a rigid sphere, C_d^s, and a gas bubble, C_d^b. They used the hypothesis of Hadamard & Rybczynski and suggested that the highest drag coefficient of a three-dimensional body corresponds to a rigid sphere with the same Reynolds, i.e., where no internal fluid circulation occurs and the non-slip condition is met. Moreover, the lower limit of the drag coefficient corresponds to a spherical fluid particle with negligible viscosity, i.e., a spherical gas bubble with same Reynolds.

Thus, for a specific Reynolds number, the magnitude of C_d^d depends on the viscosity ratio according to Figure 4-2. It follows that:

$$C_d^d = \frac{C_d^b + \varphi C_d^s}{1 + \varphi} \tag{4-11}$$

where C_d^b can be obtained by considering a clean and spherical bubble and the correlation proposed by Mei et al. (1994):

$$C_d^b = \frac{16}{Re}\left(\frac{16 + 3.315Re^{1/2} + 3Re}{16 + 3.315Re^{1/2} + Re}\right) \tag{4-12}$$

Figure 4-2. Evolution of the drag coefficient for bubbles, droplets and solid particles. Comparison between the correlations by Eqs. 4-12 and 4-5 for bubbles and particles, respectively (solid lines).

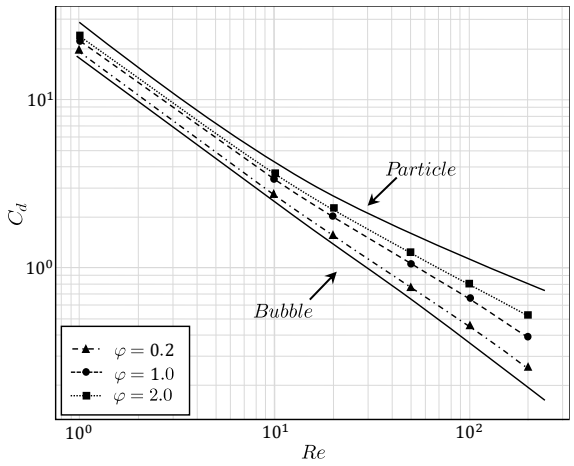

Source: adapted from Rachih et al., 2020.

On extending the hypothesis by Rachih et al. (2020) to the compound drops studied here, an expression for the drag coefficient can be obtained:

$$C_d = \frac{C_d^b + \varphi' C_d^s}{1 + \varphi'} \tag{4-13}$$

where φ' is the same effective viscosity ratio given in Eq. 4-10. Note that Eq. 4-13 is analogous to the approach described earlier; the C_d lies between the upper and lower

limits of a rigid sphere and a spherical bubble, respectively. The effective viscosity of the compound drop is the key parameter to describe its C_d. However, the use of Eq. 4-13 provides an additional term in the estimation of the drag coefficient. By taking the drag of a gas bubble directly into account, the effects of shape deformation and interface contamination of the internal fluid can be accounted for.

4.2 Compound drop orientation

This section focuses on the case of an oscillating compound drop and aims to describe how its orientation (see definition in Figure 3-5) fluctuates in time. The goal is to investigate the effect of the compound nature of the drop on the dynamics of the oscillation.

4.2.1 External phase

Let us consider the idealized case of an oscillating spherical compound drop at high Reynolds numbers according to the scheme shown in Figure 4-3. It is assumed that the external centroid (blue dot) of the compound drop moves periodically with respect to the internal centroid (red dot).

For the sake of simplicity, focus is given now on the oscillation of the external phase assuming that the internal fluid behaves similarly. Thus, θ varies with the distance travelled by the outer centroid, δ, following a sinusoidal behavior with a wavelength λ. This oscillation dynamics will be referred later in this text as the pendular oscillation of the compound drop.

The amplitude of the oscillation plays an essential role in the description of its dynamic behavior. Based on the definition of the orientation angles discussed earlier, the oscillation amplitude is defined as:

$$\Lambda_\theta = 90 - \theta_{max} \qquad 4\text{-}14$$

where θ_{max} is the orientation angle at the inflection points ($\delta = \lambda/4,\ 3\lambda/4\ \ldots$). Note that, according to Figure 3-5, the vertical alignment of the compound drop corresponds to an orientation angle of $\theta = 90$ º.

Figure 4-3. Representative scheme of the pendular motion of an oscillating compound drop. The relative position of the external centroid is shown for different values of time.

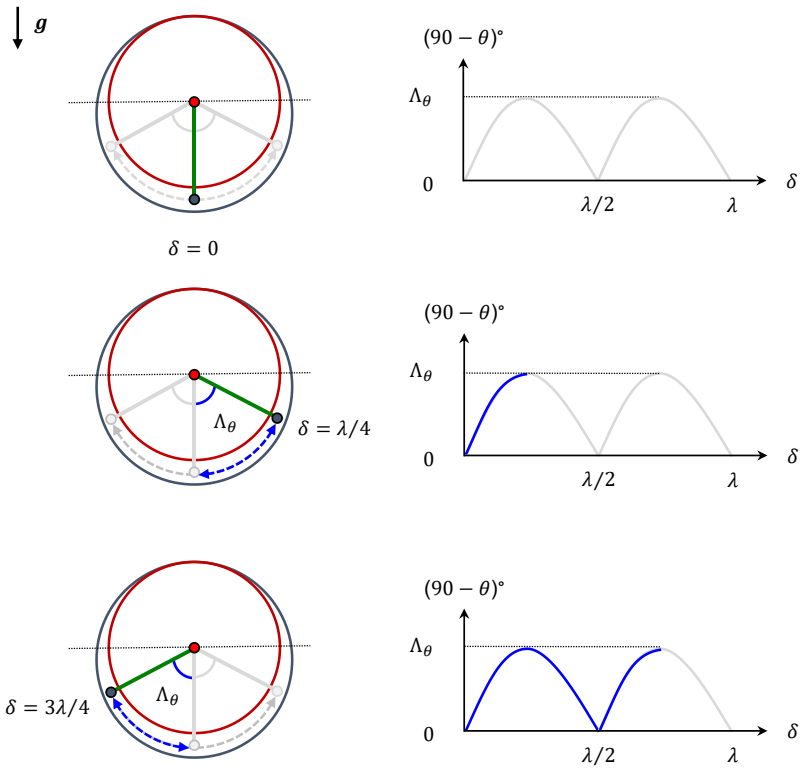

Source: own authorship.

Based on the scheme shown in Figure 4-3, the oscillation starts when $\theta = 90$ º; then, θ increasingly decreases until the inflection points are reached. The first inflection point corresponds to $\delta = \lambda/4$ when the oscillation amplitude, Λ_θ, is reached. Then, θ increases until reaching the vertical alignment once again, restoring its initial position at $\delta = \lambda/2$. Similarly, the orientation of the external phase continues to oscillate towards the opposite side of the compound drop until the oscillation cycle is complete at $\delta = \lambda$. Note that, according to its definition, only the magnitude of θ is considered; thus, $\Lambda_\theta > 0$ regardless the direction of the pendular oscillation. Figure 4-3 clarifies this behavior by showing that the oscillation cycle consists of two peaks, instead of a peak and a valley for a typical sinusoidal cycle.

This oscillation dynamics suggests that the external centroid of the compound drop fluctuates periodically with time. Thus, the typical sinusoidal equation seems to be suitable to describe the behavior of θ as follows:

$$\theta(t) = \Lambda_\theta cos\left(2\pi f_p t\right) \tag{4-15}$$

where f_p is the pendular oscillation frequency. Note that the term 2π is required because the original definition of the sinusoidal equation is based on the angular frequency of the oscillation.

Despite its applicability to the oscillating compound drops herein analyzed, it should be emphasized that the terms in Eq. 4-15 are dimensional. From a fluid mechanical standpoint, it is convenient to describe the pendular motion of the compound drops as a function of dimensionless parameters. By doing so, it is possible to account for some effects of the motion, as will be shown later.

With this aim, it is possible to define the Strouhal number of the pendular oscillation, St_p, as:

$$St_p = \frac{f_p d_{cd}}{V_{cd}} \tag{4-16}$$

that corresponds to the pendular oscillation frequency made dimensionless by the equivalent diameter and the terminal velocity of the compound drop. The Strouhal number is a key parameter to describe the oscillation dynamics and is usually associated with the mechanism of the oscillation.

The insertion of Eq. 4-16 into Eq. 4-15 results in:

$$\theta(t) = \Lambda_\theta cos\left(2\pi \frac{St_p V_{cd}}{d_{cd}} t\right) \tag{4-17}$$

where the temporal term remains in dimensional units. If the dimensionless time is defined as $t\sqrt{2g/d_{cd}}$, Eq. 4-17 becomes:

$$\theta(t) = \Lambda_\theta cos\left(2\pi \frac{St_p V_{cd}}{d_{cd}} \frac{t\sqrt{2g/d_{cd}}}{\sqrt{2g/d_{cd}}}\right) \quad 4\text{-}18$$

As can be seen in Eq. 4-18, it is still difficult to attribute a physical meaning to each term. However, some of the terms may be reorganized to improve their clarity. If the pendular oscillation arises from a balance between the inertia of the flow and gravitational effects the following dimensionless number can be considered:

$$Fr^* = \frac{2\pi V_{cd}}{\sqrt{2gd_{cd}}} \quad 4\text{-}19$$

which is defined as the modified Froude number of the pendular oscillation. It accounts for the relation between the inertia of the flow and the external gravitational field. In typical flow situations, the limit of high Froude number is associated to a significant perturbation in the external field; this parameter can be useful in modeling the pendular oscillation of the compound drop. Finally, Eq. 4-15 becomes:

$$\theta^*(t) = abs\left[cos\left(St_p Fr^* t\sqrt{2g/d_{cd}}\right)\right] \quad 4\text{-}20$$

where $\theta^* = \theta/\Lambda_\theta$ is a normalized orientation angle that goes from zero (vertical alignment) to unity (inflection point). Note that Eq. 4-20 provides only absolute values of θ^*.

4.2.2 Internal phase

A similar procedure may be adopted for the modeling of the sinusoidal behavior of the internal orientation angle ω. For the sake of brevity, such procedure

will not be repeated here. Accordingly, the normalized orientation angle of the internal fluid, $\omega^* = \omega/\Lambda_\omega$, is:

$$\omega^* = abs\left[cos\left(St_p Fr^* t\sqrt{2g/d_{cd}}\right) - \varphi_\omega St_p Fr^*\right] \quad 4\text{-}21$$

However, one should be reminded that the internal fluid is surrounded by the highly viscous external layer. Thus, as a certain period of time is required for the vorticity to diffuse through the external fluid, the internal bubble would then need an extra time to readapt to the new flow conditions (see the inner circulation within the external layer in Figure 4-1). This effect is designated as the temporal lag of the pendular oscillation and is considered in the φ_ω term. Note that the multiplication by $(St_p Fr^*)$ is to maintain the dimensional consistency of Eq. 4-21.

4.3 Final remarks

This chapter proposed mechanistic models to describe the dynamic behavior of compound drops outside the creeping flow regime. The drag coefficient of a compound drop can be estimated from Eqs. 4-9 and 4-13 that are based on the C_d of a rigid sphere and gas bubble with the same Reynolds number such that $C_d = C_d(Re,\ d_b/d_{cd}, \varphi)$. A summary of the aforementioned modeling is presented in Table 4-1. Note that in these models the compound nature of the drop is simplified by assuming a fluid particle with averaged viscosity.

To this date, there is a large gap in the literature regarding the modeling of the drag coefficient of a compound drop. As previously discussed in chapter 2, the behavior of the drag is restricted to simplified scenarios, e.g., where inertia is neglected, concentric configurations are considered, to name just a few. Thus, the modeling herein proposed contributes to filling this gap.

Table 4-1. Governing factors of the drag coefficient of spherical compound drops.

d_b/d_{cd}	< 0.35	
Trajectory	Rectilinear	
Governing effect	Viscosity	
Relevant dimensionless number	Reynolds	
Drag coefficient, C_d	$C_d = C_d^s\left(\frac{2 + 3\varphi'}{3 + 3\varphi'}\right)$	4-9
	$C_d = \frac{C_d^b + \varphi' C_d^s}{1 + \varphi'}$	4-13

Source: own authorship.

The time evolution of the orientation angles of the compound drop, θ and ω, is described by assuming a sinusoidal behavior. A summary of the fitted equations is shown in Table 4-2 for each fluid phase of the compound drop. Note that the parameters St_p and Fr^* rely on experimental data.

Note that in this work a novel oscillation mechanism is suggested for the compound drop, namely the pendular oscillation. Here, the compound nature of the drop is taken into account to describe its oscillatory behavior, where both fluid phases are analyzed separately. To the best of the current knowledge, such detailed description of the motion of compound drops has not yet been presented.

Table 4-2. Fitting of the governing parameters of the oscillatory motion of compound drops.

External phase		Internal phase	
$\theta^* = abs\left[cos\left(St_p Fr^* t\sqrt{2g/d_{cd}}\right)\right]$	4-20	$\omega^* = abs\left[cos\left(St_p Fr^* t\sqrt{2g/d_{cd}}\right) - \varphi_\omega St_p Fr^*\right]$	4-21
		$St_p = \frac{f_p d_{cd}}{V_{cd}}$	4-16
		$Fr^* = \frac{2\pi V_{cd}}{\sqrt{2g d_{cd}}}$	4-19

Source: own authorship.

5 RESULTS – DRAG, SHAPE, AND TRAJECTORY

This chapter analyses the behavior of compound drops rising in quiescent water at high Reynolds numbers. The dynamics of the compound drop is investigated by using the high-speed shadowgraph technique described in chapter 3. The path and rising velocity of the compound drops are investigated in section 5.1. The transition from the rectilinear to the oscillatory rising regimes is briefly investigated in section 5.2. The shape deformation of the compound drops is analyzed in section 5.3, along with the proposal of the governing dimensionless numbers. Finally, section 5.4 analyzes the behavior of the drag coefficient of the compound drops and compares with the modeling proposed in chapter 4.

5.1 Path and rising velocity

The analysis begins with the changes in the trajectory and velocity as the size of the inner bubble progressively increases. Figure 5-1 shows typical image sequences for the rise of an oil drop (a) and compound drops with three values of diameter ratio $d_b/d_{cd} = 0.25$ (b), 0.50 (c) and 0.85 (d).

Figure 5-1. Image sequences of rising drops (a) and compound drops (b - d) for Oil 1 and different diameter ratios. The scale of reference 2 mm is given by the horizontal arrow for each sequence.

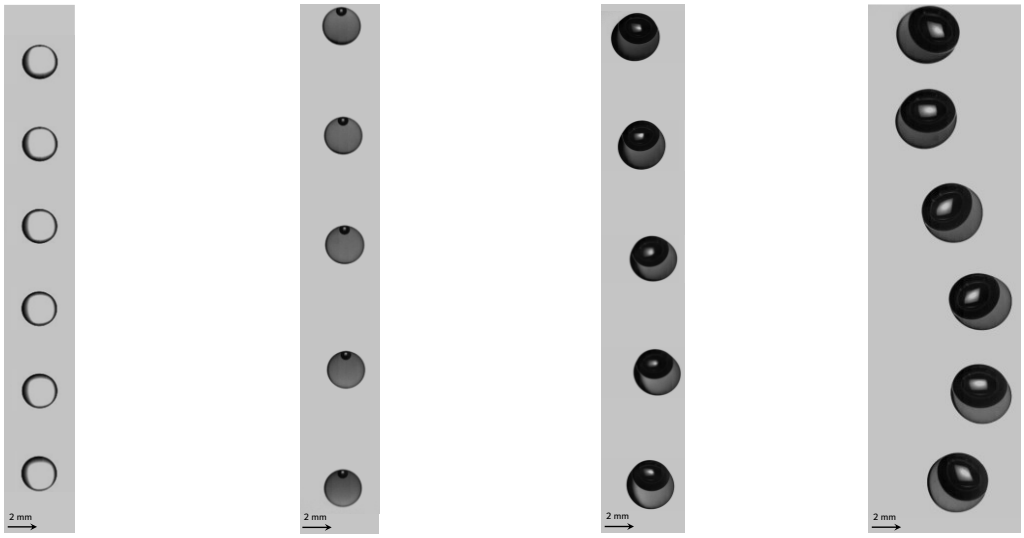

a) $d_d = 2.5\ mm$ b) $d_b/d_{cd} = 0.25$ c) $d_b/d_{cd} = 0.50$ b) $d_b/d_{cd} = 0.85$

Source: own authorship.

The path of the compound drop changes from rectilinear to oscillatory as the size of the inner bubble increases. As shown in Figure 5-1d, the oscillating path is accompanied by a pendular oscillation of the relative position of the gas and the liquid inside the drop. The center of mass of the compound drop is then shifted towards the rear, contributing to the side-ways motion. In addition, the minor axis of the compound drop appears to be aligned with the axis of the drop velocity as observed for rising ellipsoidal bubbles (Ellingsen & Risso, 2001). The trajectories of the compound drops illustrated in Figure 5-1 are also shown in Figure 5-2.

Figure 5-2. Trajectories of single-fluid (a) and compound drops (b - d) from the experiments shown in Figure 5-1. Top row: top-view of the measured trajectories. Bottom row: three-dimensional path.

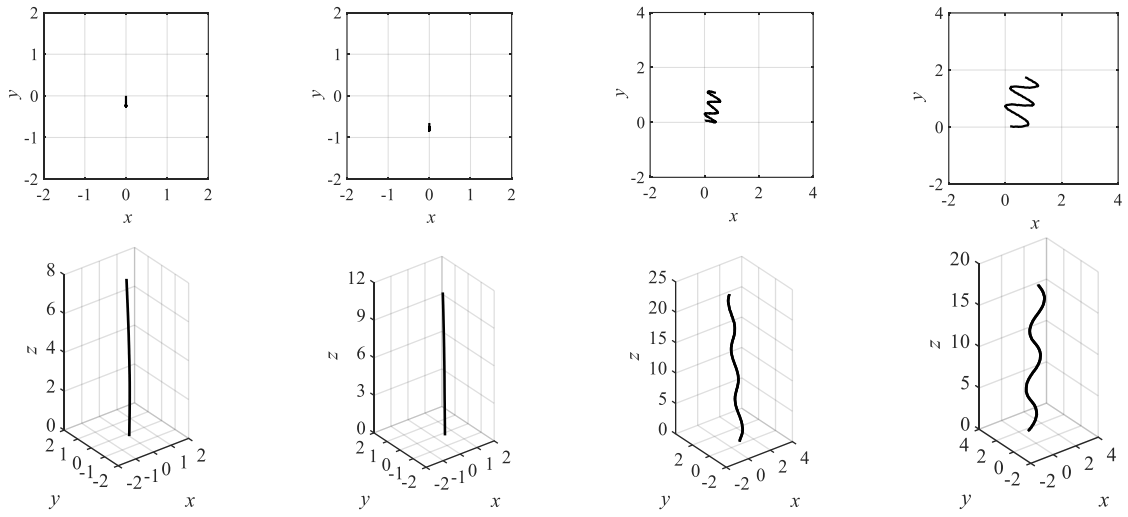

a) $d_d = 2.5\ mm$ b) $d_b/d_{cd} = 0.25$ c) $d_b/d_{cd} = 0.50$ b) $d_b/d_{cd} = 0.85$

Source: own authorship.

The time evolution of the vertical component of the rising velocity of the compound drops, V_z, is shown in Figure 5-3, considering Oil 1. The time was set to zero at the instant of the detachment from the capillary tube. The measurements are shown for three different values of diameter ratio. In all cases, the velocity of the compound drop undergoes a transient state before reaching terminal conditions. For small values of d_b/d_{cd}, the velocity reaches a constant value after the transient period; for $d_b/d_{cd} >$ 0.75 oscillations are observed even after the transient period. For the sake of contrast, the measurements are compared to those obtained for a single oil drop and a single air bubble of approximately the same volume. While the oil droplet exhibits a rectilinear

trajectory with a constant velocity, the air bubble speed oscillates in time. The compound drops velocity measurements lie between these two cases. The same qualitative behavior is observed for the other fluids (Oil 2 and Oil 3 from Table 3-1).

Figure 5-3. Time evolution of the vertical velocity of compound drops (Oil 1) for different diameter ratios. A single-fluid drop (Oil 1) and a single-fluid bubble are shown for comparison (solid lines).

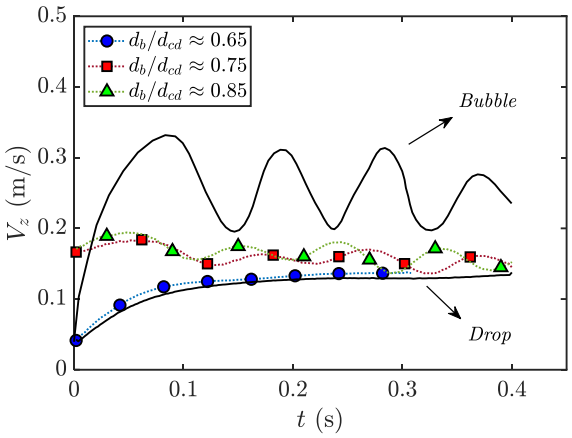

Source: own authorship.

Figure 5-4a reports the terminal velocity of the compound drops as a function of the diameter ratio d_b/d_{cd} for all tests. The list of symbols used in this and subsequent plots is given in Table 5-1. As will be later corroborated by the experiments, the motion will be classified as rectilinear when $d_b/d_{cd} < 0.35$ and as oscillatory when $d_b/d_{cd} > 0.50$. However, details regarding the transition to the oscillatory regime are reserved for later. For now, this range for motion transition ($0.35 < d_b/d_{cd} < 0.50$) remains an approximation for the measurements hereby conducted. Note that different markers are assigned to each regime (see Table 5-1). The terminal velocity increases with the bubble size inside the drop, as a consequence of its increased buoyancy. For comparison, the experimental results of Hayakawa & Shigeta (1974) are also shown in Figure 5-4 for which a similar behavior is noted; however, the comparison is only qualitative because different fluids were used.

The maximum amplitude of oscillation speed Λ_{V_x} is reported in Figure 5-4b, for the cases of oscillatory trajectories, as a function of the diameter ratio. Λ_{V_x}/V_z increases with d_b/d_{cd} reaching values as high as 0.4. Note that the behavior of the terminal velocity is crucial in the estimation of the separation efficiency in gas flotation units.

Figure 5-4. (a) Terminal velocity of the compound drops as a function of the diameter ratio. (×), experiments by Hayakawa & Shigeta (1974). (b) Normalized amplitude of the horizontal component of the velocity. The symbols are shown according to the key given in Table 5-1.

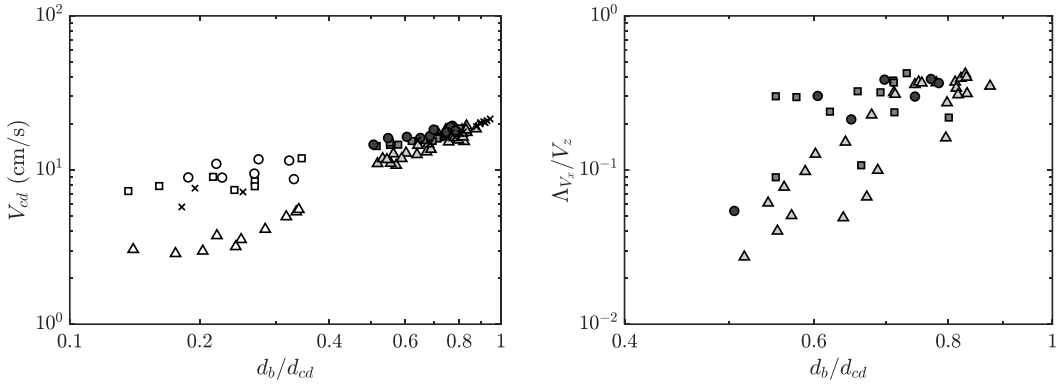

a) b)

Source: own authorship.

Table 5-1. Symbols used in the characterization of the dynamics of the compound drops.

Fluid	Marker	
	Straight path	Oscillating path
Oil 1	△	▲
Oil 2	□	■
Oil 3	○	●

Source: own authorship.

5.2 Motion transition

As a consequence of the fluid inclusion, the effective density of the compound drop (Eq. 3-4) depends on its diameter ratio, as shown in Figure 5-5. Clearly, the dimensionless density is a sole function of the diameter ratio, as indicated by the superposition of the data within the entire d_b/d_{cd} range. For compound drops composed mainly by the oil phase ($d_b/d_{cd} < 0.35$), the presence of the inner bubble has apparently little effect on the density, i.e., $\rho_{cd}/\rho_o \to 1$. Thence, the properties of the compound and single-fluid drops are selfsame. However, for a larger internal bubble ($d_b/d_{cd} > 0.50$), a significant reduction in the density of the compound drop is noted. From that point onwards, the density of the compound drop is affected by the presence of the internal bubble.

Figure 5-5. Dimensionless density of the compound drops as a function of the diameter ratio for all measurements. The symbols are shown according to the key given in Table 5-1.

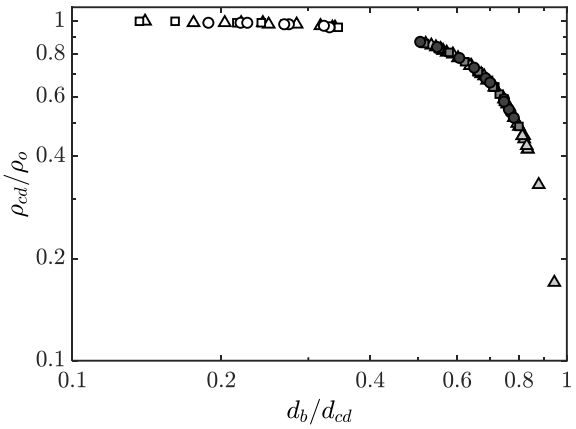

Source: own authorship.

The dynamics is discussed in terms of the inertia that results from the internal bubble. With this aim, Figure 5-6 shows the governing dimensionless numbers as a function of the diameter ratio. Throughout those measurements, the Reynolds number spans between 70 and 750, as shown in Figure 5-6a. For the rectilinear regime, a nearly constant behavior of *Re* is observed and dependent on the properties of the fluid. Thus, it follows that the compound and single-fluid drop present similar inertial effects prior to the engulfment, with the influence of the internal bubble being negligible when the majority of the compound drop is composed by the oil phase.

Figure 5-6. Reynolds (a) and Weber (b) numbers of the compound drops as a function of the diameter ratio. The symbols are shown according to the key given in Table 5-1.

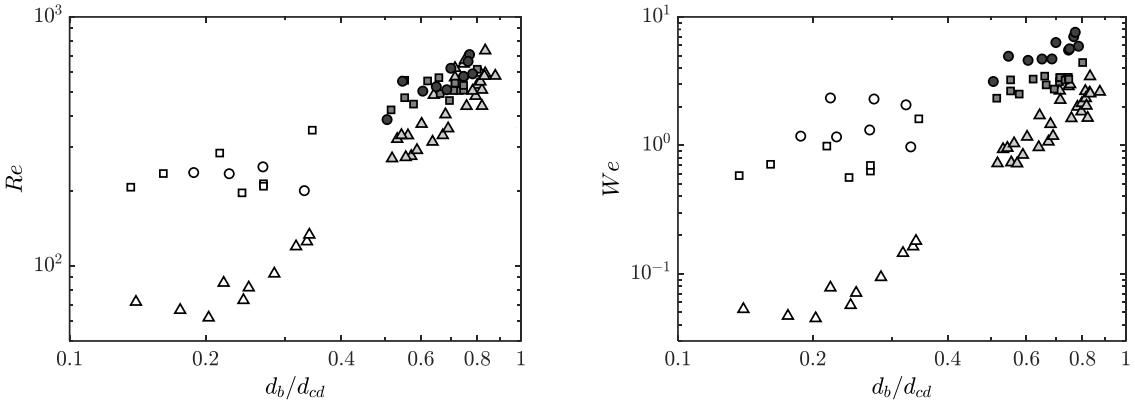

Source: own authorship.

However, the initial properties of the fluids are relevant when determining a critical range of $d_b/d_{cd} \approx 0.50$ that is associated to the increase of inertia. Furthermore, a converging trend is observed in the measurements of Re, suggesting that inertia governs the motion when path instabilities are present, with the diameter ratio being the most relevant dimensionless number when the compound drop is mostly composed by gas.

Figure 5-6b shows that a similar observation can be made when analyzing the Weber number of the compound drops. Thus, the transition may be characterized by either Re or We and a more suitable transition criteria should involve both parameters, as shown in Figure 5-7. To account for the compound nature of the fluid particles analyzed in this work, the Reynolds number is modified by multiplying it by a viscosity ratio defined as $(\mu_o/\mu)^{1/5}$. On doing so, a critical range of the Reynolds number ($Re \times (\mu_o/\mu)^{1/5} \approx 900$) is associated to the motion transition. Note that the modified viscosity ratio herein proposed provides no further physical insight, but acts towards the unification of the transition threshold, regardless of the fluids composing the compound drop.

Figure 5-7. Motion regimes of compound drops in gravitational motion in a viscous fluid. The symbols are shown according to the key given in Table 5-1.

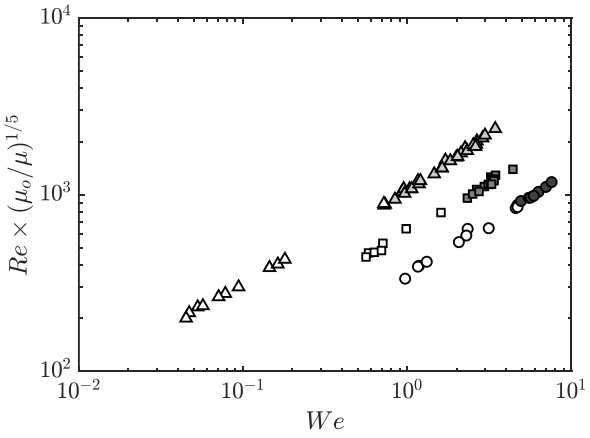

Source: own authorship.

From Figure 5-3, the path oscillation frequency can be determined to be roughly 6 Hz (considering a double period). The normalized oscillating frequency, the Strouhal number, is defined as:

$$St = \frac{f d_{cd}}{V_{cd}} \qquad 5\text{-}1$$

where f is the frequency of the velocity oscillation. The evolution of St as a function of the compound drop Reynolds number is shown in Figure 5-8. A relatively constant value $St \approx 0.1$ is observed for the range of Reynolds numbers considered here.

Figure 5-8. Strouhal number as a function of the Reynolds number for compound drops for the three oils according to Table 5-1. The (×) and (+) symbols show the measurements for bubbles by (Lindt & de Groot, 1974) and (Riboux et al., 2013), respectively. (∗) shows the measurements for the vortex shedding of single-fluid drops (Albert et al., 2015; Charin et al., 2019). The black dashed line shows the trend of the data for rigid spheres considering the data from Clift et al. (1978) and Sakamoto & Haniu (1990). The solid, dashed and dashed-dotted red lines show the Strouhal number from the frequency obtained from Eq. 5-2 for Oil 1, Oil 2 and Oil 3, respectively. The blue dashed line shows the calculation obtained with Eq. 5-3.

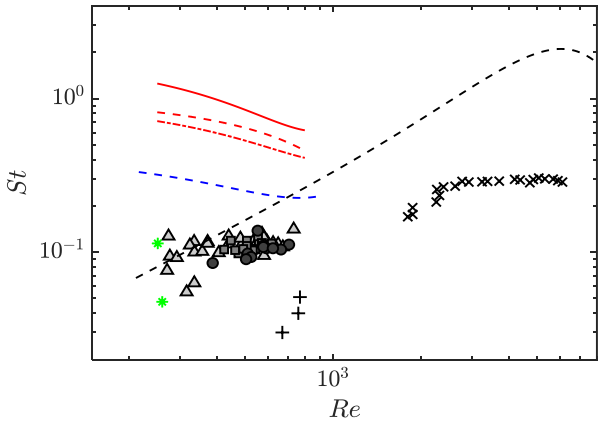

Source: own authorship.

It should be understood what the physical origin of the compound drop oscillations is. For bubbles and solid spheres, the oscillations are known to be the result of the instability of the wake as reported by several studies (Clift et al., 1978). Alternatively, surface oscillations (Lamb, 1932) or the observed pendular-like motion may lead to the appearance of trajectory oscillations.

Path oscillations resulting from the wake instability are firstly considered. To gain some insight, Figure 5-8 also displays the experimental measurements of the Strouhal number obtained for a rigid sphere in a liquid flow (Clift et al., 1978; Sakamoto & Haniu, 1990); additionally, experimental results for bubbles from Lindt &

de Groot (1974) and Riboux et al. (2013) are shown. For solid spheres the oscillations appear at $Re \approx 300$ with a Strouhal number of $St \approx 0.055$; then the value of St increases monotonically until $Re \approx 6000$, beyond which the Strouhal number plateaus. For gas bubbles the Strouhal number shows a similar trend but smaller St values; a plateau around $St \approx 0.3$ is reached for $Re > 2000$.

One would expect the compound drops to behave similarly to a rigid sphere, due to the high viscosity of the external fluid. This seems to be the case since the Strouhal number has the same order of magnitude for $Re \approx 500$. However, the St value for compound drops does not seem to increase significantly with Re, as opposed to what is observed for solid spheres or bubbles. Furthermore, the values of the Strouhal number for compound drops seems to be bound within the limits for bubbles and solid spheres. Figure 5-8 also shows the frequencies of vortex shedding for single-fluid drops rising in water (Albert et al., 2015; Charin et al., 2019).

Now, according to Lamb (1932), the surface oscillation frequency of the second mode of a freely oscillating drop considering an inviscid flow is:

$$f_o = \sqrt{\frac{48\sigma_{o/w}}{\pi^2 d_{cd}^3 (3\rho_{cd} + 2\rho)}} \qquad 5\text{-}2$$

For the three oils and compound drop sizes considered here, f_o ranges from 25 to 30 Hz, which corresponds to a value of St of $O(1)$, which is about one order of magnitude higher than that found for the compound drops, as shown in Figure 5-8. This seems to indicate that shape oscillations could not significantly contribute to the path oscillations for compound drops. Moreover, experiments for drops settling in water (Winnikov & Chao, 1966) corroborate this observation. An approximate value of 0.26 has been reported for a similar range of Re. The reduction in comparison to the prediction by Lamb indicates viscous damping. Nevertheless, the measurements still overestimate the data herein presented.

Lastly, the oscillation frequency of a pendulum, f_p, is considered. From a classical analysis:

$$f_p = \frac{1}{2\pi}\sqrt{\frac{g}{l}} \qquad 5\text{-}3$$

where l is the distance between the center of mass and the top of the drop; hence, $l \approx d_{cd}/2 \approx 1.75$ mm for most of the experiments herein conducted. Considering this length $f_p \approx 12$ Hz for the sizes herein considered. This value corresponds to a $St = 0.2$, as shown in Figure 5-8, which is slightly higher than that measured for the rising compound drops but of the same order. Also, this prediction showed a slight decrease of St with Re, which resembles the experimental trend for compound drops.

Therefore, considering the above arguments it is conjectured that the path oscillations of the compound drops result from the instability of the wake. However, it can also be argued that the pendular motion may not be responsible for the appearance of the oscillatory motion but it most likely affects the droplet trajectory oscillations. It is interesting that the Strouhal number does not increase significantly with Re, so it is possible that the oscillations are affected by the pendular motion. Additional information regarding this subject is discussed in chapter 6 based on the measurements of the velocity field.

5.3 Compound drop deformation

The deformation of an object rising in a quiescent fluid can give an indication of the balance between inertial and surface tension effects. For the case of a compound droplet the presence of a bubble changes the internal pressure balance inside the drop. Also, the path instability of bubbles and drops is known to be strongly influenced by their deformation (Zenit & Magnaudet, 2008).

Figure 5-9a shows the compound drop aspect ratio as a function of the diameter ratio. In these measurements, an averaged value of the aspect ratio of the compound

drop has been considered. Note that the plot is presented in terms of $\chi_{cd} - 1$, to accentuate the value of the deformation. In all cases, the deformation is rather small, increasing slightly for compound drops in the oscillatory regime, but still with values of χ_{cd} below 1.1. Surface contamination probably plays a role in determining the droplet shape, as the experiments were conducted under ordinary laboratory conditions (Duineveld, 1995; Wu & Gharib, 2002); however, this effect was not quantified in this study.

Figure 5-9b shows the value of the aspect ratio of the internal bubble as a function of the diameter ratio. Since both plots (Figure 5-9a and b) are presented using the same scale, a direct comparison is possible: the compound drop is much less deformed than the internal bubble. While the compound drop remains nearly spherical, the internal bubble deforms significantly. It should be noticed that the internal bubble deformation is significant in both rectilinear and oscillatory regimes. Additionally, the deformation of the internal bubble is larger than that of an isolated bubble with similar size: gas bubbles with $d_b < 1$ mm - which in the measurements herein presented correspond to $d_b/d_{cd} \approx 0.25$ - have been reported to be close to spherical (Legendre et al., 2012).

Figure 5-9. Aspect ratio of compound drops (a) and internal bubbles (b) as a function of the diameter ratio. The symbols are shown according to the key given in Table 5-1.

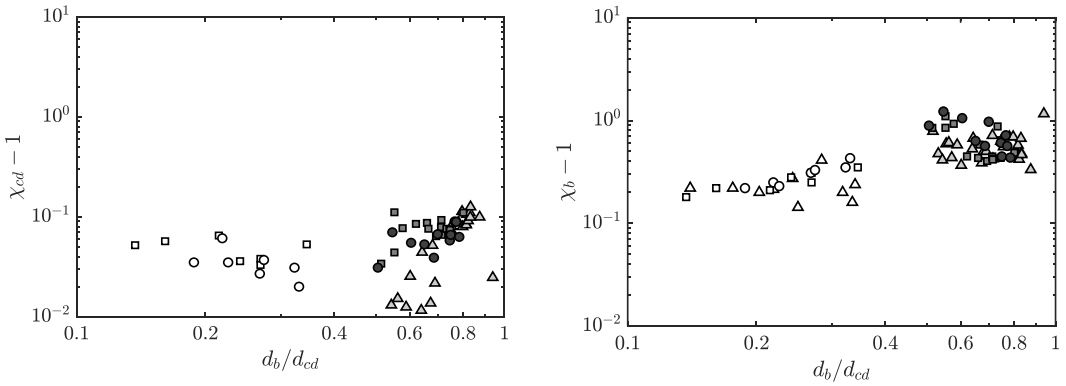

(a) (b)

Source: own authorship.

Considering the shape of the internal bubble, its measured value can be analyzed as a function of the Weber number (Legendre et al., 2012; Moore, 1965). Here an internal Weber number, $We_{o/g}$, is defined by using the properties of oil (since it surrounds the bubble):

- Oil density ρ_o (the external fluid of the compound drop);
- Interfacial tension at the internal interface (oil-gas interface) $\sigma_{o/g}$;
- Terminal velocity of the compound drop V_{cd}.

Hence, the internal Weber number is written as:

$$We_{o/g} = \frac{\rho_o V_{cd}^2 d_b}{\sigma_{o/g}} \qquad 5\text{-}4$$

Figure 5-10a shows the internal bubble aspect ratio χ_b as a function of $We_{o/g}$. The plot also shows the following predictions from Moore (1965):

$$\chi_b = 1 + 9/64 We_{o/g} \qquad 5\text{-}5$$

and Legendre et al. (2012):

$$\chi_b = (1 - 9/64 We_{o/g})^{-1} \qquad 5\text{-}6$$

as the dotted and dashed lines, respectively. Despite the data dispersion, it is clear that the deformation of the internal bubble is different from the predictions, which are valued for isolated single-fluid bubbles at high Reynolds numbers (Legendre et al., 2012; Moore, 1965). A possible explanation is the non-uniform distribution of pressure inside the compound drop, due to its multiphase structure.

In the case of a compound drop, the deformation of the internal bubble is affected by the gas-oil and oil-water interfaces. Since the bubble is immersed inside the oil drop, the inertia of the external flow is not directly balanced by the air-water

interfacial tension, as in the case of bubbles; therefore, the deformation can no longer be predicted by the classical approach (Moore, 1965).

If the inertia of the external fluid does not directly control the deformation, the Bond number can be considered. For instance, Aoyama et al. (2016) proposes:

$$\chi_b = \left(1 + 0.016 Bo_{o/g}^{1.12} Re\right)^{0.388} \qquad 5\text{-}7$$

for an ellipsoidal bubble. Note that Eq. 5-7 was adapted to the system studied here by taking an internal Bond number $Bo_{o/g}$ into account. The definition of the internal Bond number of the compound drop is analogous to Eq. 5-4:

$$Bo_{o/g} = \frac{\rho_o g d_b^2}{\sigma_{o/g}} \qquad 5\text{-}8$$

Figure 5-10. Aspect ratio of the internal bubble as a function of the internal Weber number (Eq. 5-4) (a) and as a function of the internal Bond number (Eq. 5-8) (b). Dashed and dotted lines (a) indicate the predictions by Eq. 5-6 (Legendre et al., 2012) and Eq. 5-5 (Moore, 1965), respectively. The solid line (b) shows the trend of the measurements according to Eq. 5-7 (Aoyama et al., 2016). The symbols are shown according to the key given in Table 5-1.

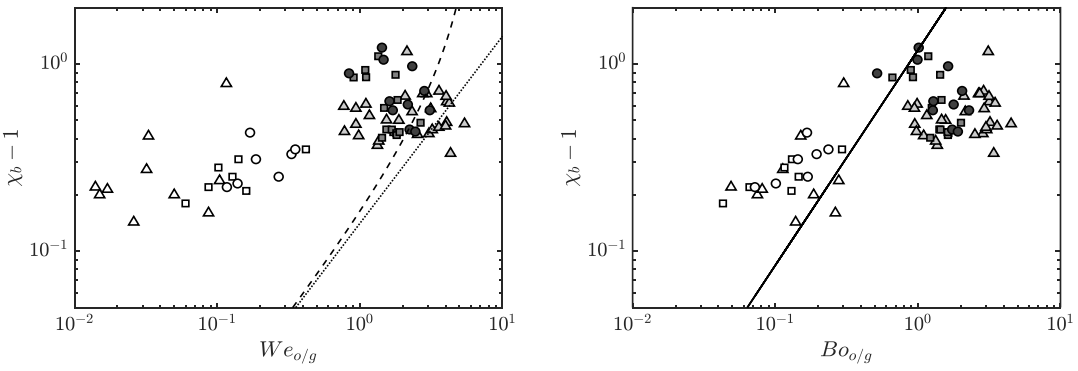

Source: own authorship.

In Figure 5-10b, χ_b is reported as a function of $Bo_{o/g}$. Although both data and prediction from Aoyama et al. (2016) appear closer and both show an increasing

deformation with the internal Bond number, their slopes are different. In the experiments conducted in the present study, both $We_{o/g}$ and $Bo_{o/g}$ are of the same order of magnitude. Therefore, it not possible to completely separate the deformation mechanism between inertia and gravity. An empirical correlation can be proposed to describe the deformation of the internal bubble:

$$\chi_b = 1 + \alpha Bo_{o/g}^{0.2} + \gamma We_{o/g}^{0.25} \qquad 5\text{-}9$$

where the constants α and γ are 0.142 and 0.254, respectively, thus fitting the measurements herein presented (30 % accuracy). This expression does not provide further physical insight, but it is useful in determining the shape of the inner bubble which is needed to understand the surface energy balance within the compound drop.

5.4 Drag coefficient of a compound drop

The drag coefficient is shown in Figure 5-11 as a function of the compound drop Reynolds number Re for all the experiments. As expected, the drag coefficient decreases with Re until $Re \approx 400$, beyond which a slight increase is observed. Note that the increase in the drag coefficient coincides with the transition to oscillatory behavior. To gain some insight about the origin of the drag force, the measurements are compared with known drag expressions for solid spheres, gas bubbles and drops.

The predictions from Eqs. 4-5, 4-9, 4-12, and 4-13 are shown along with the experimental data in Figure 5-11. All the expressions predict a monotonic decrease of the drag coefficient with Reynolds number. The drag coefficient for solid particles is much higher than that for bubbles. As expected, the drag coefficient for compound droplets is between those for spheres and the ones for bubbles; however, the drag coefficient prediction is close to that for solid particles. This is expected since the oil viscosity is much larger than that of water, leading to a large value of φ' for which, according to Eq. 4-9 and Eq. 4-13, $C_d^d \to C_d^s$. Also note that the effects of surface contamination were not addressed, although are probably present (Chebel et al., 2012).

Figure 5-11. The drag coefficient as a function of the Reynolds number for all the measurements. (×) Experiments by Hayakawa & Shigeta (1974) for compound drops; Dotted (green), dashed (red) and dash-dotted (blue) lines, prediction for compound drops (for Oil 1, 2 and 3, respectively) by Eq. 4-9. Similarly, dotted, dashed, and dash-dotted black lines show the prediction by Eq. 4-13 (for Oil 1, 2, and 3, respectively); solid lines (black), predictions for a solid sphere (Eq. 4-5) and single-fluid bubble (Eq. 4-12).

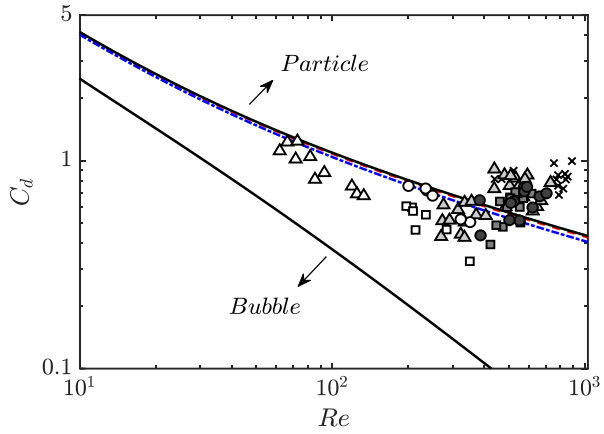

Source: own authorship.

From Figure 5-11 it can be observed that for compound drops with rectilinear paths, C_d decreases with the Reynolds number in agreement with the expressions reported above. The experimental value of C_d is between the prediction for the solid spheres and spherical bubbles, but it is closer to the one for a solid sphere. For droplets with oscillating trajectories the drag coefficient exhibits more dispersion and a slight increase with Re is observed. Such an increase of the drag coefficient is in agreement with the experiments of Hayakawa & Shigeta (1974) for gas-liquid compound drops. A similar behavior is also observed for bubbles when they deform and follow a helicoidal of zig-zagging path (Ellingsen & Risso, 2001).

5.4.1 Rectilinear path

As described above, when the path of the compound drop is rectilinear, the value of C_d is between those for solid spheres and the ones for spherical bubbles. Interestingly, C_d is somewhat smaller than the prediction for a drop with an effective viscosity φ' as defined by Eq. 4-9 and 4-13. Thence, the sole effect of the effective internal viscosity dissipation does not predict the drag coefficient of a compound drop. It must be noted that, because of buoyancy, the internal bubble is not located in the center but rather near the upper edge of the compound drop. Thus, the internal friction

is not uniformly distributed. The reduction of the amount of fluid in the frontal part of the compound drop, where significant shear is expected, may lead to the observed reduction in the drag coefficient.

Figure 5-12. (a) Normalized drag coefficient of the compound drops as a function of the diameter ratio. Solid, dashed and dotted lines, evolution of the normalized drag coefficient for Oil 1, 2 and 3, respectively. (b) Coefficient *P* from Eq. 5-11 as a function of the viscosity ratio. Solid line, fitted correlation (Eq. 5-13). The symbols are shown according to the key given in Table 5-1.

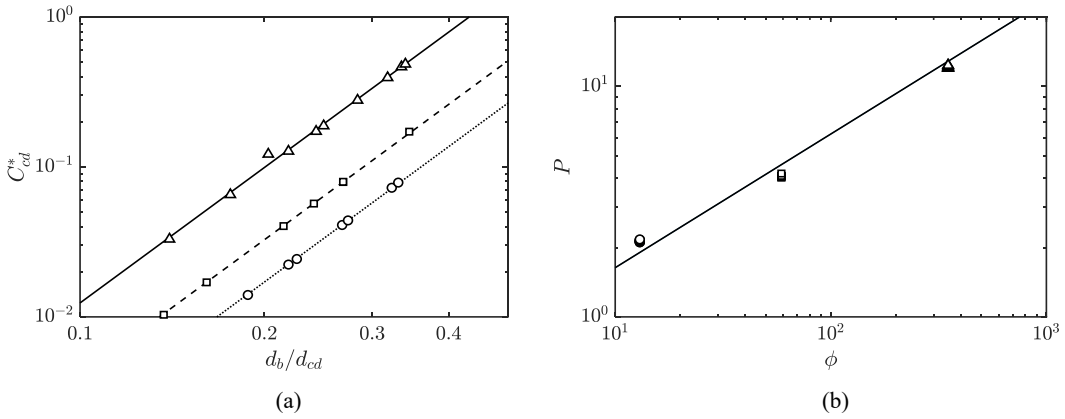

Source: own authorship.

To quantify this effect, a normalized drag coefficient can be defined as:

$$C^*_{cd} = \frac{C^d_d - C_d}{C^d_d} \qquad 5\text{-}10$$

where C^d_d is the experimental drag coefficient of a single-fluid drop of the corresponding oil and same Reynolds number. Thus, C^*_{cd} measures the importance of the internal bubble in the drag coefficient.

Figure 5-12a shows the evolution of C^*_{cd} as a function of the diameter ratio d_b/d_{cd}. Clearly, the reduction in C_d increases with the size of the inner bubble. An inspection of the data reveals that $C^*_{cd} \propto (d_b/d_{cd})^3$, from which it could be proposed:

$$C_d = C_d^d \left[1 - P\left(\frac{d_b}{d_{cd}}\right)^3\right] \quad 5\text{-}11$$

thus yielding:

$$C_{cd}^* = P(d_b/d_{cd})^3 \quad 5\text{-}12$$

where P was found to be dependent on the viscosity ratio φ and can be described by the simple power law relation:

$$P = 0.43\varphi^{0.58} \quad 5\text{-}13$$

as shown in Figure 5-12b. Such evolution accounts for the impact of the internal bubble on the drag reduction and shows that the reduction in the drag coefficient is more pronounced when the viscosity of the oil phase increases.

5.4.2 Oscillatory path

As shown above, when the compound drops oscillate, the evolution of the drag coefficient with Re changes, no longer showing a decrease with Re, as shown in Figure 5-11. As discussed before, the oscillatory behavior arguably results from the instability of the wake but it is enhanced by the drop deformation and thus by the diameter ratio d_b/d_{cd}. Therefore, in Figure 5-13 the drag coefficient of the oscillating compound drops is plotted as a function of the diameter ratio d_b/d_{cd}. As it can be seen, for this regime the value of C_d is directly influenced by d_b/d_{cd} and the effect of the fluid properties does not seem to play a dominant role, as observed for compound drops having a rectilinear path.

The data shown in Figure 5-13 can be described by a simple a power-law relation of the form:

$$C_d = k\left(\frac{d_b}{d_{cd}}\right)^n \qquad 5\text{-}14$$

with $k \approx 1$ and $n \approx 1.2$.

Figure 5-13. The drag coefficient of the compound drops in oscillatory motion as a function of the diameter ratio. The solid line represents the correlation by Eq. 5-14. The symbols are shown according to the key given in Table 5-1.

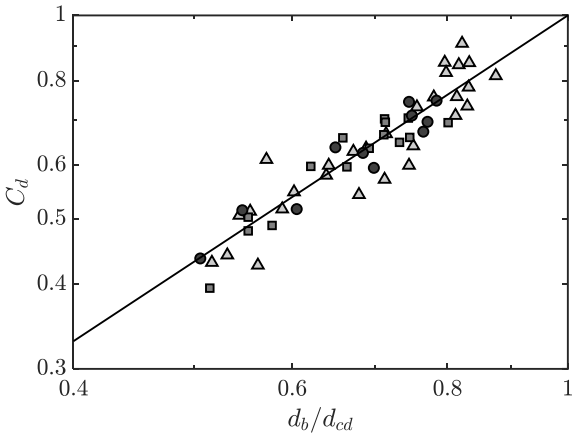

Source: own authorship.

5.5 Final remarks

In this chapter, the general dynamics of compound drops rising in water at high Reynolds numbers was investigated experimentally. The primary focus of this analysis was the investigation of the effect of inertia in the shape, trajectory, terminal velocity, and drag coefficient of the compound drops.

The motion of the compound drops evolved from rectilinear to oscillatory for the three oils tested; the size of the inner bubble determined the transition to oscillatory behavior. By comparing the normalized oscillating frequency, i.e., the Strouhal number, with measurements of spheres and bubbles, it can be concluded that the path oscillations are the result of the wake instability. However, a pendular-like motion of the compound drops was identified; such motion could play an important role in preserving the oscillations.

Despite the role of inertia, a significant deformation of the compound drops was not observed. In fact, the presence of the inner bubble was shown to help retaining a less deformed shape than that expected for a single-phase droplet under equivalent conditions.

The drag coefficient for compound drops was found to be in relatively good agreement with that for solid spheres, for the case when the trajectory is rectilinear. However, the presence of the bubble induced a certain reduction of the drag coefficient. A quantification of this effect was proposed, along with a simplified model. For the case of compound droplets moving with an oscillatory trajectory, the drag coefficient was found to be relatively independent of the value of Re; in this case, the bubble-to-drop diameter ratio appeared to control the drag coefficient, regardless of the type of oil used in each case. The drag coefficient of compound drops lies between those for rigid spheres and those for gas bubbles at high Reynolds numbers. A similar trend has been reported for compound drops in creeping flow. Once the flow became oscillatory, the drag became approximately independent of the value of the Reynolds number.

The results presented in this chapter suggested that further experiments are required to fully understand the dynamics of compound drops rising at high Reynolds numbers. For instance, the pendular-like oscillation of the compound drops apparently presented some additional features when compared to the usual oscillations found for typical bubbles and drops, which were not investigated in this chapter. Moreover, the instability of the wake has been suggested as the onset of the path oscillations. To verify this, the behavior of the continuous fluid has to be analyzed. The aforementioned phenomena are investigated in chapter 6.

6 RESULTS – WAKE AND OSCILLATION DYNAMICS

An analysis of the structure of the wake and oscillation dynamics is henceforth discussed. Section 6.1 investigates the dynamics of the oscillatory motion of the compound drops. Focus is given to its configuration, orientation, and shape fluctuations. Then, the structure of the wake is investigated in section 6.2; an underlying mechanism for the onset of instabilities is proposed. Finally, section 6.3 presents a brief analysis of the structures of the flow in the wake behind a compound drop.

6.1 Oscillatory motion

6.1.1 Compound drop configuration

The discussion of the dynamics of the oscillatory motion begins with an analysis of how the widths H and h (see Figure 3-5) of the external fluid change with the size of the internal bubble. Figure 6-1a shows the width at the bottom segment of the compound drop H as a function of the diameter ratio d_b/d_{cd}. Note that the width is presented as H/d_{cd} to accentuate its proportionality to the size of the compound drop. H/d_{cd} ranges between 0.1 and 0.4 regardless of the external fluid and decreases monotonically according to the correlation:

$$H/d_{cd} = 1 - \frac{d_b}{d_{cd}} \qquad 6\text{-}1$$

that assumes a spherical shape for the fluids. Figure 6-1b shows the measurements of the normalized width h/d_{cd} at the top segment of the compound drop. By showing both plots in the same scale, a direct comparison can be made: the width in the frontal segment of the compound drop is significantly smaller in comparison to the bottom segment; h/d_{cd} ranges from 10^{-5} to 5×10^{-2}. The density difference between the internal and external fluids promotes an internal migration of the inner bubble

towards the top region. Thus, the external fluid behaves as a thin film with increased drainage, showing a decay with d_b/d_{cd} described by:

$$h/d_{cd} = 6.5 \times 10^{-3} \left(\frac{d_b}{d_{cd}}\right)^{-4.5} \qquad 6\text{-}2$$

that agrees well with the experiments when $d_b/d_{cd} < 0.80$; otherwise, a swifter reduction in h/d_{cd} is noted.

Figure 6-1. Normalized width of the external fluid at the bottom (a) and top (b) segments of the compound drop as a function of the diameter ratio. The symbols are presented according to the key shown in Table 5-1. Solid lines represent Eq. 6-1 (a) and Eq. 6-2 (b).

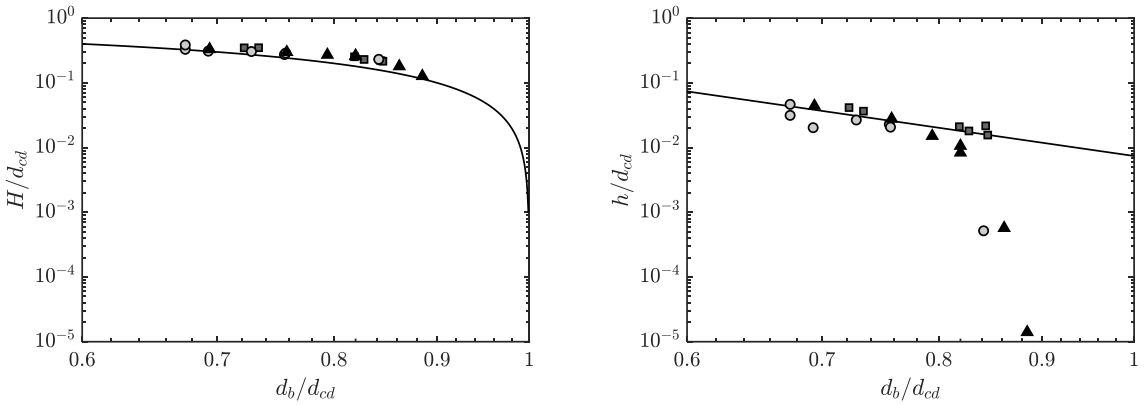

a) b)

Source: own authorship.

The results shown in Figure 6-1 confirm that the compound drops have an eccentric configuration. The centroid of the external fluid is shifted towards the rear of the compound drop, favoring the pendular oscillation presented in chapter 5. Thus, it is expected that this eccentric configuration of the compound drops contributes to this unique oscillatory behavior. It is clear from the images shown above that the size of the inner bubble governs the eccentricity ϵ/d_{cd} (see definition in Figure 3-5), given the evolution shown in Figure 6-2 where the eccentricity evolves as:

$$\epsilon/d_{cd} = 0.44 \left(\frac{d_b}{d_{cd}}\right)^{1.1} \qquad 6\text{-}3$$

Figure 6-2. Eccentricity of the compound drop as a function of the diameter ratio. Solid line represents Eq. 6-3. Filled symbols are shown according to Table 5-1.

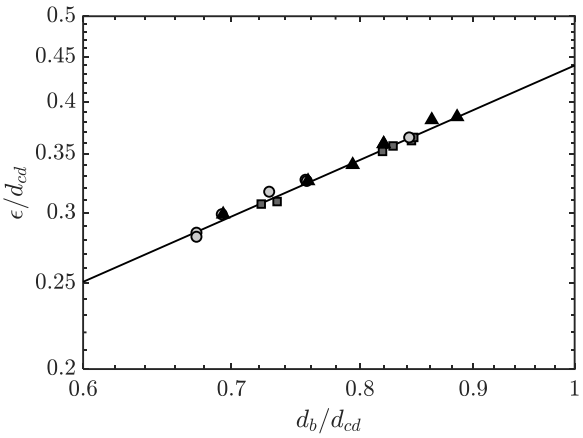

Source: own authorship.

6.1.2 *Compound drop orientation*

According to Figure 3-7, the orientation of both the internal and external phases are also fluctuating. Thus, it is interesting to understand the behavior of the orientation angles θ and ω of the compound drop (defined according to Figure 3-5) and to see whether these parameters may be employed to describe the pendular oscillation. Figure 6-3 shows the time evolution of the instantaneous orientation angles (considering Oil 1) for three representative values of diameter ratios, namely, $d_b/d_{cd} \approx$ 0.70 (a), 0.80 (b), and 0.90 (c).

Figure 6-3. Time evolution of the orientation angles of the external (left) and internal (right) phases of the compound drops (Oil 1) for different values of diameter ratio.

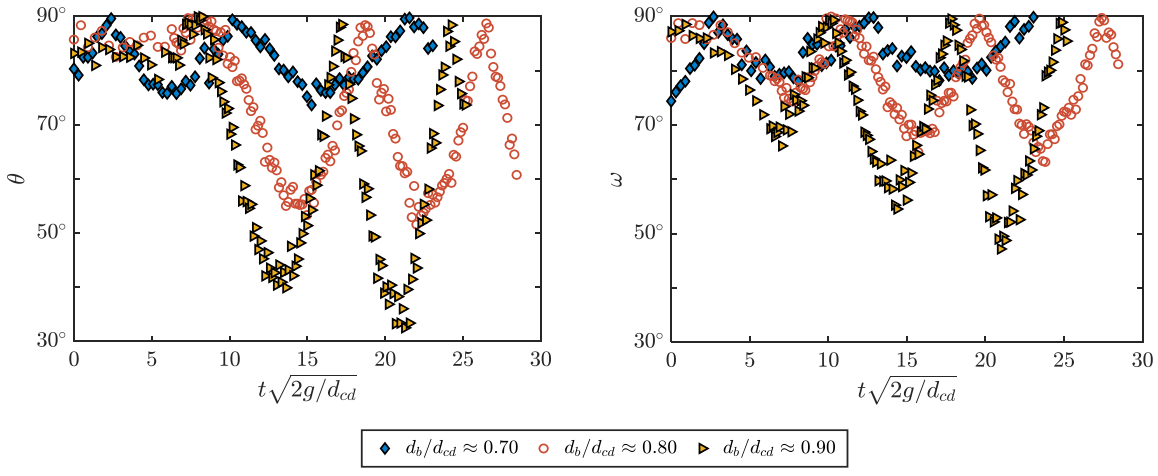

Source: own authorship.

In all cases, θ and ω experience a transient stage before reaching the terminal conditions roughly at $t\sqrt{2g/d_{cd}} = 10$. Then, a sinusoidal behavior that is consistent with the pendular motion suggested earlier is noticed. Note that by definition θ and ω are acute angles and therefore restricted to the first quadrant leading to an abrupt change in direction at 90º, i.e., where the inflection points are reached. Clearly, the external orientation oscillates with higher amplitude than the internal phase. It is conjectured that this is caused by some damping effects promoted by the external interface. To quantify this, a normalized oscillation amplitude is defined as:

$$\Lambda^* = \frac{(\Lambda_\theta - \Lambda_\omega)}{\Lambda_\theta} \qquad 6\text{-}4$$

where Λ_i is the oscillation amplitude. Thus, Λ^* measures the reduction in the oscillation amplitude of the internal bubble and is plotted in Figure 6-4 as a function of the diameter ratio. An inspection of the measurements reveals that Λ^* increases as:

$$\Lambda^* = 0.4(d_b/d_{cd})^3 \qquad 6\text{-}5$$

Figure 6-4. Normalized amplitude as a function of the diameter ratio at terminal conditions. The solid line represents the fitting by Eq. 6-5. Symbols are displayed according to Table 5-1.

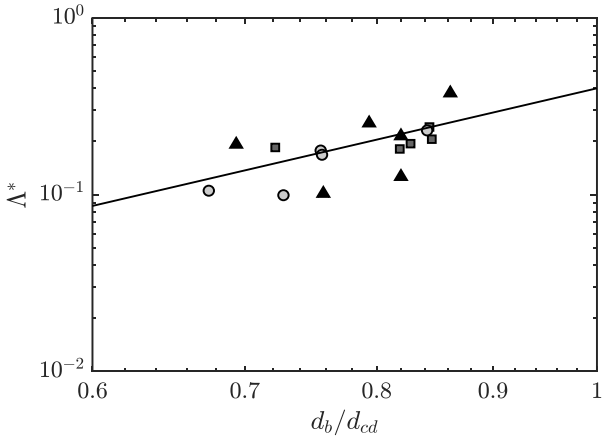

Source: own authorship.

As a certain period of time is required for the vorticity to diffuse within the external layer, a finite time is needed for the internal bubble to readapt to the new

conditions. Thus, a different time response is expected for the internal and external fluids in face of the shear stresses exerted by the flow. To verify this, Figure 6-5 shows the time evolution of θ and ω for the same cases shown in Figure 6-3 after the terminal stage is reached - the time $t\sqrt{2g/d_{cd}}$ has been reset to zero for comprehension purposes. Note that the normalized orientation angles $\theta^* = \theta/\Lambda_\theta$ and $\omega^* = \omega/\Lambda_\omega$ are shown. Thus, θ^* and ω^* span from 0 to 1 and a comparison between the response times of the compound drop can be made.

Figure 6-5. Normalized orientation angles at terminal conditions for different diameter ratios (θ, filled marker; ω, empty marker). Solid and dotted lines refer to Eq. 4-20 and Eq. 4-21, respectively. Blue and red markers represent t_θ and t_ω used in Eq. 6-6, respectively.

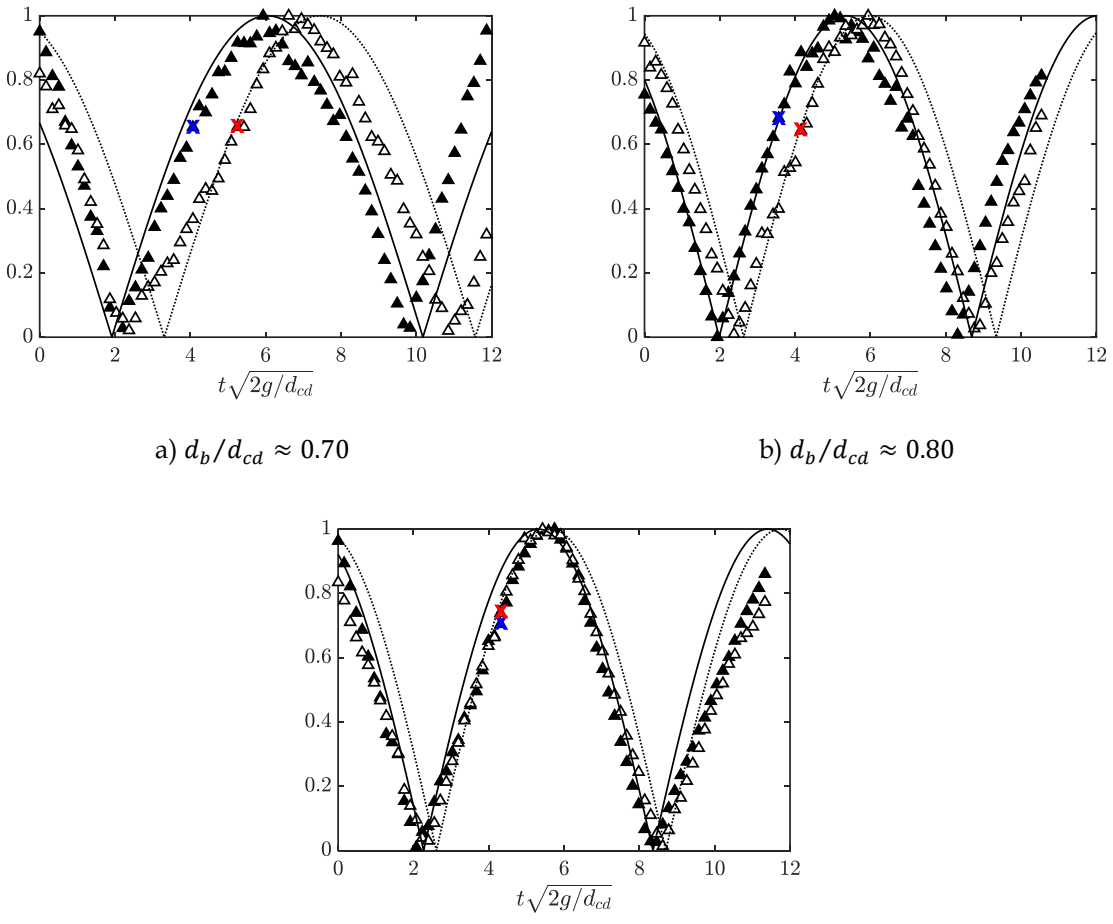

a) $d_b/d_{cd} \approx 0.70$

b) $d_b/d_{cd} \approx 0.80$

c) $d_b/d_{cd} \approx 0.90$

Source: own authorship.

Clearly, the measurements of ω^* are temporally shifted in comparison to θ^*. For the case shown in Figure 6-5a ($d_b/d_{cd} \approx 0.70$) a significant time lag is identified.

Furthermore, the delay decreases with d_b/d_{cd} and is practically non existent for a large internal bubble (Figure 6-5c), where the measurements of θ^* and ω^* superpose. For practical reasons, the delay φ_ω is defined as:

$$\varphi_\omega = t_\omega - t_\theta \qquad 6\text{-}6$$

where t_ω and t_θ are shown in Figure 6-5 as the red and blue dots, respectively. They represent the threshold of the linear behavior of ω^* and θ^* near the inflection point. φ_ω decreases with d_b/d_{cd} for all fluids analyzed, as shown in Figure 6-6a.

Figure 6-6. Modeling of oscillatory motion parameters as a function of the diameter ratio. (a) Temporal delay; (b) Modified Strouhal number. The symbols are shown according to the key given in Table 5-1. The solid lines represent Eq. 6-7 (a) and Eq. 6-8 (b).

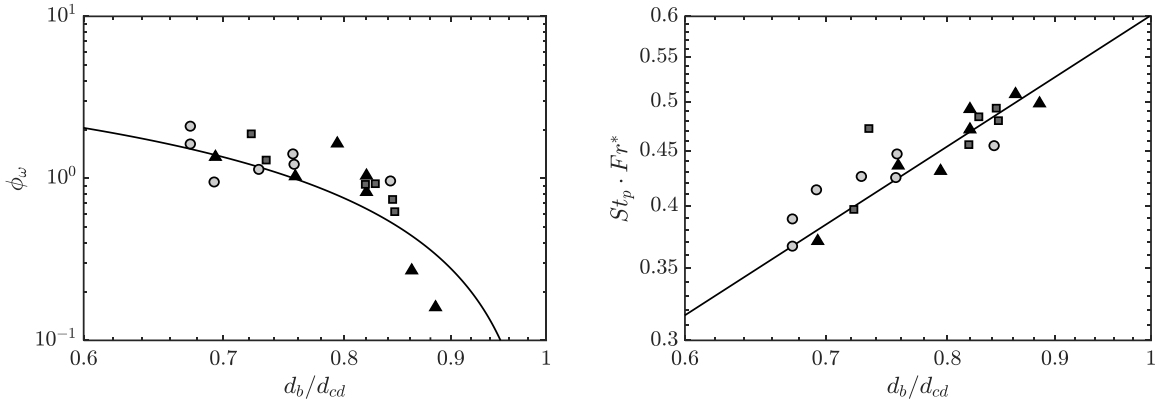

a) b)

Source: own authorship.

Thus, the temporal lag seems to be proportional to the width of the external fluid, where the measurements can be fitted to the expression:

$$\varphi_\omega = 7.5\left(1 - \frac{d_b}{d_{cd}}\right)^{1.4} \qquad 6\text{-}7$$

allowing one to infer that the rate of shear dissipation within the external layer of the compound drops is inversely proportional to H, as expected. Note that the delay term is defined only for the internal bubble.

The frequency of the oscillation is now addressed. Figure 6-5 shows that both phases oscillate with same frequency of about 6 Hz. The frequency of the pendular motion is related to the parameter $St_p Fr^*$, given in Figure 6-6b as a function of the diameter ratio and is described by the simple expression:

$$St_p Fr^* = k\left(\frac{d_b}{d_{cd}}\right)^l \qquad 6\text{-}8$$

where $k = 0.6$ and $l = 1.25$. Thus, Eq. 4-20 and Eq. 4-21 can be used together with the above expression to provide the temporal behavior of θ^* and ω^*, respectively. Figure 6-5 shows that these predictions are in good agreement with the experimental measurements.

6.1.3 *Shape fluctuations*

The transient behavior of the shape deformation of the compound drop can give an insight as to how the pressure difference across the interface is balanced by interfacial tension (Becker et al., 1991). It is also interesting to connect the shape distortion to the pendular oscillation described earlier. For oscillating fluid particles, the shape may experience fluctuations in response to oscillations in the pressure field in the surrounding liquid (Lunde & Perkins, 1998). This is particularly interesting for the compound drops herein studied because of the internal interface that affects the distribution of pressure.

The instantaneous measurements of the aspect ratio of the compound drop χ_{cd} and internal bubble χ_b are shown in Figure 6-7 for Oil 1 at terminal conditions. In all cases, the compound drop and internal bubble experience temporal fluctuations in shape. Sample images of the compound drops are shown at time intervals that correspond to the peaks and valleys of the aspect ratio. Clearly, the shape fluctuations evolve with the diameter ratio. However, d_b/d_{cd} apparently has a different effect with regard to the external and internal phases. The amplitude of the temporal oscillations of χ_b increases with d_b/d_{cd}. χ_{cd}, on the other hand, has higher oscillation amplitudes

when $d_b/d_{cd} \approx 0.80$ (Figure 6-7b) that practically disappear when d_b/d_{cd} reaches 0.90 and the compound drop is nearly spherical. The external fluid behaves as a thin film, damping the deformation of the compound drop.

Figure 6-7. Aspect ratio of the compound drop and internal bubble for different diameter ratios. Sample images are shown for each plot. Filled and empty symbols represent the external and internal fluids, respectively. The blue line is the eccentricity of the compound drop.

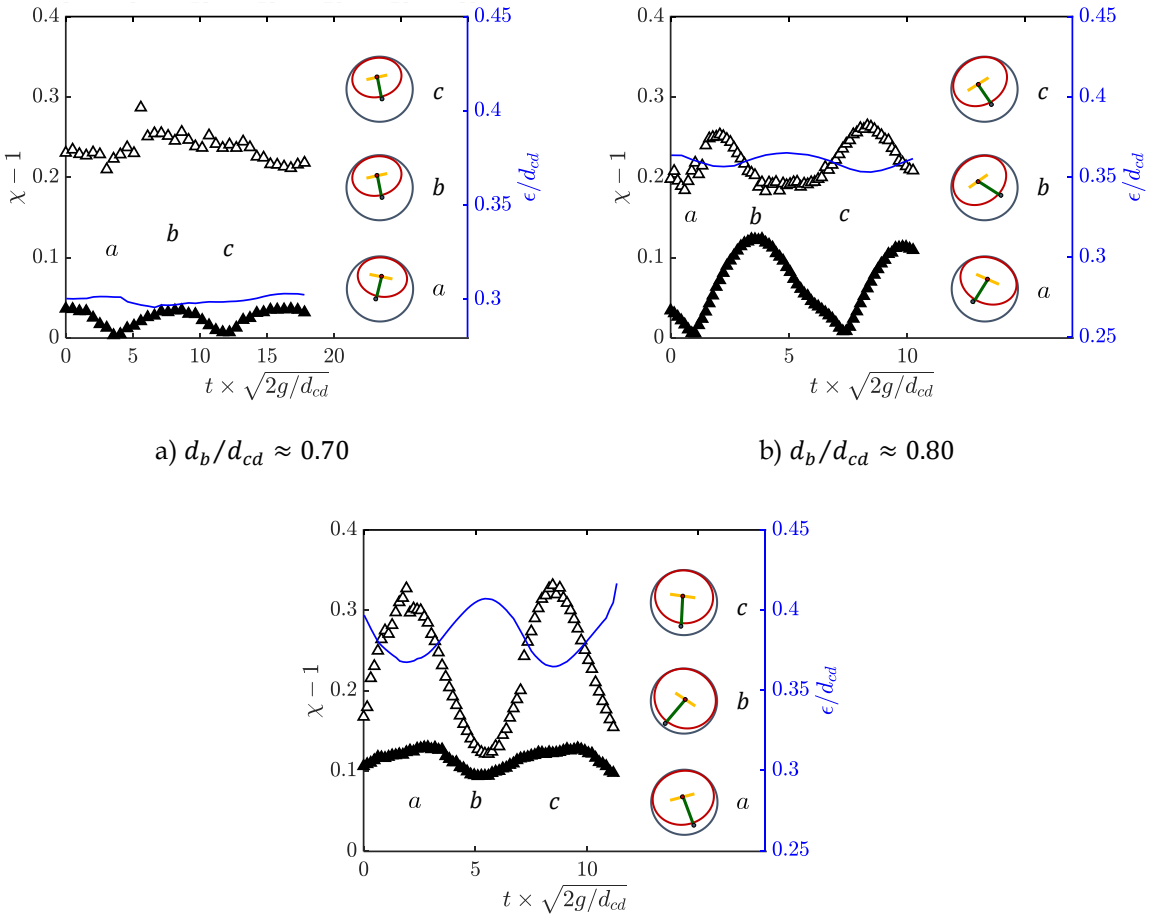

a) $d_b/d_{cd} \approx 0.70$

b) $d_b/d_{cd} \approx 0.80$

c) $d_b/d_{cd} \approx 0.90$

Source: own authorship.

To further illustrate this, Figure 6-7 shows the dimensionless eccentricity ϵ/d_{cd} of the compound drop. A coupling effect between these parameters can be observed. As expected, ϵ/d_{cd} increases with d_b/d_{cd}; however, significant fluctuations are noticed for a large internal bubble (Figure 6-7c) that expresses the damping effect in the amplitude of shape fluctuations. Thus, an uneven oscillation is observed for the compound drops. The shape measurements obtained for the other two fluids (Oil 2 and Oil 3, according to Table 3-1) show a similar temporal behavior.

Figure 6-8 plots the instantaneous measurements of the aspect ratio and orientation angle (in degrees) for the external (left) and internal (right) phases. Note that the scale is the same in the two plots so it is possible to investigate which, if any, of the oscillation mechanisms is prevalent. The governing parameter to address this is clearly the diameter ratio. When $d_b/d_{cd} \approx 0.70$, the measurements of χ_{cd} barely change with θ, which is also observed for the internal bubble. Once the internal bubble grows ($d_b/d_{cd} \approx 0.80$) a larger variation is noticed, but the scaterring of the measurements remains symmetrical, i.e., shape and orientation fluctuations are synchronized; thus, some organization is revealed for these oscillations.

Figure 6-8. Aspect ratio of the compound drop (a) and internal bubble (b) in regard to θ and ω (in degrees) for different values of diameter ratio. Symbols are the same shown in Figure 6-3.

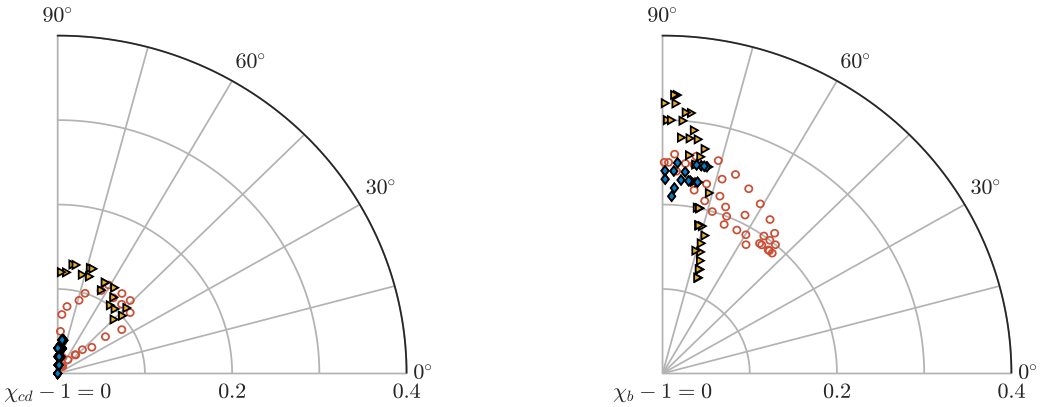

a) b)

Source: own authorship.

When the internal bubble grows further and $d_b/d_{cd} \to 1$ the magnitude of one oscillation mechanism – shape or orientation - seems to increase significantly compared to the other. Furthermore, the governing oscillation mechanism is opposite for each fluid phase. The oscillation of the external phase is governed by θ, whereas the inner bubble experiences significant shape oscillations only.

6.2 Wake structure

From the sample PIV images shown in Figure 3-8 it is possible to characterize the wake behind a compound drop. To do so, the velocity fields in the $x - z$ and $x - y$

planes are obtained by means of the aforementioned cross-correlation technique. Accordingly, the normal and streamwise vorticities are calculated using Eq. 3-5.

6.2.1 Velocity and vorticity fields

The velocity field in the $x-z$ plane and the normal vorticity ω_y are shown in Figure 6-9 for the cases listed in Table 3-3. The vorticity is presented in its dimensionless form as $\omega_y/(V_{cd}/d_{cd})$. The structure of the wake clearly evolves with the diameter ratio d_b/d_{cd}. A mild perturbation is observed in the liquid for Case 1 (shown in Figure 6-9a) where the wake presents an axisymmetric structure. The compound drop essentially drags a portion of the liquid as it flows. Typically, this is consistent with the wake observed in the steady motion of three-dimensional bodies at relatively small Reynolds number, i.e., small rigid spheres (Ghidersa & Dudek, 2000; Tomboulides & Orszag, 2000; Magnaudet & Mougin, 2007), spherical air bubbles in water (Magnaudet & Mougin, 2007; Ellingsen & Risso, 2001; Zenit & Magnaudet, 2009), and liquid drops up to a few millimeters (Albert et al., 2015; Charin et al., 2019). Thus, when d_b/d_{cd} is not too large and Re is below the range of hundreds, the wake of a compound drop is similar to that of a common drop with same Reynolds number, in accordance with previous reports (Brunn & Roden, 1985).

Figure 6-9b shows that unsteadiness appears when vorticity pockets are periodically shed from the wake when $Re > 300$. Although the planar symmetry is preserved - the wake sheds vorticity pockets along a straight line - and positive and negative values of ω_y do not alternate within each vortex thread, clearly suggesting an instability of the wake leading to the appearance of the path instabilities discussed earlier. The wake structure shown in (c) corroborates this observation, since the increase in the path oscillation amplitude develops in conjunction with alternate positive and negative values of the normal vorticity ω_y within each vortex thread. Together with an increase in the vortex shedding frequency, it is clear that the instability of the wake evolves with the Reynolds number Re for higher values of d_b/d_{cd}.

Figure 6-9. Velocity (arrows) and vorticity (contour) fields of compound drops (Oil 1) for cases 1 (a), 2, (b), and 3 (c) as listed in Table 3-3. Measurements near the compound drop are not considered. The black line represents the position of the overall centroid of the compound drop.

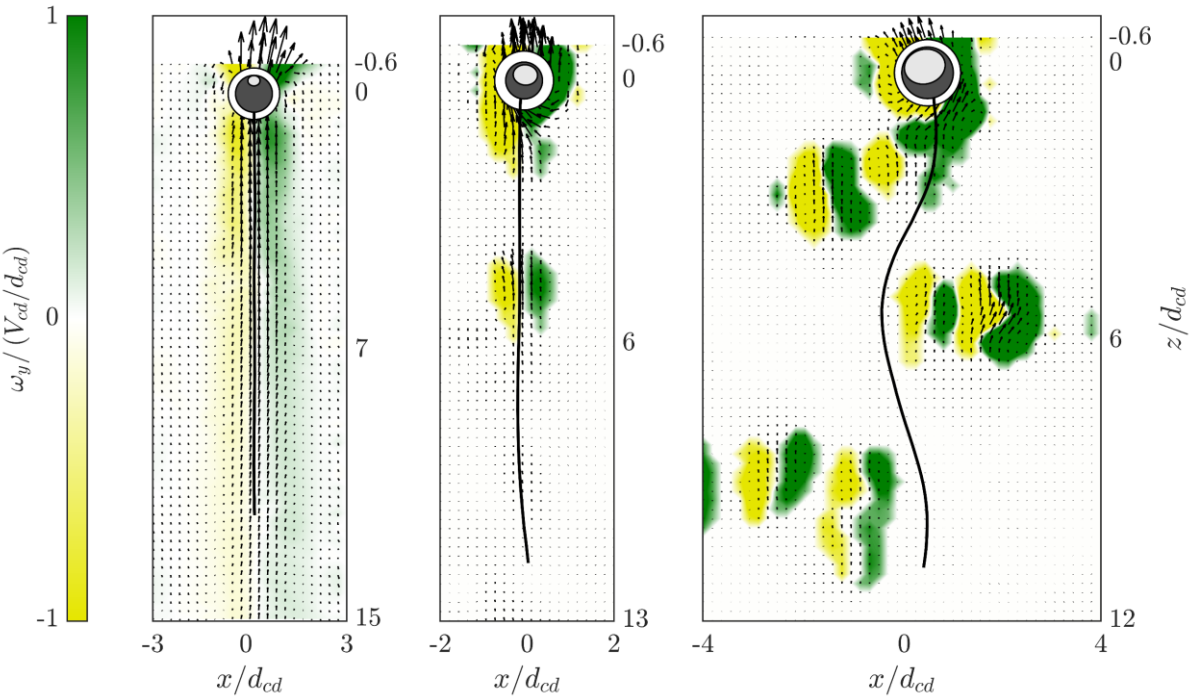

Source: own authorship.

The velocity and vorticity fields shown in Figure 6-9 suggest an uneven distribution of pressure in the liquid surrounding the compound drop that led to the pendular oscillation. To verify this hypothesis, Figure 6-10 shows the streamlines of the flow field around the compound drop for each case. The velocity vectors are also shown to improve the visualization. Focus is given to the segment of the wake that remains attached to the compound drop, at about $z/d_{cd} < 3$. The wake shown in (a) exhibits a symmetry with regard to an $y - z$ plane - also defined as $x = 0$ - that dictates its rectilinear path and straight inclination.

Figure 6-10b (Case 2) shows that the attached eddy is no longer axisymmetric as an uneven liquid perturbation is noted. Apparently, the attached portion of the wake is primarily confined in the right segment and the symmetry axis of the compound drop is now inclined accordingly. A similar behavior is reported for ellipsoidal bubbles in a rocking motion (Lunde & Perkins, 1998; Lindt & de Groot, 1974), where the minor axis forms an angle with the vertical direction that changes

periodically with time (Mougin & Magnaudet, 2001). A parallel can be drawn here, with the remark that the eccentric configuration leads to a relative motion between the centroids that is defined as the pendular motion.

Figure 6-10. Streamlines of the flow past compound drops for cases 1 (a), 2 (b), and 3 (c). The velocity vectors and orientation angles of the compound drop are also displayed.

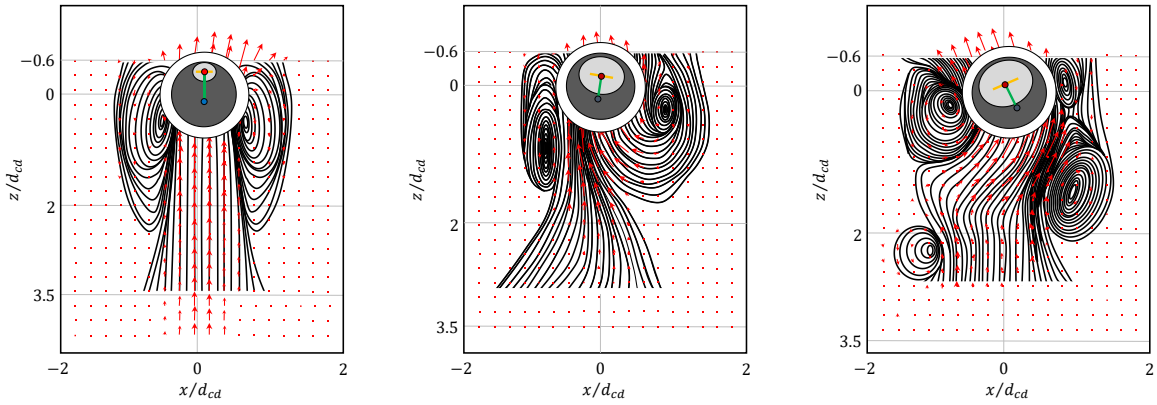

a) b) c)

Source: own authorship.

A subsequent symmetry breakdown is observed in (c) where the vortex pairs are no longer shed simultaneously and the confinement of fluid recirculation is intensified - in that instant, to the left segment of wake ($x/d_{cd} < 0$) -. The compound drop is therefore inclined towards the region with major circulation. Moreover, the periodic nature of the vortex shedding - see the forming eddy at the opposite side ($z/d_{cd} \to 0$) - suggests that this inclination evolves periodically with time, as discussed earlier. The results described present similarities with the correspondent literature for typical drops and bubbles (Yang & Prosperetti, 2007; Albert et al., 2015). The instability of the wake triggers the unsteadiness of the flow (Charin et al., 2019; Zenit & Magnaudet, 2009).

From the images shown in Figure 3-8 is possible to obtain the velocity field in the $x - y$ plane and to calculate the streamwise vorticity from Eq. 3-5. Thus, it can be investigated whether ω_z evolves with the rising regime of the compound drop. Figure 6-11 shows the velocity and vorticity fields for a compound drop in straight motion (Case 1). From the measurements shown for different times after the compound drop

Figure 6-11. Velocity and vorticity fields for Case 1 listed in Table 3-3. The arrows denote the velocity vectors in the $x-y$ plane; the colormap shows different values of streamwise vorticity. The lines show contours of isovorticity: red, $\omega_z/(V_{cd}/d_{cd}) = +0.4$ and blue, $\omega_z/(V_{cd}/d_{cd}) = -0.4$. (a) $t\sqrt{2g/d_{cd}} = 0$, (b) ≈ 4, and (c) ≈ 8.

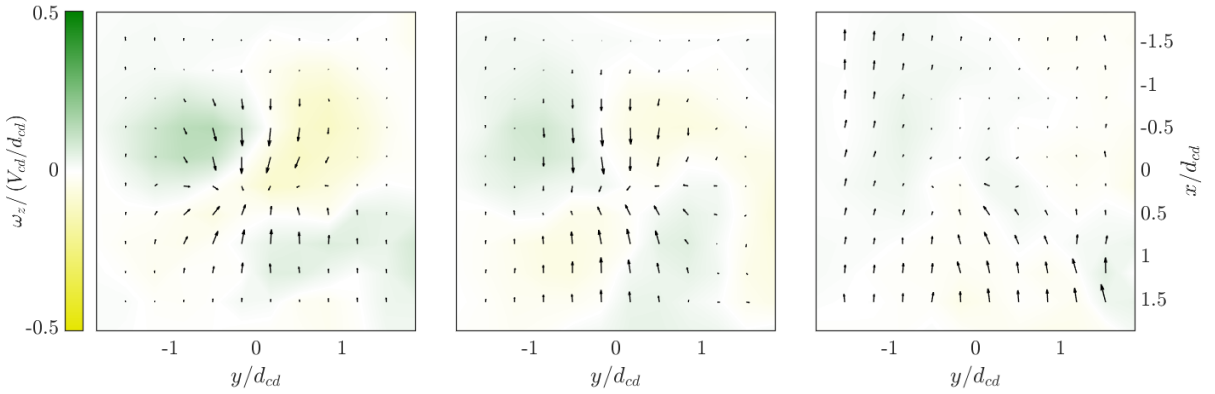

a) b) c)

Source: own authorship.

Figure 6-12. Velocity and vorticity fields for Case 2 listed in Table 3-3. Symbols are the same as in Figure 6-11. (a) $t\sqrt{2g/d_{cd}} \approx 3$, (b) ≈ 5, (c) ≈ 8, (d) ≈ 11, (e) ≈ 14, and (f) ≈ 16.

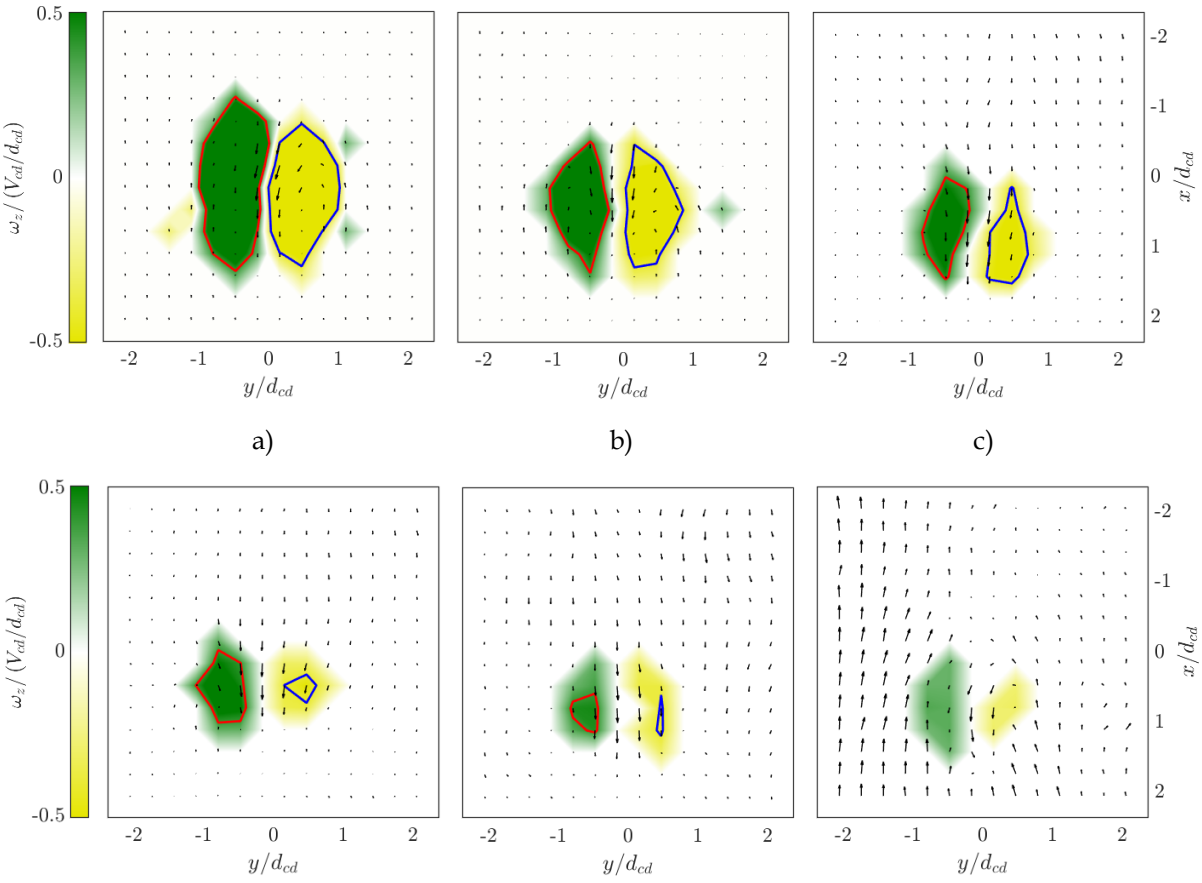

a) b) c)

d) e) f)

Source: own authorship.

crosses the laser sheet, it is clear that no streamwise component of the vorticity is identified; the motion resembles a "sink" flow where a portion of the fluid is dragged by the compound drop, as shown earlier. These measurements of the flow field are similar to those obtained by Zenit & Magnaudet (2009) for a bubble in rectilinear motion.

Figure 6-13. Velocity and vorticity fields for Case 3 listed in Table 3-3. Top (a - c) and bottom (d - f) rows relate to the first and second vortex pair, respectively. Symbols are the same as in Figure 6-11. (a) $t\sqrt{2g/d_{cd}} \approx 3$, (b) ≈ 5, (c) ≈ 8, (d) ≈ 16, (e) ≈ 21, and (f) ≈ 26.

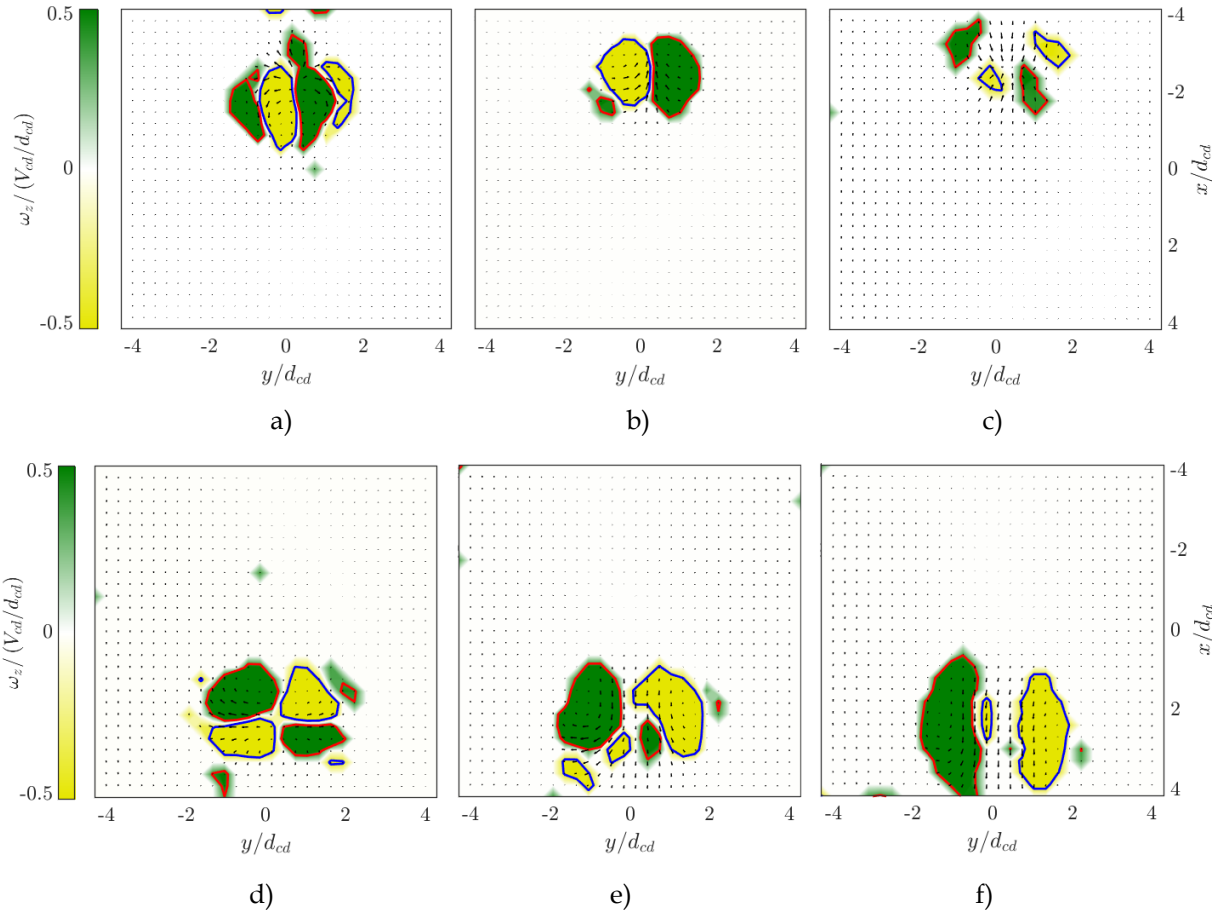

Source: own authorship.

However, for the transition regime (Case 2) shown in Figure 6-12, two discrete pockets of streamwise vorticity ω_z with opposite signs are clearly identified. The structure also evolves with time, where the strength of the swirling regions progressively weakens after the compound drop crosses the plane. For visualization purposes, a threshold limit of $\omega_z/(V_{cd}/d_{cd}) = \pm 0.4$ is shown in Figure 6-12 as the red and blue lines. The area within the threshold curve clearly reduces with time.

Figure 6-13 shows that further instabilities arise for the oscillatory regime (Case 3) of the compound drop. Multiple swirling regions are detected in the wake structure. Furthermore, at $t\sqrt{2g/d_{cd}} \approx 16$ an additional vortex structure is identified at a different position in the $x-y$ plane, corresponding to a secondary vortex pair that sheds from the wake. The positive and negative values of ω_z also appear to be alternate when compared to the first vortex pair, contributing to the instability of the wake.

6.2.2 3-D rendition of the wake structure

From the vorticity fields it is possible to reconstruct the 3-D wake structure of the compound drops. An instructive visualization of the wake is shown in Figure 6-14 for the transitory rising regime. The wake was assembled by converting the threshold values of $\omega_z/(V_{cd}/d_{cd}) = \pm 0.4$ into slices in the z plane by simply estimating the vertical position of the compound drop as $z = V_{cd}t$. Note that this approach does not take the fluctuations in V_{cd} into consideration and is therefore a simplified reconstruction. Furthermore, since the measurements of ω_z are obtained after the compound drop crosses the plane, a Lagrangian vorticity field can be considered only in the vicinity of the compound drop, represented in Figure 6-14 as a sphere.

The wake consists of two vortex tubes of opposite sign that thin out with time as a consequence of viscous dissipation of the streamwise vorticity; the wake of the compound drop extends up to approximately 12 times its diameter. Note that this wake structure is similar to that observed for a zigzagging bubble (Zenit & Magnaudet, 2009), with the remark that the compound drops herein considered remain essentially spherical. Figure 6-15 confirms the evolution of the wake instability for compound drops in the fully-developed oscillatory motion (Case 3). The shedding and lateral migration of vortex pairs contributes to the loss of planar symmetry of the wake when compared to the transition stage of the oscillation. The direction of the discrete swirling regions now alternate in each vortex pair. Therefore, the oscillatory motion of the compound drop is intermittent, given the periodic nature of the vortex shedding. A similar flow structure was numerically investigated by Albert et al. (2015) for common drops rising in water at high Reynolds numbers.

Figure 6-14. Reconstructed isovorticity surfaces: the green and yellow colors show surfaces of iso-streamwise-vorticity with values of $\omega_z/(V_{cd}/d_{cd}) = +0.4$ and $\omega_z/(V_{cd}/d_{cd}) = -0.4$, respectively. (a), (b), and (c) show different views for the same flow (Case 2, from Table 3-3.) A sphere is positioned at (0,0,0) to represent the compound drop.

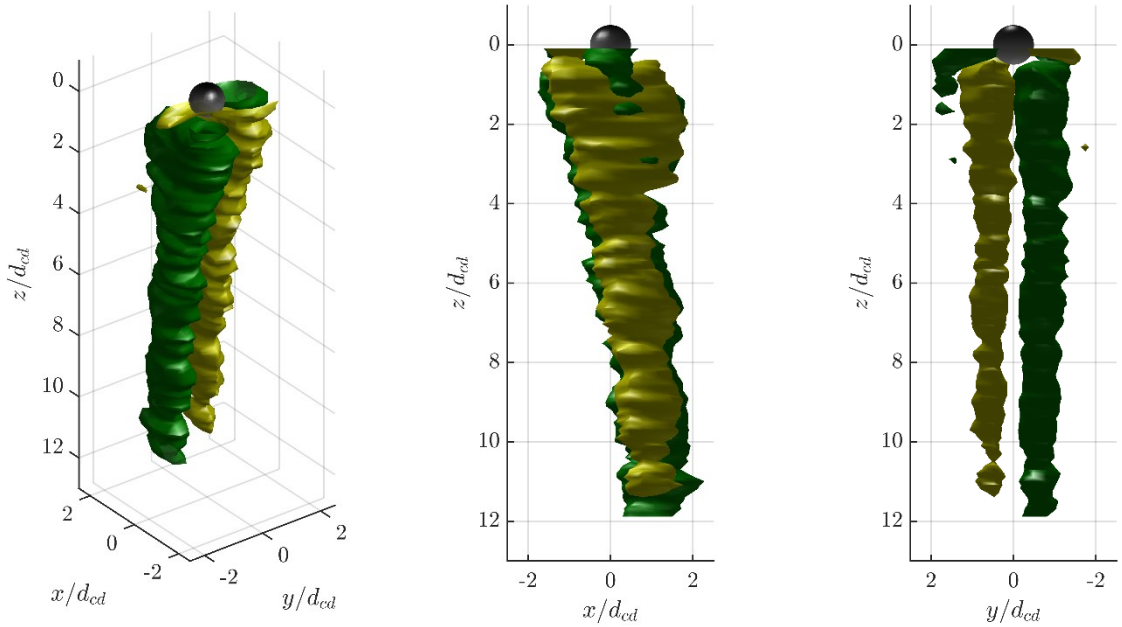

a) b) c)

Source: own authorship.

Figure 6-15. Reconstructed isovorticity surfaces for Case 3, listed in Table 3-3. The symbols are the same as in Figure 6-14.

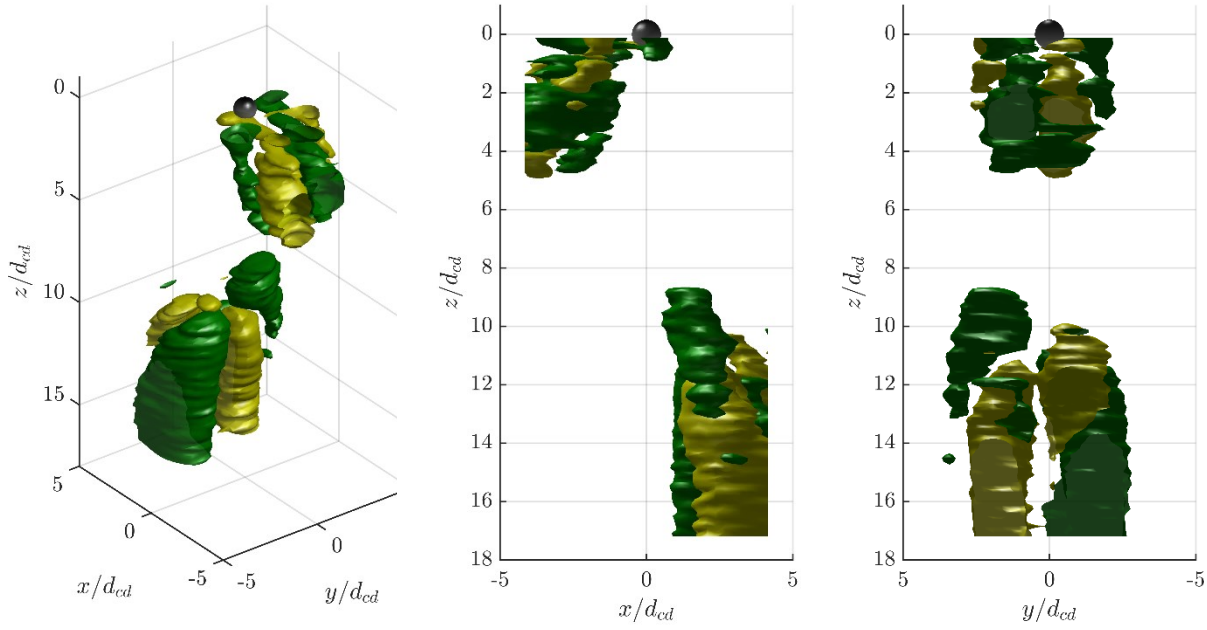

a) b) c)

Source: own authorship.

6.2.3 *Liquid-induced velocity*

So far, the wake of a compound drop appears to be similar to typical particles, e.g., rigid spheres, gas bubbles, and liquid drops. However, it should be noted that the pendular oscillation is absent in such particles because of their single-phase structure. Thus, to investigate the structure of the wake further, the velocity induced in the surrounding liquid by the compound drop is analyzed; possibly, the pendular oscillation affects the way that the compound drop disturbs the continuous liquid.

The longitudinal velocity profile shown in Figure 6-16a provides further insight into how the rising regime of the compound drop affects the liquid perturbation. The vertical component of the velocity, v_z, is measured along the rising paths of the compound drop - black solid line in Figure 6-9 - and shown as a function of the normalized vertical position, z/d_{cd}. The rising regime is crucial in the determination of the longitudinal velocity decay. As one might expect from the velocity fields shown in Figure 6-9, an asymptotic decrease in v_z/V_{cd} is observed for Case 1 suggesting a long wake, surprisingly similar to the one of an ellipsoidal bubble. Aside for the rectilinear case, v_z is actually greater than V_{cd} when $0 < z/d_{cd} < 1$. A similar behavior has been reported for rising bubbles (Ellingsen & Risso, 2001; Roig et al., 2012).

Figure 6-16. (a) Longitudinal velocity along the path of the compound drop (solid lines in Figure 6-9) for the same cases shown in previous plots (△ Case 1, □ Case 2, ◆ Case 3). Dashed, dotted, and solid lines (black color) represent spline fits for cases 1, 2, and 3, respectively. Blue and red lines show the predictions by Ellingsen & Risso, 2001 for an ellipsoidal bubble in an inviscid and viscous flow, respectively. (b) Transverse profiles of v_z for cases 1 (black), 2 (red), and 3 (blue). Solid and dotted lines represent the transverse profiles at $z/d_{cd} = 1$ and $z/d_{cd} = 1.3$, respectively.

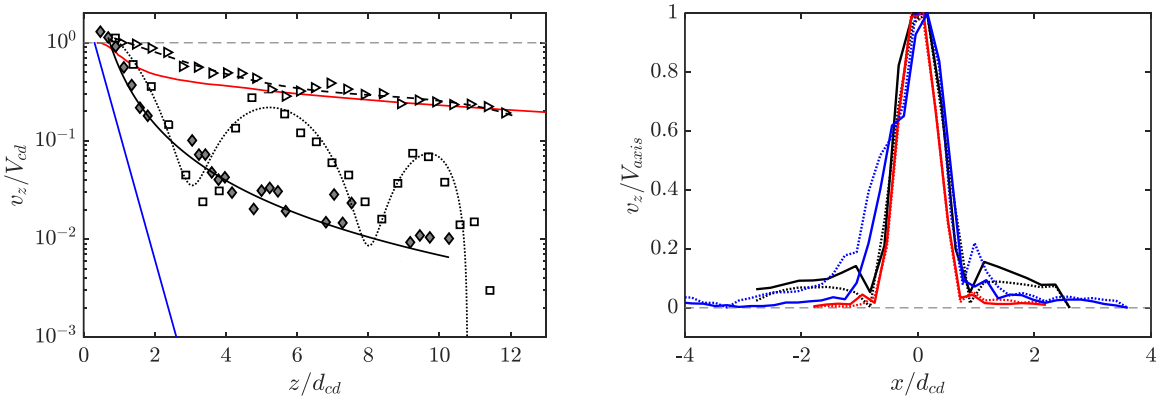

a) b)

Source: own authorship.

A rapid decay is observed for Case 2 when $z/d_{cd} < 4$ followed by two peaks in v_z at $z/d_{cd} \approx 5$ and 9.5 that coincide with the locations of the vertical position of the vortex pairs. For Case 3, a swift decay in v_z/V_{cd} is observed; it arises from the lateral migration of the vortex pairs, now located farther away from the rising path of the compound drop. A direct comparison can also be made with the theory of potential flow (extracted from Ellingsen & Risso (2001) for an ellipsoidal bubble) that predicts a rapid decrease in v_z/V_{cd} due to the absence of a wake. This theory is known to describe well the wake of spherical bubbles at high Reynolds numbers (Biesheuvel & Winjgaarden, 1984). However, this is not valid for the compound drops and the pendular oscillation probably plays some role here.

The transverse profile of the liquid velocity v_z - normalized by $V_{axis} = v_{z_{x=0}}$ - is shown in Figure 6-16b for two positions within the region corresponding to the recirculating wake ($z/d_{cd} = 1$ and 1.3). The horizontal position x/d_{cd} has been normalized to converge to zero at the center of the wake for all cases. The rising regime affects mainly the longitudinal profile since the measurements shown in Figure 6-16b overlap for all cases analyzed. Thus, the dissipation of momentum is restricted to the x direction in which an exponential decay is observed for all cases. From the measurements hereby described, the wake of the compound drops with pendular oscillation appears to be similar to a typical single-fluid bubble, at least in terms of the liquid-induced velocity.

6.2.4 Lift force inferred from the vorticity in the wake

Now, the lift force acting on a compound drop is analyzed; the goal here is to check whether this is the suitable parameter to relate to the pendular oscillation observed for the compound drops. As pointed out by Magnaudet (1997), the asymmetry of the flow makes the determination of the lift force extremely difficult and only a rough quantitative estimation can be obtained experimentally. However, it is possible from the measurements to obtain the lift force $\boldsymbol{F}_L$ from the simplified model proposed by de Vries et al. (2002) that estimates the lift force exerted in an oscillating bubble by two inviscid vortices as:

$$\boldsymbol{F_L} = \rho \tau l_c \boldsymbol{V_{cd}} \qquad 6\text{-}9$$

where l_c is the distance between the vortex centers and τ is the circulation of each vortex. Both parameters can be obtained directly form Figure 6-12 and Figure 6-13. The streamwise component of the vorticity is diffused throughout the swirling region limited by $\omega_z/(V_{cd}/d_{cd}) = \pm 0.4$. Therefore, the circulation of each vortex is obtained from the surface integral within the aforementioned threshold limiting curve:

$$\tau = \int \vec{\boldsymbol{v}} \cdot d\vec{\boldsymbol{r}} = \int_S \omega_z dS \qquad 6\text{-}10$$

Thus, the fluid circulation changes with time given that the cross-sectional area of the vortical structure diminishes due to viscous dissipation. The temporal evolution of τ is shown in Figure 6-17.

Figure 6-17. Dimensionless circulation of the streamwise vortices calculated according to Eq. 6-10. (□) and (○) show the measurements for cases 2 and 3, respectively. Filled and empty symbols correspond to the positive and negative vortices, respectively.

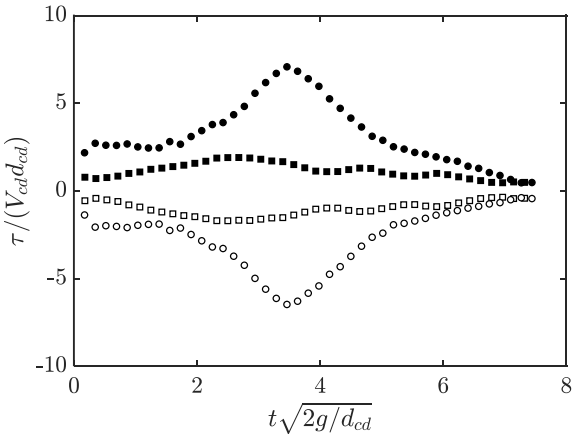

Source: own authorship.

Note that the fluid circulation is made dimensionless against $(V_{cd}d_{cd})$. The circulation depends greatly on the rising regime. For the transitory regime (Case 2), the absolute value of $\tau/(V_{cd}d_{cd})$ reaches a maximum of roughly 2 at $t\sqrt{2g/d_{cd}} \approx 3$, followed by a smooth decaying trend. As for the oscillatory regime (Case 3), a peak in

the measurements is clearly identified at $t\sqrt{2g/d_{cd}} \approx 3.8$ for which $\tau/(V_{cd}d_{cd}) \approx 7$. As expected, the circulation increases substantially for the oscillatory regime. Zenit & Magnaudet (2009) and de Vries et al. (2002) obtained a similar temporal evolution of $\tau/(V_{cd}/d_{cd})$ for zigzagging bubbles. For the compound drops studied here, the measurements correspond to a value of τ of $O(0)$ - same order of magnitude - for the transitory case, and $O(1)$ - one order of magnitude higher - compared to the measurements by Zenit & Magnaudet (2009) and de Vries et al. (2002), respectively.

Finally, the lift force can be calculated from Eq. 6-9 using the measurements shown above. Note that for the vortical structures presented here, $l_c/d_{cd} \approx 1$ and ≈ 2 for cases 2 and 3, respectively, that apparently varied randomly with time. However, the strength of the fluid circulation varies significantly for different time instants during the flow; therefore, the estimated values of $\boldsymbol{F_L}$ are shown in Figure 6-18 as a function of time. Note that the lift force is normalized by the Archimedes force (Eq. 2-1). The lift force clearly exhibits a maximum at the same time instants of τ, for which $\boldsymbol{F_L/F_g} \approx 8$ and ≈ 28 for cases 2 and 3, respectively. The time averaged lift force, $\bar{F}_L$, is calculated as follows:

$$\bar{F}_L = \frac{1}{T}\int_0^T F_L\left(t\sqrt{2g/d_{cd}}\right) d\left(t\sqrt{2g/d_{cd}}\right) \qquad 6\text{-}11$$

that results in $5.79 \times 10^{-5}\ N$ for Case 2 and $5.25 \times 10^{-4}\ N$ for Case 3, corresponding to a value of $\bar{F}_L$ of $O(1)$, about one order of magnitude higher than Case 2. Note that T is set to 7 in both cases. The measurements of the lift force shown here for a rising compound drop - considering Case 2 - is of same order of magnitude to those obtained by Zenit & Magnaudet (2009) for a zigzagging bubble ($\bar{F}_L = 2.98 \times 10^{-5}\ N$). Thus, the lift force acting on a compound drop is similar to that of a typical bubble at similar motion conditions; the compound nature of the drop appears to have little effect on this parameter. Therefore, the lift force on its own cannon be directly associated to the effect of the wake instability and the pendular oscillation.

Figure 6-18. Lift force acting on a compound drop calculated according to Eq. 6-10. The data is normalized by the Archimedes force (Eq. 2-1). The symbols are the same shown in Figure 6-17.

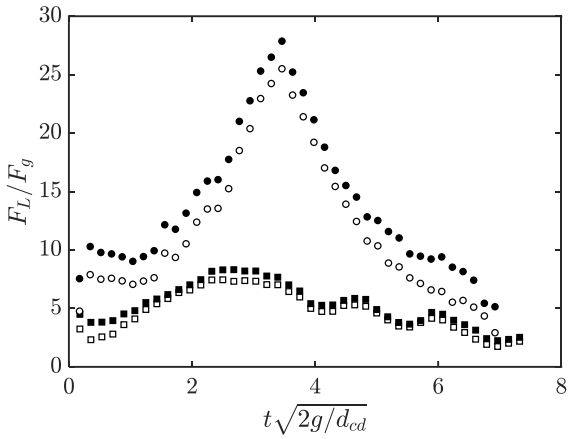

Source: own authorship.

It should once again be stressed that the lift force $\bar{F}_L$ obtained from this methodology is a rough estimation, given that the flow field measurements resemble a Lagangrian field only in the vicinity of the compound drop. Moreover, de Vries et al. (2002) considered only the lift force acting on a bubble by two infinitely long vortices in an inviscid flow. Nevertheless, the estimation of the lift force acting on a compound drop contributes to the understanding of the oscillation dynamics.

6.2.5 *Coupling between wake dynamics and pendular oscillation*

Based on the aforementioned observations, a hypothesis to relate the unsteadiness of the wake to the pendular oscillation is now suggested. Thus far, the structure of the wake resembles that of other typical particles. Therefore, despite the fact that the onset of the oscillations appears to be caused by the instability of the wake, it remains difficult to associate this behavior to the compound nature of the drop.

Firstly, the frequency of the path instabilities is addressed. According to Figure 3-7, the compound drops oscillate with a frequency of roughly 6 Hz, regardless of their diameter ratio. Thus, to consider the effect of inertia observed for larger internal bubbles, the Roshko number is considered, defined as:

$$Ro = \left(\frac{f d_{cd}}{V_{cd}}\right) Re \qquad 6\text{-}12$$

that includes the effect of inertia and oscillation frequency in the characterization of the wake.

Figure 6-19. Roshko number as a function of the Reynolds number (symbols according to Table 5-1). The red line shows the correlation obtained by Ormières & Provansal (1999) for a rigid sphere.

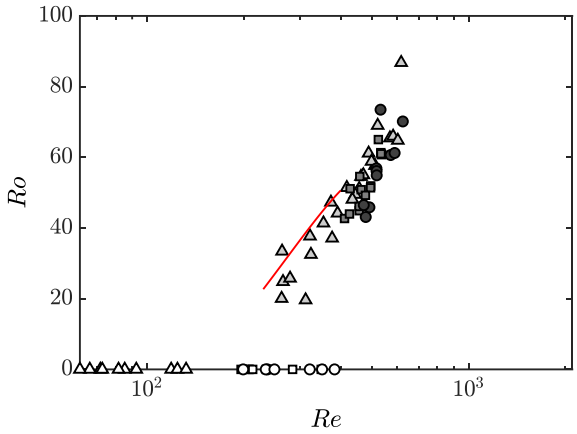

Source: own authorship.

The Roshko number is shown in Figure 6-19 as a function of the Reynolds number. Note that Ro is calculated in terms of the frequency of path oscillations. To check whether the path of a compound drop is similar to a rigid sphere, Figure 6-19 also shows the correlation obtained by Ormières & Provansal (1999) (shown in Figure 6-19 as the red line). The authors associated the oscillatory path of the sphere to the turbulence in its wake and suggested that the inertia of the oscillation evolves as:

$$Ro = -48.2 + 0.391Re - 3.6 \times 10^{-4} Re^2 \qquad 6\text{-}13$$

that agrees well with the measurements. Thus, from a direct analysis of the oscillating path of the compound drops, its behavior appears to be similar to a rigid sphere with same Reynolds.

Next, the frequency of the shedding of vortices in the wake of the compound drop is investigated. The development of unsteadiness is further analyzed by the evolution of the Strouhal number:

$$St_s = \frac{f_s d_{cd}}{V_{cd}} \qquad 6\text{-}14$$

shown in Figure 6-20 as a function of the Reynolds number. Note that the frequency of vortex shedding, f_s, is used instead of the pendular frequency defined in section 6.1. An increase of roughly 60 % has been observed from $Re \approx 320$ (Case 2) to $Re \approx 415$ (Case 3) and is approximately 0.22 for this value of Re. Moreover, the Strouhal of the compound drops evolves as $St_s \propto Re^{1.7}$.

Now, the influence of the fluid inclusion in the wake dynamics is reported. Figure 6-20 also shows the evolutions of Strouhal number for a rigid sphere (black dotted line) and an ellipsoidal bubble (solid blue line). Both trends underestimate the measurements herein presented - specially for Case 3 - suggesting a different behavior of the shedding wake. Moreover, the Strouhal number of the compound drops evolves as $St_s \propto Re^{1.7}$ instead of $Re^{0.6}$ (bubble) and Re^{1} (sphere). This is interesting because it contrasts with the previous measurements that suggested a similarity between the structure of the wake of the compound drops and other common particles. It is now suggested that the pendular oscillation is directly associated to this behavior.

In an attempt to describe the nature of the oscillations it is suggested, based on the pendular behavior described above, to connect the frequency of vortex shedding f_s to the frequency of the pendular oscillation using the harmonic solution for an inviscid pendulum:

$$f_s = \frac{1}{2\pi}\sqrt{\frac{g}{H}} \qquad 6\text{-}15$$

where the bottom width H of the external fluid seems to be a suitable parameter to model the characteristic length of the pendulum since the internal bubble is distorted. Note that Eq. 6-15 is similar to Eq. 5-3 defined earlier to investigate the path instabilities. The overestimation indicates viscous damping.

Figure 6-20. Strouhal number as a function of the Reynolds number. Filled symbols (according to Table 5-1) correspond to Case 2 ($Re \approx 320$) and Case 3 ($Re \approx 415$); The dotted line shows the trend for rigid spheres (Clift et al. (1978) and Sakamoto & Haniu (1990)). Solid lines show the trends for an ellipsoidal bubble (Magnaudet & Mougin, 2007) (blue), Eq. 6-15 (blak) and Eq. 6-16 (red).

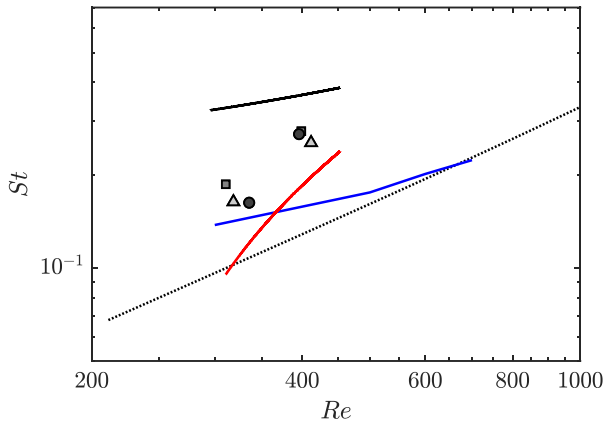

Source: own authorship.

To verify this assumption, the model proposed by Mathai et al. (2019) for a buoyant pendulum can be considered. The authors proposed that viscous drag reduces the frequency of the oscillation and a damped frequency can be obtained:

$$f_d = f_s f^* \qquad 6\text{-}16$$

where f^* is a normalized oscillation frequency that measures the extent of viscous damping. From the data by Mathai et al. (2019), as long as the oscillation amplitude is not too large, f^* depends only on the density ratio of the pendulum, i.e., ρ_{cd}/ρ:

$$f^* = 1 - 0.92\ (\rho_{cd}/\rho) \qquad 6\text{-}17$$

Figure 6-20 shows that Eq. 6-16 resembles the trend of the data herein presented. However, it under predicts the measurements. Note that this comparison is

qualitatively only, insomuch as the compound drops herein studied are different from the system considered by Mathai et al. (2019).

6.3 Flow structures

From the velocity fields shown in Figure 6-12 and in Figure 6-13, it is possible to characterize the wake of the compound drops further by means of the flow structures present in their wake. Focus is now given to the oscillatory cases, for which a significant transient behavior is expected in the dynamics of the wake.

6.3.1 Velocity fluctuations

The velocity and vorticity fields shown in Figure 6-12 and in Figure 6-13 suggest convoluted flow structures in the wake that dissipate with time. To verify this, Figure 6-21 shows the instantaneous measurements of the velocity components, considering Case 2, as listed in Table 3-3. The values of v_x and v_y are shown at the center of each vortex (see Figure 6-12), approximately at ($x/d_{cd} = 0$, $y/d_{cd} = -0.5$) and ($x/d_{cd} = 0$, $y/d_{cd} = +0.5$). Note that this is an approximation given that the position of the center of the vortex changes as the vorticity dissipates.

The velocity fluctuations in the x and y directions, denoted respectively by v'_x and v'_y, are obtained by using the Reynolds decomposition:

$$v'_x(x,y,t) = v_x(x,y,t) - \bar{v}_x(x,y) \qquad 6\text{-}18$$

$$v'_y(x,y,t) = v_y(x,y,t) - \bar{v}_y(x,y) \qquad 6\text{-}19$$

where $\bar{v}_x(x,y)$ and $\bar{v}_y(x,y)$ are the time-averaged values, shown in Figure 6-21 as the black solid line. The values of the velocity components are fluctuating with time. Moreover, $\left|\bar{v}_y/\bar{v}_x\right|_{y/d_{cd}=-0.5} \approx 0.3$ and $\left|\bar{v}_y/\bar{v}_x\right|_{y/d_{cd}=0.5} \approx 0.25$ for the vortex with negative and positive values of streamwise vorticity, respectively. This difference between the magnitudes of each velocity component is presumably a consequence of the lateral migration in the x direction that increases this velocity component.

Figure 6-21. Velocity fluctuations in the $x-y$ plane for Case 2, as listed in Table 3-3. Top row: x direction in the positive (a) and negative (b) vortices. Bottom row: y direction in the positive (c) and negative (d) vortices. The temporal measurements are obtained from Figure 6-12 at the point of highest vorticity, near the center of each vortex. The black solid line shows the temporal average.

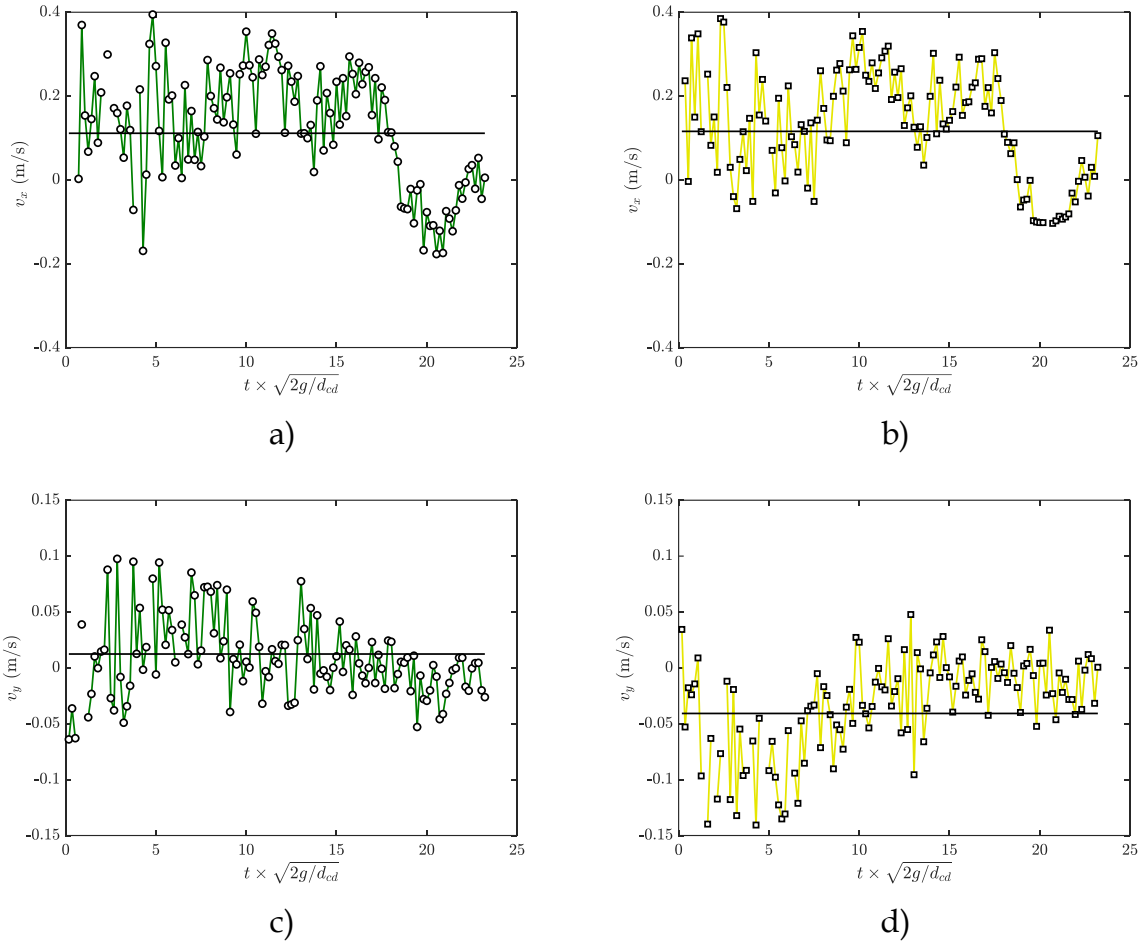

Source: own authorship.

A similar behavior is depicted for the wake behind the compound drop considering Case 3, whose velocity fluctuations are shown in Figure 6-22. For this increased complex structure of the wake, both v_x and v_y apparently present alternate positive and negative magnitudes. Thus, despite $\bar{v}_x(x,y)$ and $\bar{v}_y(x,y)$ being closer to zero for Case 3, the amplitude of the velocity fluctuations is higher, revealing a more complex flow within each vortex. Note that only the portion of the wake that remains attached to the compound drop is analyzed, roughly at $z/d_{cd} < 5$.

The transverse profile of the velocity fluctuations may contribute to the analysis of the flow structures in the wake and to investigate the effects of viscous dissipation. Figure 6-23 shows the transverse profile in the y direction of the instantaneous

measurements of the velocity components at $x/d_{cd} = 0$. The measurements are obtained from the velocity field shown in Figure 6-12, considering Case 2, as listed in Table 3-3. The time-averaged values $\bar{v}_x$ and $\bar{v}_y$ are also shown (empty markers); the errorbars represent the amplitude of the velocity fluctuations.

Figure 6-22. Velocity fluctuations in the $x-y$ plane for Case 3, as listed in Table 3-3. Top row: x direction in the positive (a) and negative (b) vortices. Bottom row: y direction in the positive (c) and negative (d) vortices. The temporal measurements are obtained from Figure 6-12 at the point of highest vorticity, near the center of each vortex. The black solid line shows the temporal average.

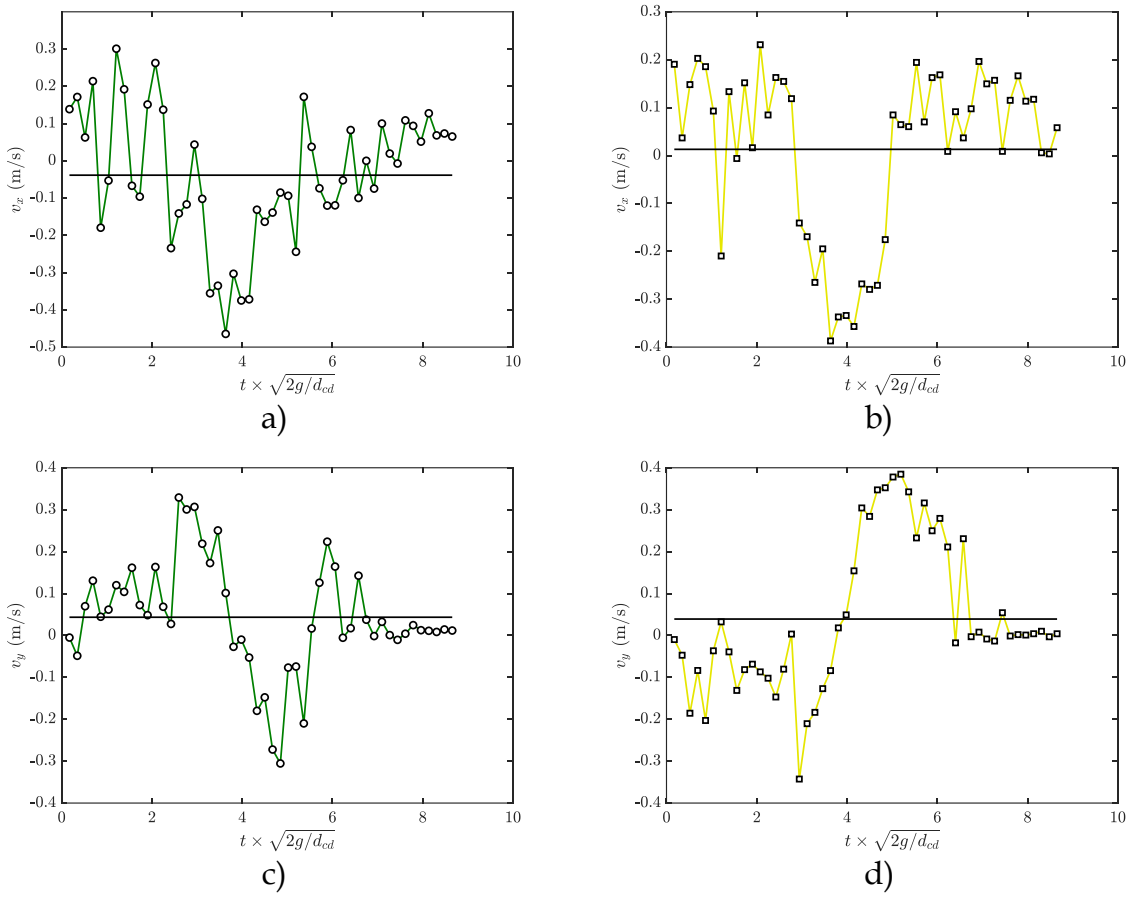

Source: own authorship.

From Figure 6-23a it can be seen that v_x has a peak at $y/d_{cd} \approx 0$ corresponding to the gap between the positive and negative vortices (see Figure 6-12) where $\omega_z \to 0$ and the velocity vectors are aligned in the x direction. On the other hand, v_y (Figure 6-23b) has a peak and a valley at the vortex centers at $y/d_{cd} \approx -0.5$ and $y/d_{cd} \approx +0.5$, respectively. Moreover, from Figure 6-23 the effect of viscous dissipation is clear, where the amplitude of the fluctuations of v_x and v_y decrease in the y direction.

Figure 6-23. Transversal profile of the velocity fluctuations in the x (a) and y (b) directions for Case 2 (Table 3-3). The position in the x direction is fixed at $x/d_{cd} = 0$. The empty markers show the time averaged velocity for each position in the y direction. The blue error bars indicate the amplitude of the velocity fluctuations. The velocities are made dimensionless by $V_{axis} = |v_{x(y=0)}|$.

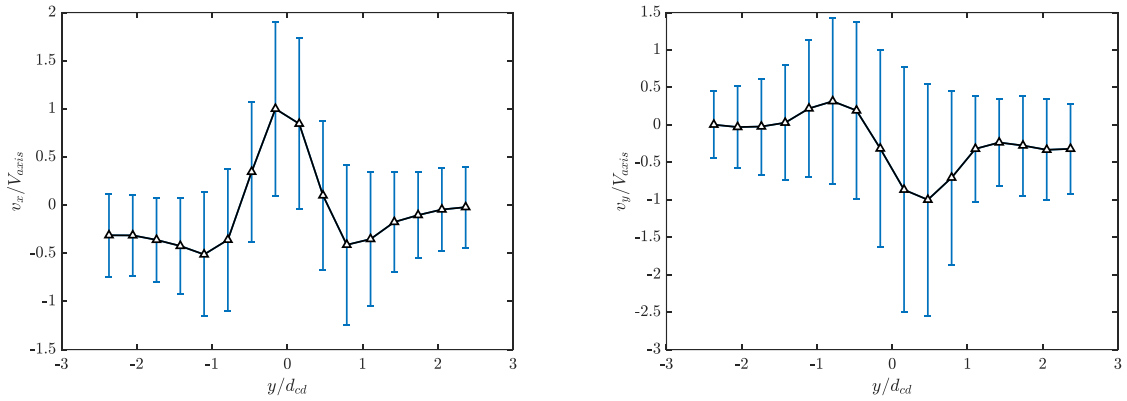

a) b)

Source: own authorship.

Figure 6-24. Transversal profile of the velocity fluctuations in the x (a) and y (b) directions for Case 3 (Table 3-3). The position in the y direction is fixed at $x/d_{cd} = -2$. The symbols are the same from Figure 6-23. The velocities are made dimensionless by $V_{axis} = |v_{x(y=0)}|$.

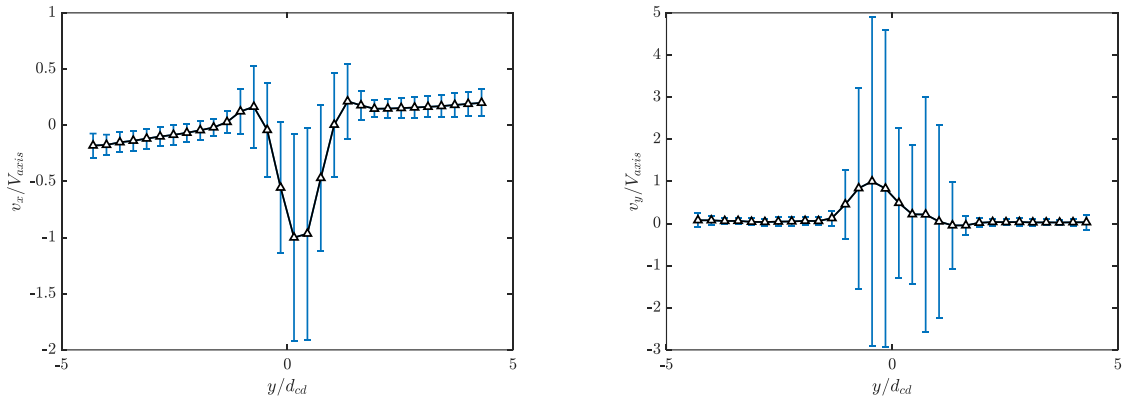

a) b)

Source: own authorship.

A similar profile is identified for the fully-developed oscillatory regime (Case 3 from Table 3-3), shown in Figure 6-24. The instantaneous measurements of the velocity components are obtained from the velocity and vorticity fields shown in Figure 6-13. The position in the x direction is now fixed at $x/d_{cd} = -2$, the approximate location of the center of the vortex pair. The resemblance to the velocity profile shown in Figure

6-23 is striking. The time-averaged velocities $\bar{v}_x$ and $\bar{v}_y$ show distinguished inflection points between the positive and negative vortices and in the vortex centers, respectively. The difference lies in the magnitude of the velocity fluctuations. The rapid decay in the y direction suggests a higher rate of viscous dissipation for the oscillatory regime.

6.3.2 Turbulence intensity and Reynolds stresses

The fluctuating velocity profiles shown in Figure 6-23 and Figure 6-24 suggest a complex flow structure in the discrete pockets of streamwise vorticity in the wake of the compound drop. To quantify this, the turbulence intensity I is calculated as:

$$I = \left[\frac{1}{T}\int_0^T [v'(x,y,t)]^2 d\left(t\sqrt{2g/d_{cd}}\right)\right]^{1/2} \qquad 6\text{-}20$$

where $v'(x,y,t) = \left[\left(v'_x(x,y,t)\right)^2 + \left(v'_y(x,y,t)\right)^2\right]^{1/2}$ is the fluctuation in the velocity magnitude. Figure 6-25a confirms the peak in the turbulence intensity near the center of the vortex pair at $y/d_{cd} \approx 0$, particularly for Case 3 where I is of order $O(1)$ when compared to Case 2. The dissipation of I in the y direction occurs swiftly and $I \to 0$ when $y/d_{cd} > 2$.

The turbulence intensity I provides the averaged profile of the velocity fluctuations and does not necessarily take the swirling within each vortex into account. The behavior of the Reynolds stresses calculated as:

$$\overline{v'_x v'_y} = -\frac{1}{T}\int_0^T \left[v'_x(x,y,t)\cdot v'_y(x,y,t)\right] d\left(t\sqrt{2g/d_{cd}}\right) \qquad 6\text{-}21$$

can provide further information of the flow at the vortex centers since this parameter considers the fluctuations of each component individually. The profile of the Reynolds stresses is shown in Figure 6-25b where two inflections points are identified, roughly at $y/d_{cd} = -0.5$ and $+0.5$, i.e., near the vortex centers. Thus, the fluctuations in the

velocity components may be a consequence of the streamwise vorticity with $\overline{v_x' v_y'} \propto \omega_z$. As aforementioned, from the temporal behavior described earlier, it may be inferred that some turbulent effects are identified in the wake of an oscillating compound drop.

Figure 6-25. Transversal profile of the turbulence intensity (a) and Reynolds stresses (b) obtained from Eq. 6-20 and Eq. 6-21, respectively. ( ) and ( ) show the measurements for cases 2 and 3, respectively, as listed in Table 3-3. The fixed x-position is the same from previous plots.

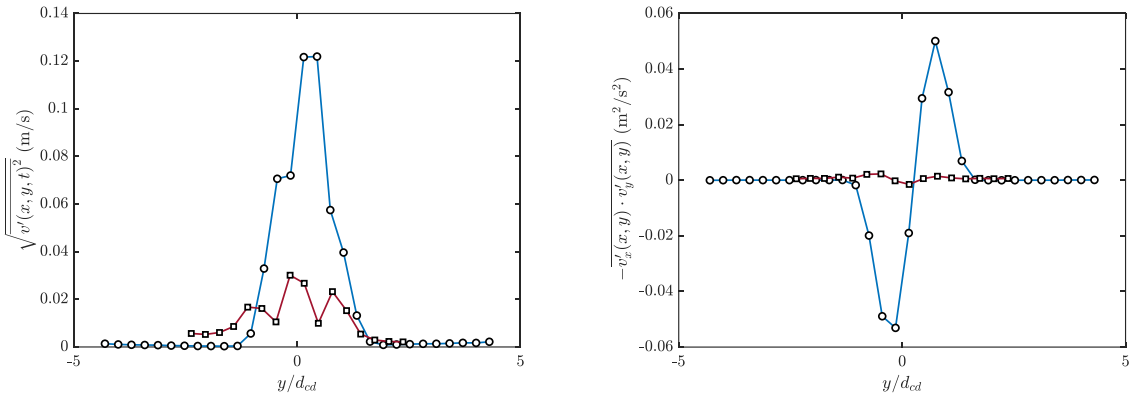

a) b)

Source: own authorship.

6.4 Final remarks

In this chapter, the physical mechanisms governing the motion transition of the compound drop from straight to oscillatory motion were experimentally investigated by using flow visualization techniques. Measurements of the path, shape, and orientation of the compound drop as a function of the diameter ratio d_b/d_{cd} were reported. Furthermore, the behavior of the continuous phase was also investigated.

The measurements suggest that the rising path of the compound drop evolved from rectilinear to oscillatory depending on the diameter ratio. Regardless of the motion regime, the compound drops presented an eccentric configuration caused by the migration of the internal bubble promoted by buoyancy.

A relative motion was observed for the external centroid with regard to the internal phase that led to a pendular oscillation. The inner bubble oscillated with

reduced amplitude and with a temporal delay that was inversely proportional to the thickness of the external layer. Shape fluctuations were also observed and they appeared to have the same magnitude as the pendular oscillation as long as the internal bubble is not too large ($d_b/d_{cd} \to 1$), suggesting a coupled oscillation. Otherwise, one oscillation mechanism becomes dominant for each fluid: shape and orientation oscillations for the internal and external fluids, respectively.

The instability of the wake is at the onset of the unsteadiness of the motion. Experiments using a PIV system were conducted and they showed that the axisymmetric wake became unstable when, for larger Reynolds numbers, the diameter ratio exceeded a critical value of $d_b/d_{cd} > 0.6$, approximately. This claim was supported by the measurements of the liquid-induced velocity as well as the distribution of normal and streamwise vorticities. Although a similar behavior has been extensively reported in literature for typical bubbles, the main difference is that in the case of the compound drops the transition is not governed by the shape distortion. Instead, the diameter ratio d_b/d_{cd} together with the Strouhal number seem to be more suitable to predict the onset of unsteadiness.

The structure and the dynamics of the wake strongly evolved with d_b/d_{cd}. For a compound drop in rectilinear motion, a long wake is reported; essentially two vortex filaments of streamwise vorticity that dissipated along the path. Transition occurred when discrete pockets of vorticity were shed in the wake, as the symmetry axis of the compound drop became inclined with regard to the vertical direction. Further instabilities arose once the oscillatory motion developed at which point the vortex pairs have alternate vorticity signs.

A different evolution of the shedding frequency was observed for the compound drops and the Strouhal number St evolved as $Re^{1.7}$, substantially higher in comparison to bubbles and spheres and suggesting a distinguished wake structure. It is hinted that the pendular oscillation was responsible for this behavior and a simple model of St that presented a good agreement with the measurements was proposed. However, further analysis about this matter is encouraged.

The wake of an oscillating compound drop developed two vortex tubes of streamwise vorticity that promoted a lateral force that contributed to the lateral migration of the compound drop. Measurements of the velocity and vorticity fields have shown that the wake behind a compound drop is similar to that of an oscillating bubble. At the onset of the oscillation, the wake still presented a planar symmetry; the cross-sectional area of the vortex tubes then reduced as a consequence of the viscous dissipation. Once the path instability of the compound drop evolved, the planar symmetry is lost and a fully unstable and intermittent wake was developed.

Measurements of the fluctuating velocity field in the wake suggested further complex flow structures behind the compound drop. Despite the clear evolution of the magnitude of the fluctuations with the instability of the wake, details regarding the physical origin of the fluctuations still remain unclear. Further analysis to investigate whether the fluctuations in velocity arose from turbulence or organized motion is under conduction. Moreover, despite the similarities in the triggering of the instability of the wake with typical flows involving single-fluid bubbles, the physical mechanisms involved in the development of the wake structure are still not completely understood.

7 CONCLUSIONS AND PERSPECTIVES

The dynamics of compound drops rising at high Reynolds numbers were investigated. To the best of the current knowledge, the effect of inertia in the motion of the compound drops had not yet been investigated to this date. By using the high-speed shadowgraph and particle image velocimetry (PIV) techniques, measurements of the path, shape, velocity, drag, and the structure of the wake were reported.

The size of the internal bubble determined the rising path of the compound drop, which evolved from rectilinear to oscillatory for all fluids tested. The compound drops showed a distinguished mechanism of oscillation: the external centroid moves around the internal one following a pendular behavior. The compound and eccentric nature of the drops studied here were crucial in the development of this oscillation regime. Measurements of the Strouhal number corroborated this observation, where the distinguished evolution from typical particles, e.g., bubbles, drops, and spheres, suggested a different oscillation mechanism. The shape of both the internal and external phases of the compound drop have shown to be largely dependent on their compound structure. Additional dimensionless parameters were defined to account for the secondary pressure jump present at the second interface, leading to a better characterization of their shape.

The unsteadiness of the wake is at the onset of path instabilities. When the size of the inner bubble reaches a critical value, the rate of vorticity generated at the bottom segment of the compound drop increases beyond the stability threshold; the wake is no longer symmetrical because of symmetry breakdowns induced by fluid separation. The rising regime of the compound drops greatly affected the parameters of the motion, in particular the drag coefficient. For the case when the path is straight, the drag coefficient behaved similarly as a rigid sphere; the inner bubble induced only a slight decrease of this parameter. However, for the oscillatory compound drops, the drag coefficient seemed to be governed by the diameter ratio instead of the Reynolds number. Clearly, the instability of the wake contributed to this behavior.

Despite the observations herein presented, the understanding of the dynamic behavior of rising compound drops is far from complete. For instance, the role played by surface contamination should be investigated with more detail. A more complete modeling for the drag coefficient should consider the internal circulation instead of averaged fluid properties. Moreover, details regarding the symmetry breakdown in the wake of the compound drop would contribute to the characterization of the motion transition. Some of these features are difficult to investigate experimentally and require computational methods. Hopefully, other researchers may address some of these issues with more detail in the future.

REFERENCES

ABATE, A. R.; WEITZ, D. A. **High-order multiple emulsions formed in poly(dymethyilsiloxane) microfluidics**. In: Small 5.18 (2009), pp. 2030–2032. doi: 10.1002/smll.200900569.

ALBERT, C.; KROMER, J.; ROBERTSON, A. M.; BOTHE, D. **Dynamic behaviour of buoyant high viscosity droplets rising in a quiescent liquid**. In: J. Fluid Mech. 778 (2015), pp. 458–533. doi: 10.1017/jfm.2015.393.

AOYAMA, S.; HAYASHI, K.; HOSOKAWA, S.; TOMIYAMA, A. **Shapes of ellipsoidal bubbles in infinite stagnant liquids**. In: Int. J. Multiphase Flow 79 (2016), pp. 23–30. doi: 10.1016/j.ijmultiphaseflow.2015.10.003.

BASHIR, S.; SOLVAS, X. C.; BASHIR, M.; REES, J. M.; ZIMMERMAN, W. J. **Dynamic wetting in microfluidic droplet formation**. In: BioChip. J. 8 (2014), pp. 122–128. doi: 10.1007/s13206-014-8207-y.

BAZHLEKOV, I. B.; SHOPOV, P. J.; ZAPRYANOV, Z. D. **Unsteady motion of a type-A compound multiphase drop at moderate Reynolds numbers**. In: J. Colloid Interface Sci. 169.1 (1995), pp. 1–12. doi: 10.1006/jcis.1995.1001.

BECKER, E.; HILLER, W. J.; KOWALEWSKI, T. A. **Experimental and theoretical investigation of large amplitude oscillations of liquid droplets**. In: J. Fluid Mech. 231 (1991), pp. 189–210. doi: 10.1017/ S0022112091003361.

BLANKEN, N.; SALEEM, M. S.; THORVAL, M.; ANTONINI, C. **Impact of compound drops: A perspective.** In: Curr. Opin. Colloid In. 51.101389 (2021). doi: 10.1016/j.cocis.2020.09.002.

BIESHEUVEL, A.; WINJGAARDEN, L. **Two-phase flow equations for a dilute dispersion of gas bubbles in a liquid.** In: J. Fluid Mech. 148 (1984), pp. 301–318. doi: 10.1017/S0022112084002366.

BRUNN, P. O.; RODEN, T. **On the deformation and drag of a type-a multiple drop at low Reynolds number**. In: J. Fluid Mech. 160 (1985), pp. 211–234. doi: 10.1017/S0022112085003457.

BRÜCKER, C. **Structure and dynamics of the wake of bubbles and its relevance for bubble interaction**. In: Phys Fluids 11.7 (1999). doi: 10.1063/1.870043.

CHAITHANYA, K. V. S.; THAMPI, S. P. **Dynamics and stability of a concentric compound particle – a theoretical study**. In: Soft Matter 15 (2019), pp. 7605–7615. doi: 10.1039/C9SM01332F.

CHARIN, A. H. L. M.; LAGE, P. L. C.; SILVA, L. F. L. R.; TUKOVIC, Z.; JASAK, H. **On the dynamic behavior of rising droplets**. In: Int. J. Multiphase Flow 110 (2019), pp. 165–178. doi: 10.1016/j.ijmultiphaseflow.2018.09.005.

CHEBEL, N. A.; VEJRAZKA, J.; MASBERNAT, O.; RISSO, F. **Shape oscillations of an oil drop rising in water: effect of surface contamination**. In: J. Fluid Mech. 702 (2012), pp. 533–542. doi: 10.1017/Jfm.2012.205.

CHEN, Y.; LIU, X.; ZHAO, Y. **Deformation dynamics of double emulsion droplet under shear**. In: App. Phys. Lett. 106.141601 (2015). doi: 10.1063/1.4916623.

CLIFT, R.; GRACE, J. R.; WEBER, M. E. **Bubbles, drops, and particles**. 15 Wellman Avenue, North Chelmsford, MA 01863.: Courier Corporation, 1978.

DAS, S.; MANDAL, S.; CHAKRABORTY, S. **Interfacial viscosity-dictated morpho-dynamics of a compound drop in linear flows**. In: Phys. Fluids 32.062006 (2020), pp. –. doi: 10.1063/5.0009659.

DEKA, H.; BISWAS, C.; SAHU, K. C.; KULKARNI, Y.; DALAL, A. **Coalescence dynamics of a compound drop on a deep liquid pool**. In: J. Fluid Mech. 866 (2019). doi: 10.1017/jfm.2019.137.

DUDEK, M.; OYE, G. **Midrofluidic study on the attachment of crude oil droplets to gas bubbles**. In: Energy Fuels 32.10 (2018), pp. 10513–10521. doi: 10.1021/acs.energyfuels.8b02236.

DUINEVELD, P. C. **The rise velocity and shape of bubbles in pure water at high Reynolds number**. In: J. Fluid Mech. 292 (1995), pp. 325–332. doi: 10.1017/S0022112095001546.

EDGE, R. M.; GRANT, D. C. **The terminal velocity and frequency of oscillation of drops in pure systems**. In: Chem. Eng. Sci. 26.7 (1971), pp. 1001–1012. doi: 10.1016/0009-2509(71)80013-1.

ELLINGSEN, K.; RISSO, F. **On the rise of an ellipsoidal bubble in water: oscillatory paths and liquid induced velocity**. In: J. Fluid Mech. 440 (2001), pp. 235–268. doi: 10.1017/S0022112001004761.

ERN, P.; RISSO, F.; FABRE, D.; MAGNAUDET, J. **Wake-induced oscillatory paths of bodies freely rising or falling in fluids**. In: Ann. Rev. Fluid Mech. 44 (2012), pp. 97–121. doi: 10.1146/annurev-fluid-120710-101250.

GAONKAR, A. G. **Interfacial tensions of vegetable oil/water systems: effect of oil purification**. In: JACCS 66.8 (1989), pp. 1090–1092. doi: 10.1007/BF02670090.

GHIDERSA, B.; DUSEK, J. **Breaking of axisymmetry and onset of unsteadiness in the wake of a sphere**. In: J. Fluid Mech. 432 (2000), pp. 235–268. doi: 10.1017/S0022112000001701.

HAYAKAWA, T.; SHIGETA, M. **Terminal velocity of two-phase droplet**. In: Journal of Chemical Engineering of Japan 7.2 (1974), pp. 140–142. doi: 10.1252/jcej.7.140.

HUA, H.; SHIN, J.; KIM, J. **Dynamics of a compound droplet in shear flow**. In: Int. J. Heat Fluid Fl. 50 (2014), pp. 63–71. doi: 10.1016/j.ijheatfluidflow.2014.05.007.

HUANG, S.; FRANEKL, E. N.; AESCHBACH, R.; GERMAN, J. B. **Partition of selected antioxidants in corn oil-water model systems**. In: J. Agric. Food Chem. 45.6 (1997), pp. 1991–1994. doi: 10.1021/jf9701695.

JOHNSON, R. E.; SADHAL, S. S. **Fluid mechanics of compound multiphase drops and bubbles**. In: Ann. Rev. Fluid Mech. 17 (1985), pp. 289–320. doi: 10.1146/annurev.fl.17.010185.001445.

JOHNSON, R. E.; SADHAL, S. S. **Stokes flow past bubbles and drops partially coated with thin films - A perturbation solution**. In: J. Fluid. Mech. 132 (1983), pp. 295–318. doi: 10.1017/S0022112083001627.

KAN, H. C.; UDAYKUMAR, H. S.; SHYY, W.; TAY-SON-TAY, R. **Hydrodynamics of a compound drop with application to leukocyte modeling**. In: Phys. Fluids 10.760 (1998), pp. –. doi: 10.1063/1.869601.

KAWANO, S.; HASHIMOTO, H. **A numerical study on motion of a sphere coated with a thin liquid film at intermediate Reynolds numbers**. In: J. Fluids Eng. 119.2 (1997), pp. 397–403. doi: 10.1115/1.2819147.

LALANNE, B.; CHABEL, N. A.; VEJRAZKA, J.; TANGUY, S.; MASBERNAT, O.; RISSO, F. **Non-linear shape oscillations of rising drops and bubbles: Experiments and simulations**. In: Phys. Fluids 27.123305 (2015). doi: 10.1063/1.4936980.

LAMB, H. **Hydrodynamics**. Shaftesbury Rd, Cambridge CB2 8BS, UK: Cambridge University Press, 1932.

LANDMAN, K. A. **Stability of a viscous compound fluid drop**. In: AIChE J. 31.4 (1985), pp. 567–573. doi: 10.1002/aic.690310406.

LEGENDRE, D.; ZENIT, R.; VELEZ-CORDERO, J. R. **On the deformation of gas bubbles in liquids**. In: Phys. Fluids 24.04303 (2012). doi: 10.1063/1.4705527.

LEGENDRE, D. **Quelques aspects des forces hydrodynamiques et des transferts de chaleur sur une bulle sphérique**. PhD Thesis (1996).

LINDNER, J. R. **Microbubbles in medical imaging: current applications and future directions**. In: Nat. Rev. Drug Discov. 3 (2004), pp. 527–532. doi: 10.1038/nrd1417.

LINDT, J. T.; DE GROOT, R. G. F. **The drag on a single bubble accompanied by a periodic wake**. In: Chem. Eng. Sci. 29.4 (1974), pp. 957–962. doi: 10.1016/0009-2509(74)80087-4.

LIU, K.; SUGIYAMA, K.; TAKAGI, S. **On the interaction of two encapsulated bubbles in an ultrasound field**. In: J. Fluid Mech. 804 (2016), pp. 58–89. doi: 10.1017/jfm.2016.525.

KIU, H.; LU, Y.; LI, S.; YU, Y.; SAHU, K. C. **Deformation and breakup of a compound droplet in three-dimensional oscillatory shear flow**. In: Int. J. Multiphase Flow 134.103472 (2021). doi: 10.1016/j.ijmultiphaseflow.2020.103472.

LUNDE, K.; PERKINS, R. J. **Shape oscillations of rising bubbles**. In: Appl. Sci. Res. 58 (1997), pp. 387–408. doi: 10.1023/A:1000864525753.

MAGNAUDET, J. **The forces acting on bubbles and rigid particles**. In: FEDSM97 - 3522 (1997), pp. –.

MAGNAUDET, J.; MOGIN, G. **Wake instability of a fixed spheroidal bubble**. In: J. Fluid Mech. 72 (2007), pp. 311–337. doi: 10.1017/S0022112006003442.

MANDAL, S.; GOSH, U.; CHAKRABORTY, S. **Effect of surfactant on motion and deformation of compound droplets in arbitrary unbounded Stokes flow**. In: J. Fluid Mech. 803 (2016), pp. 200–249. doi: 10. 1017/jfm.2016.497.

MATHAI, V.; LOEFFEN, L. A. V. W.; CHAN, T. T. K.; WILDEMAN, S. **Dynamics of heavy and buoyant underwater pendulums**. In: J. Fluid Mech. 862 (2019), pp. 348–363. doi: 10.1017/jfm.2018.867.

MEI, R.; KLAUSNER, J. F.; LAWRENCE, C. J. **A note on the history force on a spherical bubble at finite Reynolds number**. In: Phys. Fluids 6.418 (1994). doi: 10.1063/1.868039.

MERCIER, J. L.; DA CUNHA, F. M.; TEIXEIRA, J. C.; SCOFIELD, M.P. **Influence of enveloping water layer on the rise of air bubbles in Newtonian fluids**. In: J. Appl. Mech. 41.1 (1974), pp. 29–34. doi: 10.1115/1.3423253.

MOORE, D. W. **The velocity of rise of distorted gas bubbles in a liquid of small viscosity**. In: J. Fluid Mech. 23.4 (1965), pp. 749–766. doi: 10.1017/S0022112065001660.

MOUGIN, G.; MAGNAUDET, J. **Path Instability of a Rising Bubble**. In: Phys. Rev. Lett. 88.014502 (2001), pp. –. doi: 10.1103/PhysRevLett.88.014502.

MORI, Y. H. **Configurations of gas-liquid two-phase bubbles in immiscible liquid media**. In: Int. J. Multiphase Flow 4.4 (1978), pp. 383–396. doi: 10.1016/0301-9322(78)90032-0.

MORI, Y. H.; KMOTORI, K.; HIGETA, K.; INADA, J. **Rising behavior of air bubbles in superposed liquid layers**. In: The Canadian Journal of Chemical Engineering 55.1 (1977), pp. 9–12. doi: 10.1002/cjce.5450550103.

MUNGALL, J. E.; BRENNAN, J. M.; GODEL, B.; BARNES, S. J.; GAILLARD, F. **Transport of metals and sulphur in magmas by flotation of sulphide melt on vapour bubbles**. In: Nature Geosci. 8 (2015), pp. 216–219. doi: 10.1038/ngeo2373.

NEESON, M. J.; TABOR, R. F.; GRIESER, F.; DAGASTINE, R. R.; CHAN, D. Y. C. **Compound sessile drops**. In: Soft Matter 8 (2012), pp. 11042–11050. doi: 10. 1039/c2sm26637g.

ORMIÈRES, D.; PROVANSAL, M. **Transition to turbulence in the wake of a sphere**. In: Phys. Rev. Lett. 83.1 (1999), pp. 80–83. doi: 10.1103/PhysRevLett.83.80.

PATZER, J. F.; HOMSY, G. M. **Hydrodynamic stability of thin spherically concentric fluid shells**. In: J. Colloid Interface Sci. 51.3 (1975), pp. 499–508. doi: 10.1016/0021-9797(75)90146-0.

PROSPERETTI, A.; OHL, C.; TIJINK, A.; MOUGIN, G.; MAGNAUDET, J. **Leonardo's paradox. Appendix to A. Prosperetti, C. D. Ohl, A. Tijink**. In: J. Fluid Mech. 482 (2003), pp. 286–289.

QU, X.; WANG, Y. **Dynamics of concentric and eccentric compound droplets suspended in extensional flows**. In: Phys. Fluids 24.123302 (2012). doi: 10.1063/1.4770294.

RACHIH, A.; LEGENDRE, D.; CLIMENT, E.; CHARTON, S. **Numerical study of conjugate mass transfer from a spherical droplet at moderate Reynolds number**. In: Int. J. Heat Mass Transf. 157.119958 (2020). doi: 10.1016/j.ijheatmasstransfer.2020.119958.

RAFFEL, M.; WILLERT, C. E.; SCARANO, F.; KAHLER, C. J.; WERELEY, S. T.; KOMPENHANS, J. **Particle image velocimetry: a practical guide**. Tiergartenstrasse 17 D-69121: Springer-Verlag GmbH, 1998.

RIBOUX, G.; LEGENDRE, D.; RISSO, F. **A model of bubble-induced turbulence based on large-scale wake interactions**. In: J. Fluid Mech. 719 (2013), pp. 362–387. doi: 10.1017/jfm.2013.12.

ROIG, V.; ROUDET, M.; RISSO, F.; BILLET, A. **Dynamics of a high-reynolds-number bubble rising within a thin gap**. In: J. Fluid Mech. 707 (2012), pp. 444–466. doi: 10.1017/jfm.2012.289.

RUSHTON, E.; DAVIES, G. A. **Settling of encapsulated droplets at low Reynolds numbers**. In: Int. J. Multiphase Flow 9 (1983), pp. 337–342. doi: 10.1016/0301-9322(83)90111-8.

SAKAMOTO, H.; HANIU, H. **A study on vortex shedding from spheres in a uniform flow**. In: J. Fluids Eng. 112.4 (1990), pp. 386–392. doi: 10.1115/1.2909415.

SANADA, T.; SUGIHARA, K.; SHIROTA, M.; WATANABE, M. **Motion and drag of a single bubble in super-purified water**. In: Fluid Dyn. Res. 40 (2008), pp. 534–545. doi: 10.1016/j.fluiddyn.2007.12.005.

SATHTHASIVAM, J.; LOGANATHAN, K.; SARP, S. **An overview of oil-water separation using gas flotation systems**. In: Chemosphere 144 (2016), pp. 671–680. doi: 10.1016/j.chemosphere.2015.08.087.

SCHILLER, L.; NAUMANN, A. **A drag coefficient correlation**. In: Zeit. Ver. Deutsch. Ing. 77 (1933), pp. 318–320.

SELECKI, A.; GRADON, L. **Equation of motion of an expanding vapour drop in an immiscible liquid medium**. In: Int. J. Heat Mass Transf. 19.8 (1976), pp. 925–929. doi: 10.1016/0017-9310(76)90204-0.

SEGRÉ, G.; SILBERBERG, A. **Behaviour of microscopic rigid spheres in poiseulle flow**. In: J. Fluid Mech. 14 (1962), pp. 115–157. doi: 10.1017/S002211206200110X.

SHANKAR, N.; SUBRAMANIAN, R. S. **The slow axisymmetric thermocapillary migration of an eccentrically placed bubble inside a drop in zero gravity**. In: J. Colloid Interface Sci. 94.1 (1983), pp. 258–275. doi: 10.1016/0021-9797(83)90256-4.

SIJL, J.; DOLLET, B.; OVERVELDE, M.; GARBIN, V.; ROZENDAL, T.; JONG, N.; LOHSE, D.; VERSLUIS, M. **Subharmonic behavior of phospholipid-coated ultrasound contrast agent microbubbles**. In: J. Acoust. Soc. Am. 128.5 (2010), pp. 3239–3252. doi: 10.1121/1.3493443.

SONG, Y.; XU, J.; YANG, Y. **Stokes flow past a compound drop in a circular tube**. In: Phys. Fluids 22.072003 (2010), pp. –. doi: 10.1063/1.3460301.

STONE, H. A.; LEAL, L. G. **Breakup of concentric double emulsion droplets in linear flows**. In: J. Fluid Mech. 211 (1990), pp. 123–156. doi: 10.1017/S0022112090001525.

STROEVE, P.; VARANASI, P. P. **An experimental study on double emulsion drop breakup in uniform shear flow**. In: J. Colloid Interface Sci. 99.2 (1984), pp. 360–373. doi: 10.1016/0021-9797(84)90123- 1.

TAMBOULIDES, A. G.; ORSZAG, S. A. **Numerical investigation of transitional and weak turbulent flow past a sphere**. In: J. Fluid Mech. 416 (2000), pp. 45–73. doi: 10.1017/S0022112000008880.

TOMIYAMA, A.; KATAOBA, I.; ZUN, I.; SAKAGUCHI, T. **Drag coefficients of single bubbles under normal and micro gravity conditions**. In: JSME Int. J. 41.2 (1998), pp. 472–479. doi: 10.1299/jsmeb.41.472.

TORZA, S.; COX, R. G.; MASON, S. G. **Particle motions in sheared suspensions XXVII. Transient and steady deformation and burst of liquid drops**. In: J. Colloid Interface Sci. 38.2 (1972), pp. 395–411. doi: 10.1016/0021-9797(72)90255-X.

TORZA, S.; MASON, S. G. **Three-phase interactions in shear and electrical fields**. In: J. Colloid Interface Sci. 33 (1970), pp. 67–83. doi: 10.1016/0021-9797(70)90073-1.

TRIPATHI, M. K.; SAHU, K. C.; GOVINDARAJAN, R. **Dynamics of an initially spherical bubble rising in quiescent liquid**. In: Nat. Commun. 6.6268 (2015), pp. –. doi: 10.1038/ncomms7268.

TSAMOPOULOS, J. A.; BROWN, R. A. **Dynamic centering of liquid shells**. In: Phys. Fluids 30.27 (1987), pp. –. doi: 10.1063/1.866190.

ULBRECHT, J. J.; STROEVE, P.; PRABODH, P. **Behaviour of double emulsions in shear flows**. In: Rheol. Acta 21 (1982), pp. 593–597. doi: 10.1007/978-3-662-12809-1_63.

DE VRIES, A.; BIESHEUVEL, A.; VAN WINJGAARDEN, L. **Notes on the path and wake of a gas bubble rising in pure water**. In: Int. J. Multiphase Flow 28 (2002), pp. 1823–1835. doi: 10.1016/S0301-9322(02)00036-8.

VU, T.; VU, T. V.; NGUYEN, C. T.; PHAM, P. H. **Deformation and breakup of a double-core compound droplet in an axisymmetric channel**. In: International Journal of Heat and Mass Transfer 135 (2019), pp. 796–810. doi: 10 . 1016 / j . ijheatmasstransfer.2019.02.032.

WANG, S.; ZHANG, Y.; MEREDITH, J. C.; BEHRENS, S. H.; TRIPATHI, M. K.; SAHU, K. C. **The dynamics of rising oil-coated bubbles: experiments and simulations**. In: Soft Matter 14 (2018), pp. 2724–2734. doi: 10.1039/C7SM01603D.

WELLEK, R. M.; ANGRAWAL, A. K.; SKELLAND, A. H. P. **Shape of liquid drops moving in liquid media**. In: AIChE J. 12 (1966), pp. 854–866. doi: 10.1002/aic.690120506.

WINNIKOV, S.; CHAO, B. T. **Droplet motion in purified systems**. In: Phys. Fluids 9.1 (1966). doi: 10.1063/1.1761532.

WU, M.; GHARIB, M. **Experimental studies on the shape and path of small air bubbles rising in clean water**. In: Phys Fluids 14. L49 (2002). doi: 10.1063/1.1485767.

YANG, B.; PROSPERETTI, A. **Linear stability of the flow past a spheroidal bubble**. In: J. Fluid Mech. 582 (2007), pp. 53–78. doi: 10.1017/S0022112007005691.

ZENIT, R.; MAGNAUDET, J. **Path instability of rising spheroidal air bubbles: A shape-controlled process**. In: Phys. Fluids 20.061702 (2008). doi: 10.1063/1.2940368.

ZENIT, R.; MAGNAUDET, J. **Measurements of the streamwise vorticity in the wake of an oscillating bubble**. In: Int. J. Multiphase Flow 35 (2009), pp. 195–203. doi: 10.1016/j.ijmultiphaseflow.2008.10.007.

ZHANG, Y.; CHATAIN, D.; ANNA, S. L.; GAROFF, S. **Stability of a compound sessile drop at the axisymmetric configuration**. In: J. Colloid Interface Sci. 462 (2016), pp. 88–99. doi: 10.1016/j.jcis.2015.09.043.

ZHOU, C.; PENGTAO; YUE, P.; FENG, J. J. **Formation of simple and compound drops in microfluidic devices**. In: Phys. Fluids 18.092105 (2006), pp. –. doi: 10.1063/1.2353116.

ZHOU, Y.; ZHAO, C.; BO, H. **Analyses and modified models for bubble shape and drag coefficient covering a wide range of working conditions**. In: Int. J. Multiphase Flow 127.103265 (2020), pp. –. doi: 10.1016/j.ijmultiphaseflow.2020.103265.

ZHU, S.; KHERBECHE, A.; FENG, Y.; THORVAL, M. **Impact of an air-in-liquid compound drop onto a liquid surface**. In: Phys. Fluids 32.041705 (2020). doi: 10.1063/5.0005702.